

國立交通大學
電子工程學系 電子研究所
碩士論文

奈米級金氧半場效電晶體應變矽物理之研究



**Strained Silicon Physics in
Nanoscale MOSFETs**

研究生：林以唐

指導教授：陳明哲 博士

中華民國九十七年七月

奈米級金氧半場效電晶體應變矽物理之研究

Strained Silicon Physics in Nanoscale MOSFETs

研究生：林以唐

Student：Yi-Tang Lin

指導教授：陳明哲博士

Advisor：Dr. Ming-Jer Chen



A Thesis

Submitted to Department of Electronics Engineering & Institute of Electronics

College of Electrical Engineering

National Chiao Tung University

in Partial Fulfillment of the Requirements

for the Degree of

Master of Science

In

Electronics Engineering

July 2008

Hsinchu, Taiwan, Republic of China

中華民國九十七年七月

奈米級金氧半場效電晶體應變矽物理之研究

研究生：林以唐

指導教授：陳明哲博士

國立交通大學 電子工程學系 電子研究所碩士班

摘要

爲了提升 MOSFETs 元件效能及載子遷移率(carrier mobility)，在(001) 晶圓上的單軸縱向(uniaxial longitudinal)及雙軸(biaxial)應變矽製程已被廣泛的應用在先進的奈米技術中。

在本論文中，首先，爲了探討在不同的晶圓方向及不同的應力條件下，是否能進一步的增高元件效能及降低元件功率，我們將應變張量(strain tensor)表示成縱向應力(longitudinal stress)、橫向應力(transverse stress)及垂直應力(normal stress)的函數。接著利用 deformation potential theory 以及 $k \cdot p$ framework 來分別計算在三種晶圓方向：(001)、(110)和(111)上及不同的應力條件下，應變矽材料的傳導帶和價電帶的能帶結構(band structure)、能谷位移(band edge shift)、三維 k 空間下的等能量面(constant energy surface)、二維能量等高線(2D energy contour)，以及有效質量(effective mass)。另外，額外的垂直晶圓方向應力及橫向應力也被考慮及計算。利用以上的計算結果來作爲分析的工具，我們發現在這些可能的應變形式中，對 nMOSFETs 來說，在(001)晶圓上的單軸及雙軸伸張應變具有較佳的增益；而對 pMOSFETs 來說，在(001)和(110)晶圓上的單軸壓縮應變具有較佳的增益。此外，對 pMOSFETs 來說，在(001) 晶圓上加上額外的橫向伸張應力可以進一步的增進元件的電導率(conductivity)。

接著，利用計算出來的能帶結構，我們萃取出在(001) 晶圓方向上的單軸及雙軸應變下的量子化有效質量(quantization effective mass)、二維及三維能態密度

有效質量(2D and 3D density-of-state effective mass)。此外，根據應變下的能帶結構，我們推導及修正了半導體元件物理中常用的物理表示式，包含材料的費米能階(Fermi energy)、傳導帶及價電帶的有效狀態密度(conduction and valence effective DOS)、本質載子濃度(intrinsic carrier concentration)，使其可以繼續延伸應用到材料內具有應變的情況。同時我們也計算了這些參數在單軸及雙軸應變下從零到 3GPa 的變化，並提出了合理的物理解釋。以上這些參數在決定材料特性及元件效能時相當重要。

最後，根據以上的討論，我們建立了一套物理模型及模擬器來評估及計算應力對 MOSFETs 元件造成的影響，包含平帶電壓(flat-band voltage)、應變下對應的多晶矽閘極/氧化層/通道截面能帶圖(band diagram)。並將三角形位能井近似法(triangular potential approximation) 延伸應用到應變矽 MOSFETs 元件中，同時也考慮閘極及通道均具有應變的情況。此方法可計算出在不同應力條件、外加電壓及元件參數下介面電場、次能階、反轉層載子濃度及多晶矽閘極/氧化層/通道跨壓等重要參數。接著，利用 WKB 方法，我們也計算出在(001)晶圓上單軸壓縮應變對 nMOSFETs 和 pMOSFETs 的閘極直接穿隧電流(gate direct tunneling current)的影響，模擬結果與實驗數據吻合。

Strained Silicon Physics in Nanoscale MOSFETs

Student: Yi-Tang Lin

Advisor: Dr. Ming-Jer Chen

Department of Electronics Engineering
& Institute of Electronics
National Chiao Tung University

Abstract

In this work, by using the deformation potential theory for conduction band and the $k \cdot p$ framework (6×6 Luttinger Hamiltonian) for valence band, the strain-altered band structure (E - k relation), the strain-induced band edge shift, the constant energy surface, and the 2D energy contour have been calculated for various stress conditions on three conventional wafer orientations, (100), (110), and (111). Moreover, the influences of the additional transverse or normal strain have been examined as well.

Next, utilizing the calculated E - k relation, the conventional physical parameters including the quantization effective mass, the 2D DOS Effective mass, and 3D DOS effective mass have been also extracted under uniaxial and biaxial stress on (001) wafer. Then, using the DOS effective masses and strain-induced band edge shifts, the Fermi energy of bulk silicon can be determined as a function of stress and doping concentration. These parameters are significant in calculating the subband energy and carrier density in the channel inversion layer of MOSFETs. In addition, we also evaluated the intrinsic carrier density of bulk silicon under uniaxial and biaxial stress from zero to 3GPa.

Furthermore, we extended and modified the previously developed triangular potential approximation, a self-consistent method that takes the quantum confinement effect in the inversion layer and the conservation of electric flux at the SiO₂/Si interface into consideration, for the unstrained MOSFETs to construct the band diagram and physical model for strained counterparts. The method has also been applied to both nMOSFETs and pMOSFETs with corresponding revisions of the physical model. In our model, the stresses for poly gate and channel are allowed to have different magnitude and type.

Finally, applying our model and the extracted physical parameters, we can calculate the interface electric field, subband energy, inversion carrier density, substrate band bending, etc., with various stress conditions, applied voltage and device parameters as inputs. Then, utilizing the WKB approximation, the transmission probability and gate direct tunneling current for various stress conditions can also be evaluated. The simulated results agree with the experimental data of the former works.

Acknowledgement

這篇論文的完成，首先要感謝陳明哲教授二年來的指導與鼓勵。在雜訊與擾動課程及每週 seminar 和老師的互動中，讓我學習到許多做研究的方法、思考的方式、以及嚴謹的態度。而在半導體元件物理課程時及擔任助教時與學弟妹的互動中，也使我獲益良多，對固態領域有了更深入的體悟。另外要感謝謝振宇學長及梁惕華同學平日極具啟發性的討論，蒐集的 paper 及資料的分享，並一起釐清了許多觀念，協助我確立研究的方法與方向。同時要感謝李建志學長、許智育學長、李韋漢學長在課業、生活及研究上的幫助與建議。另外也要感謝張書通教授所撰寫的程式及簡鶴年同學無私的分享與討論，使我能夠儘快的瞭解這個領域的關鍵知識與技術。也要感謝呂立方同學在研究用軟體及物理模擬軟體的使用以及研究經驗的分享；周佳宏、宋東壕、陳彥銘同學平日的討論與幫助；以及湯侑穎同學在系學會網路組時期、擔任半導體元件物理助教時、以及實驗室事務上的大力協助。另外也要感謝張智勝經理、李文欽經理和張書通教授在口試及面試時的指導與建議。最後要感謝我的家人的全力支持，讓我能夠無後顧之憂的專心在研究之上。

Yi-Tang, Lin

August 2008

Contents

Chinese Abstract	i
English Abstract	iii
Acknowledgement	v
Contents	vi
Table Captions.....	ix
Figure Captions	x
Chapter 1 Introduction.....	1
Chapter 2 Strain-altered Band Structures.....	3
2.1 Introduction.....	3
2.2 A Review of Mechanics of Materials.....	3
2.2.1 Stress	3
2.2.2 Strain	5
2.2.3 Relationship between Stress and Strain	6
2.3 Hamiltonian.....	8
2.3.1 Hamiltonian for Conduction Band (Deformation Potential Theory) ...	8
2.3.2 Hamiltonian for Valence Band ($k \cdot p$ Framework).....	9
2.3.2.1 Various Materials (Si/Ge/GaAs)	11
2.4 Types of Stress and Various Wafer Orientations	12
2.5 Results and Discussion	13
2.5.1 Band Structures	13
2.5.2 Strain-induced Subband Energy Shift.....	14

2.5.3 Constant Energy Surface.....	17
2.5.4 Two-dimension Energy Contour in the Plane of Wafer Surface	17
2.5.5 Advantageous Strains and Wafer Orientations.....	18
2.5.6 Influences of Additional Transverse or Normal Stress	21
2.6 Conclusion	23
Chapter 3 The Properties of Bulk Silicon in the Presence of Stress	25
3.1 Introduction.....	25
3.2 Effective Mass	26
3.3 Carrier Density and Effective DOS	29
3.3.1 Electrons in Conduction Band	29
3.3.2 Holes in Valence Band	30
3.3.3 Simulated Results of N_C^* and N_V^*	31
3.4 Fermi Energy of Bulk Silicon	31
3.5 Intrinsic Carrier Concentration	33
3.6 Conclusion	33
Chapter 4 Strain-induced Change of Gate Direct Tunneling Current.....	35
4.1 Introduction.....	35
4.2 Physical Model.....	36
4.2.1 Hole Subband Energy and Carrier Density (pMOSFETs)	36
4.2.2 Hole Direct Tunneling Current for pMOSFETs.....	39
4.2.3 Electron Direct Tunneling Current for nMOSFETs.....	41
4.3 Results and Discussion	42
4.3.1 Hole Direct Tunneling Current for pMOSFETs.....	42

4.3.1.1 Parameters Extraction for the Vertical Electric Field Component.....	42
4.3.1.2. Calculation for the Stress Component (Valence Band Edge Shifts).....	43
4.3.1.3. Hole Direct Tunneling Current	44
4.3.1.4 Uniaxial Transverse Stress	45
4.3.2 Electron Direct Tunneling Current for nMOSFETs.....	46
4.4 Conclusion	47
Chapter 5 Conclusions.....	48
References.....	51
Vita	115



Table Captions

Chapter 2

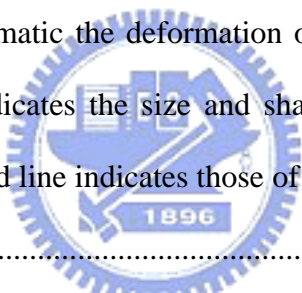
Table 2.1 The deformation potentials, Luttinger parameters, elastic stiffness constants, and split-off energy for Si, Ge, and GaAs.	55
Table 2.2 The normal, longitudinal, and transverse direction for (001), (110), and (111) wafer.	56
Table 2.3 The stress tensor and strain tensor for biaxial stress on (001) wafer, uniaxial stress along $[110]$, $[\bar{1}10]$, $[001]$, $[111]$, and $[11\bar{2}]$ direction.	57
Table 2.4 The resultant strain tensors in response to the combination of normal, longitudinal, and transverse stress for the three wafer orientations.	58
Table 2.5 Numerical values of effective mass for silicon conduction band in inversion layer given by [30].	59
Table 2.6 The conductivity, transverse, and quantization effective masses of the top band for bulk silicon with various stress conditions and wafer orientations. The quantization effective masses of the second band are also listed.	60
Table 2.7 Comparison the effective masses between the 1GPa uniaxial longitudinal compressive stress with and without additional 1GPa uniaxial transverse tensile stress for (001) and (110) wafer.	61

Chapter 4

Table 4.1 Equations for subband calculation.	62
---	----

Figure Captions

Chapter 2

- Fig. 2.1.. (a) An arbitrary force $\Delta R(P)$ acting on an infinitesimal area ΔA at point P. The normal component of the force is $\Delta F(P)$ and the tangential components of the force are $\Delta V_s(P)$ and $\Delta V_t(P)$ along two orthogonal directions in the plane. (b) Schematic of the nine components defining the stress state at an arbitrary point in three dimensions.....63
- Fig. 2.2. (a) Schematic of the deformation of a body applied to normal stress along y-axis; and (b) schematic the deformation of a body applied to pure shear stress. Dash line indicates the size and shape of the original body before deformation and solid line indicates those of the body after deformation.
.....64
- Fig. 2.3. Schematic of the surface orientation and the corresponding stress directions for (001) wafer. The shadow region indicates the wafer surface. The surface normal is [001], the longitudinal (channel) direction is [110], and the transverse direction, which is perpendicular to the channel in the plane, is $[\bar{1}10]$65
- Fig. 2.4. Schematic of the surface orientation and the corresponding stress directions for (110) wafer. The shadow region indicates the wafer surface. The surface normal is [110], the longitudinal (channel) direction is $[\bar{1}10]$, and the transverse direction, which is perpendicular to the channel in the plane, is $[00\bar{1}]$66
- Fig. 2.5. Schematic of the surface orientation and the corresponding stress directions

for (111) wafer. The shadow region indicates the wafer surface. The surface normal is [111], the longitudinal (channel) direction is $[\bar{1}10]$, and the transverse direction, which is perpendicular to the channel in the plane, is $[11\bar{2}]$67

Fig. 2.6. Silicon valence band structures for (a) unstressed, (b) 1GPa uniaxial longitudinal compressive, (c) 1GPa uniaxial longitudinal tensile, (d) 1GPa uniaxial transverse compressive, and (e) 1GPa uniaxial transverse tensile stress on (001) wafer.68

Fig. 2.7. Silicon valence band structures for (a) 1GPa biaxial compressive and (b) 1GPa biaxial tensile stress on (001) wafer.69

Fig. 2.8. Silicon valence band structures for (a) unstressed, (b) 1GPa uniaxial longitudinal compressive, (c) 1GPa uniaxial longitudinal tensile, (d) 1GPa uniaxial transverse compressive, and (e) 1GPa uniaxial transverse tensile stress on (110) wafer.70

Fig. 2.9. Silicon valence band structures for (a) unstressed, (b) 1GPa uniaxial longitudinal compressive, (c) 1GPa uniaxial longitudinal tensile, (d) 1GPa uniaxial transverse compressive, and (e) 1GPa uniaxial transverse tensile stress on (111) wafer.71

Fig. 2.10. Strain-induced hole subband energy shift versus (a) uniaxial longitudinal and (b) uniaxial transverse stress on (001) wafer.72

Fig. 2.11. Strain-induced hole subband energy shift versus biaxial stress on (001) wafer.73

Fig. 2.12. Comparison between the strain-induced hole subband energy shift calculated by 4×4 and 6×6 Hamiltonian for (a) uniaxial longitudinal and (b) biaxial stress on (001) wafer. The solid line indicates the subband energy calculated by the 6×6 Hamiltonian. The dotted line indicates the subband

energy calculated by 4 by 4 Hamiltonian.....	74
Fig. 2.13. Strain-induced hole subband energy shift versus (a) uniaxial longitudinal and (b) uniaxial transverse stress on (110) wafer.	75
Fig. 2.14. Strain-induced subband energy shift versus (a) uniaxial longitudinal and (b) uniaxial transverse stress on (111) wafer.....	76
Fig. 2.15. Hole constant energy surface of unstressed bulk silicon for three lowest bands.....	77
Fig. 2.16. Hole constant energy surface of silicon under 1GPa uniaxial longitudinal (a) compressive and (b) tensile stress on (001) wafer for three lowest bands.	78
Fig. 2.17. Hole constant energy surface of silicon under 1GPa uniaxial transverse (a) compressive and (b) tensile stress on (001) wafer for three lowest bands.	79
Fig. 2.18. Hole constant energy surface of Silicon under 1GPa biaxial (a) compressive and (b) tensile stress on (001) wafer for three lowest bands.	80
Fig. 2.19. Hole constant energy surface of silicon under 1GPa uniaxial longitudinal (a) compressive and (b) tensile stress on (110) wafer for three lowest bands.	81
Fig. 2.20. Hole constant energy surface of silicon under 1GPa uniaxial transverse (a) compressive and (b) tensile stress on (110) wafer for three lowest bands.	82
Fig. 2.21. Hole constant energy surface of silicon under 1GPa uniaxial longitudinal (a) compressive and (b) tensile stress on (111) wafer for three lowest bands.	83
Fig. 2.22. Hole constant energy surface of silicon under 1GPa uniaxial longitudinal (a) compressive and (b) tensile stress on (111) wafer for three lowest bands.	

.....	84
Fig. 2.23. Contour map in k_x, k_y plane ($k_z=0$) of unstressed bulk silicon on (001) wafer for three lowest valence bands.	85
Fig. 2.24. Contour map in k_x, k_y plane ($k_z=0$) of silicon under 1GPa uniaxial longitudinal (a) compressive and (b) tensile stress on (001) wafer for three lowest valence bands.	86
Fig. 2.25. Contour map in k_x, k_y plane ($k_z=0$) of silicon under 1GPa uniaxial transverse (a) compressive and (b) tensile stress on (001) wafer for three lowest valence bands.	87
Fig. 2.26. Contour map in k_x, k_y plane ($k_z=0$) of silicon under 1GPa biaxial (a) compressive (b) tensile stress on (001) wafer for three lowest valence bands.	88
Fig. 2.27. Contour map in k_x, k_y plane ($k_z=0$) of silicon under 1GPa uniaxial longitudinal (a) compressive and (b) tensile stress on (110) wafer for three lowest valence bands.	89
Fig. 2.28. Contour map in k_x, k_y plane ($k_z=0$) of silicon under 1GPa uniaxial transverse (a) compressive and (b) tensile stress on (110) wafer for three lowest valence bands.	90
Fig. 2.29. Contour map in k_x, k_y plane ($k_z=0$) of silicon under 1GPa uniaxial longitudinal (a) compressive and (b) tensile stress on (111) wafer for three lowest valence bands.	91
Fig. 2.30. Contour map in k_x, k_y plane ($k_z=0$) of silicon under 1GPa uniaxial transverse (a) compressive and (b) tensile stress on (111) wafer for three lowest valence bands.	92
Fig. 2.31. Band structures, constant energy surface, and energy contour of bulk silicon under 1GPa longitudinal compressive stress with additional 1GPa transverse	

tensile stress on (a) (001) and (b) (110) wafer, respectively.....93

Chapter 3

Fig. 3.1. Effective masses along the three axes of the ellipsoid, $m_{[110]}$, $m_{[\bar{1}10]}$, and $m_{[001]}$, versus uniaxial longitudinal stress for three lowest valence bands.
94

Fig. 3.2. 3D (bulk) and 2D DOS effective masses versus uniaxial longitudinal stress for three lowest valence bands.95

Fig. 3.3. Effective masses along the three axes of the ellipsoid, $m_{[100]}$, $m_{[010]}$, and $m_{[001]}$, versus biaxial stress for three lowest valence bands.96

Fig. 3.4. 3D (bulk) and 2D DOS effective masses versus biaxial stress for three lowest valence bands.....97

Fig. 3.5. Schematic of the strain-induced energy valleys splitting for (a) conduction band electrons and (b) valence band holes.....98

Fig. 3.6. Conduction and valence effective DOS, N_c and N_v , versus uniaxial stress....
99

Fig. 3.7. Conduction and valence effective DOS, N_c and N_v , versus biaxial stress.....
 100

Fig. 3.8. Fermi energy of bulk silicon versus uniaxial stress for various doping concentrations. The figure also shows the intrinsic Fermi level, conduction band edge, and valence band edge versus stress. 101

Fig. 3.9. Fermi energy of bulk silicon versus biaxial stress for various doping concentration. The figure also shows the intrinsic Fermi level, conduction

band edge, and valence band edge versus stress.	102
Fig. 3.10. Intrinsic carrier concentration versus uniaxial and biaxial stress.	103

Chapter 4

Fig. 4.1. Valence band hole dispersion relation along [100] and [110] direction for the three lowest bands calculated by six-band $k \cdot p$ method under channel inversion condition ($F_{Si}=1MV/cm$). The external stress is (a) unstressed and (b) 500MPa uniaxial compressive stress along [110] direction.	104
Fig. 4.2. Schematic of band diagram of a p^+ polysilicon/SiO ₂ /n-Si structure biased in channel inversion condition and stressed with uniaxial longitudinal compressive stress. The solid lines indicate the conduction and valence band edge without external stress. The dotted lines indicate the stress induced band edge shift of the conduction and valence band. The figure also shows the energy quantization effect in the channel inversion layer and hole direct tunneling current from the channel inversion layer to the polysilicon gate under stress.	105
Fig. 4.3. Schematic of the band diagram of a p^+ polysilicon/SiO ₂ /n-Si (pMOS) structure, which is biased a negative gate voltage. The poly gate and channel are under arbitrary strain. The expression of flat band voltage for pMOSFETs under arbitrary strain can be derived with the help of this diagram.	106
Fig. 4.4. Schematic of band diagram of an n^+ polysilicon/SiO ₂ /p-Si structure biased in channel inversion condition and stressed with uniaxial longitudinal compressive stress. The solid lines indicate the conduction and valence band edge without external stress. The dotted lines indicate the stress induced	

band edge shift of the conduction and valence band. The figure also shows the energy quantization effect in the channel inversion layer and electron direct tunneling current from the channel inversion layer to the polysilicon gate under stress. 107

Fig. 4.5. Schematic of the band diagram of an n^+ polysilicon/SiO₂/p-Si (nMOS) structure, which is biased a positive gate voltage. The poly gate and channel are under arbitrary strain. The expression of flat band voltage for nMOSFETs under arbitrary strain can be derived with the help of this diagram..... 108

Fig. 4.6. Hole subband energy at gamma point versus F_{Si} without external stress. The circles are data calculated by the six-band $k \cdot p$ method with Schrödinger-Poisson equation. The solid lines are the fitting by the triangular potential approximation and the improved one band EMA. The figure also shows the quantization effective mass of the three lowest bands for best fitting. 109

Fig. 4.7. Hole subband energy at gamma point versus stress with various F_{Si} . (a) First band, (b) second band, and (c) third band. The circles are data calculated by $k \cdot p$ method with Schrödinger-Poisson equation. The solid lines are the data calculated by Equation (4.1) for the three lowest bands, respectively.... 110

Fig. 4.8. The strain-induced band edge shift versus stress for bulk silicon (a) conduction and (b) valence band..... 111

Fig. 4.9. (a) $\Delta J_{HDT}/J_{HDT}$ versus Stress. The squares, diamonds, and circles are data published by former works. The solid lines are the simulation result by our model. (b) Hole subband energy versus stress. (c) Carriers density versus stress. (d) Hole direct tunneling current density versus stress. 112

Fig. 4.10.(a) $\Delta J_{EDT}/J_{EDT}$ versus Stress. The squares, diamonds, and circles are data published by former works. The solid lines are the simulation result by our model. (b) Electron subband energy versus stress. (c) Carriers density versus stress. (d) Electron direct tunneling current density versus stress..... 113

Fig. 4.11. Compare the influences of electron direct tunneling current between the two different doping concentrations of substrate. 114



Chapter 1

Introduction

In advanced nanotechnology, strain process has been extensively used for enhancing device performance [1], [2]. Therefore, having fundamental understanding of strain physics and studying the influences of strain in the nano-scale Si devices are essential. Moreover, developing a physically reasonable model and incorporating it into a quantum simulator in order to provide clear insight for future strain engineering and assess the influences of strain, such as subband energy splitting, repopulation of carrier density in each subband, and change of gate direct tunneling current, is crucial as well.

In order to give insights into the future strained devices while meeting the high performance and low power requirements, we first examine several potential stress types on various wafer orientations in Chapter 2. The simulation results including the strain-altered band structure, strain-induced band edge shift, constant energy surface in momentum space, two-dimensional energy contour, and the effective masses along the different crystallization directions, which are calculated by the deformation potential theory for conduction band and $k \cdot p$ framework for valence band, are utilized to be the tools for estimating device performance. In addition, the influences of additional transverse stress, which is existent in process such as capping layer or STI stressor when the dimension of channel width is comparable with channel length, but usually ignored in former work, are addressed as well.

Second, in order to understand the properties of bulk silicon such as the Fermi level and intrinsic carrier concentration in the presence of strain, we utilize the

strain-altered band structures and the effective mass approximation to calculate the quantization effective mass, 2D DOS effective mass, and 3D DOS effective mass of bulk silicon under uniaxial and biaxial stress on (001) wafer in Chapter 3. Consequently, the effective DOS, Fermi energy, and intrinsic carrier concentration are also extracted with stress varying from zero to 3GPa. However, it is noticeable that the effective mass approximation, or the hypothetical elliptic constant energy surface, is suitable for large strain due to the strain symmetry, but introduces large error under small strain.

Third, in IC industry, the phenomenon of gate direct tunneling current in MOSFETs induces many problems such as standby power consumption, leakage current in C-V measurement, and etc. [3]-[5]. In the recent years, the dimension of device keeps scaling down while gate oxide thickness keeps thinning. Even the thickness is only several atomic layers. Therefore, the drawback of gate direct tunneling current becomes severe and influences the normal operation of devices [3]. On the other hand, in the advanced nanotechnology, the strain process is extensively used. Selecting the type of strain appropriately may enhance the mobility and alleviate the gate leakage in the meantime [1], [2], [6]. Thus, a computing efficient and reasonably physical model for characterizing and modeling the gate direct tunneling current of strained silicon device is essential. In chapter 4, we have developed a triangular potential approximation based quantum simulator for strained MOSFETs modeling.

Chapter 2

Strain-altered Band Structures

2.1 Introduction

In this chapter, we first review the topic of mechanics of materials and the equilibrium analysis of deformable bodies. Next, the well recognized methods, namely the deformation potential theory for conduction band and $k \cdot p$ framework for valence band, are introduced to calculate the strain-altered band structure (energy dispersion relation). Then, in order to give insights into the future strained devices while meeting the high performance and low power requirements, several potential wafer orientations, (001), (110), and (111), with various stress conditions including uniaxial longitudinal, uniaxial transverse, and biaxial stress, will be examined. The calculated results in terms of the band structures, effective masses, strain-induced subband energy shift, constant energy surface, and two-dimensional energy contour, will exhibit the ability to quantitatively determine the device performance. Finally, the influences of the additional transverse strain on the devices will also be discussed.

2.2 A Review of Mechanics of Materials

In this section, we first review the concept of stress and strain, and then make a connection between the two. Note that the stress and strain produced by the change of temperature [7] are not included, that is, the temperature remains constant in this work.

2.2.1 Stress

Stress is the distribution of a force over the area on which the force acts. The

intensity of stress is expressed as force per unit area [7], [8]. There are two types of stress: normal stress and shear stress. To illustrate this, let us consider an arbitrary force vector $\Delta R(P)$ at certain point P acting on an infinitesimal area ΔA with normal vector n as shown in Fig. 2.1(a). The force is resolved into normal and tangential components $\Delta F(P)$ and $\Delta V(P)$. The tangential component is further resolved into components along two orthogonal directions, s and t in the plane. Then, the normal stress σ_n and the shear stress τ_{ns} and τ_{nt} at point P are defined by the following expressions [7]:

$$\sigma_n(P) = \lim_{\Delta A \rightarrow 0} \left(\frac{\Delta F(P)}{\Delta A} \right) \quad (2.1a)$$

$$\tau_{ns}(P) = \lim_{\Delta A \rightarrow 0} \left(\frac{\Delta V_s(P)}{\Delta A} \right) \quad (2.1b)$$

$$\tau_{nt}(P) = \lim_{\Delta A \rightarrow 0} \left(\frac{\Delta V_t(P)}{\Delta A} \right). \quad (2.1c)$$

Next, we expand above definitions of stress on a particular plane to all three mutually orthogonal planes that intercept a given common point in a deformable body as shown in Fig. 1(b). In the figure, σ_{ii} refers to the normal stress components acting on the planes perpendicular to i -direction, while τ_{ij} indicates the shear stress components oriented in the j -direction acting on the planes perpendicular to i -direction. According to Cauchy's equation of motion, these nine components are sufficient to define the stress state at any point in a deformable body [8]. Furthermore, at moment equilibrium, the shear stress components must satisfy $\tau_{ij} = \tau_{ji}$ [7]. Thus, a stress tensor with six independent components is sufficient to describe the state of stress:

$$\sigma = \begin{bmatrix} \sigma_{xx} \\ \sigma_{yy} \\ \sigma_{zz} \\ \tau_{yz} \\ \tau_{zx} \\ \tau_{xy} \end{bmatrix}. \quad (2.2)$$

2.2.2 Strain

When a deformable body is subjected to external forces, it changes size and/or shape in response to the applied forces. The deformation of the body may include both changes of length (normal strain) and changes of angles (shear strain). For example, let us first focus on the case of a normal stress applied to the deformable body along the y-axis as shown in Fig. 2.2(a). A positive value for the stress σ_y , that is, a tensile stress, causes the body to elongate along y-axis and to contract along x and z-axis. On the other hand, a negative value for the stress σ_y indicates compressive stress, hence causing the body to be shortened along y-axis and dilated along x and z-axis. The normal strain is defined as

$$\varepsilon = \frac{\Delta L}{L} = \frac{L' - L}{L} \quad (2.3)$$

where L , L' , and ΔL denote the original length, the length after deformation has occurred, and the total elongation of the body along y-axis, respectively. A positive value for strain ε indicates the body is stretched along y-axis, that is, $L' > L$, and is called tensile strain. A negative value for ε indicates that the body is contracted along y-axis, that is, $L' < L$, and is referred to as the compressive strain.

Next, let us consider that a body deforms due to the pure shear stress as shown in Fig. 2.2(b). After deformation, the original right angle $\pi/2$ becomes an acute angle θ' . The shear strain is defined as the change in angle between two originally perpendicular line segments as shown in Fig. 2.2(b). Thus, we have [7], [9], and [10]

$$\gamma_{yz} = \gamma_{zy} = \frac{\pi}{2} - \theta' = \frac{\partial u_y}{\partial z} + \frac{\partial u_z}{\partial y}. \quad (2.4)$$

Likewise, we extend these definitions of normal strain and shear strain to the three mutually orthogonal planes [8]-[10]

$$\varepsilon_{xx} = \frac{\partial u_x}{\partial x}, \quad \varepsilon_{yy} = \frac{\partial u_y}{\partial y}, \quad \varepsilon_{zz} = \frac{\partial u_z}{\partial z} \quad (2.5a)$$

$$\gamma_{xy} = \gamma_{yx} = \frac{\partial u_x}{\partial y} + \frac{\partial u_y}{\partial x} \quad (2.5b)$$

$$\gamma_{yz} = \gamma_{zy} = \frac{\partial u_y}{\partial z} + \frac{\partial u_z}{\partial y} \quad (2.5c)$$

$$\gamma_{zx} = \gamma_{xz} = \frac{\partial u_x}{\partial z} + \frac{\partial u_z}{\partial x} \quad (2.5d)$$

where u_x , u_y , and u_z are the displacements in the x, y, and z direction, respectively. It is worth noting that γ_{ij} denotes engineered shear strain and ε_{ij} is called average shear strain and defined as one half the γ_{ij} [9], [10].

Similar to stress tensor, the strain tensor is also composed of six independent components

$$\varepsilon = \begin{bmatrix} \varepsilon_{xx} \\ \varepsilon_{yy} \\ \varepsilon_{zz} \\ \varepsilon_{yz} \\ \varepsilon_{zx} \\ \varepsilon_{xy} \end{bmatrix}. \quad (2.6)$$

2.2.3 Relationship between Stress and Strain

When a small normal stress, which remains well below the yield point, is applied to a homogeneous and isotropic body, the linear relationship between normal stress and normal strain can be described by Hooke's law [7],

$$\sigma = E\varepsilon \quad (2.7)$$

where the constant of proportionality E represents the Young's modulus. Moreover,

associated with the normal strain of an elastic body in the direction of the applied normal stress, there is usually a transverse strain in two other directions, as illustrated in Fig. 2.2(a). The relationship between normal strain and transverse strain is described by [7], [9]

$$\varepsilon_{tran} = -\nu\varepsilon_{long} \quad (2.8)$$

where the constant of proportionality ν represents the Poisson's ratio. Finally, to relate shear stress and shear strain, the Hooke's law for shear is used [7], [9]

$$\tau = G\gamma \quad (2.9)$$

where the constant of proportionality G represents the shear modulus of elasticity.

By the principle of linear superposition, we can use the equations (2.7), (2.8), and (2.9) to combine strain response by adding together the separate responses produced by the six components of stress tensor. Consequently, the generalized Hooke's law for isotropic materials is expressed as [7]

$$\varepsilon_{xx} = \frac{1}{E} [\sigma_{xx} - \nu(\sigma_{yy} + \sigma_{zz})] \quad (2.10a)$$

$$\varepsilon_{yy} = \frac{1}{E} [\sigma_{yy} - \nu(\sigma_{xx} + \sigma_{zz})] \quad (2.10b)$$

$$\varepsilon_{zz} = \frac{1}{E} [\sigma_{zz} - \nu(\sigma_{xx} + \sigma_{yy})] \quad (2.10c)$$

$$\gamma_{xy} = \frac{1}{G} \tau_{xy}, \quad \gamma_{xz} = \frac{1}{G} \tau_{xz}, \quad \gamma_{yz} = \frac{1}{G} \tau_{yz} \quad (2.10d)$$

It is noteworthy that for isotropic materials, shear strains are independent of normal stresses, and, likewise, normal strains are independent of shear stresses. In addition, the three components of shear are uncoupled [7].

For convenience, we usually combine the equations (2.2), (2.6), and (2.10) to establish the elastic strain-stress matrix for relating stress tensor and strain tensor [8], [10]-[12].

$$\begin{bmatrix} \varepsilon_{xx} \\ \varepsilon_{yy} \\ \varepsilon_{zz} \\ 2\varepsilon_{yz} \\ 2\varepsilon_{zx} \\ 2\varepsilon_{xy} \end{bmatrix} = \begin{bmatrix} S_{11} & S_{12} & S_{12} & 0 & 0 & 0 \\ S_{12} & S_{11} & S_{12} & 0 & 0 & 0 \\ S_{12} & S_{12} & S_{11} & 0 & 0 & 0 \\ 0 & 0 & 0 & S_{44} & 0 & 0 \\ 0 & 0 & 0 & 0 & S_{44} & 0 \\ 0 & 0 & 0 & 0 & 0 & S_{44} \end{bmatrix} \begin{bmatrix} \sigma_{xx} \\ \sigma_{yy} \\ \sigma_{zz} \\ \tau_{yz} \\ \tau_{zx} \\ \tau_{xy} \end{bmatrix} \quad (2.11)$$

where S_{11} , S_{12} , and S_{44} are the elastic stiffness constants.

These relationships can be determined experimentally by performing certain stress-strain and torsion tests [7]. Some extracted values of bulk Silicon for Young's modulus (130GPa for <100> directions and 169GPa for <110> directions), Poisson's ratio (0.22-0.28), and shear modulus (79.9GPa) can be found in [8], [13]-[16]. Then, using these values, the elastic stiffness constants, S_{11} , S_{12} , and S_{44} can be evaluated. The values used in this work are listed in Table 2.1. Note that although silicon is an anisotropic crystal, for the purposes of simplification it is conventional to use the equation (2.11) for mechanical analysis of bulk silicon [8], [11], and [12].

2.3 Hamiltonian

The deformation potential theory [17] (for conduction band) and $k \cdot p$ Framework [18], [19] (for valence band) are the primary [18] method to calculate the strain-altered band structures including band shift and warping to date.

2.3.1 Hamiltonian for Conduction Band (Deformation Potential Theory)

In deformation potential theory, the total Hamiltonian for each energy valleys of silicon conduction band is [18]

$$H = \left(\frac{\hbar^2 (k_l - k_0)^2}{2m_l^*} + \frac{\hbar^2 k_t^2}{2m_t^*} \right) + (E_c + \Xi_d Tr(\varepsilon_{ij}) + \Xi_u \varepsilon_l) \quad (2.12)$$

where \hbar is the reduced Planck's constant. k_l and k_t are the wavevectors parallel and

perpendicular to the $\langle 100 \rangle$ directions of each energy valleys, respectively. m_l^* and m_t^* are the longitudinal and transverse effective mass, respectively. E_c is the conduction band edge of unstrained bulk silicon. Ξ_d and Ξ_u are the dilation and uniaxial deformation potential for silicon conduction band, respectively. $Tr(\varepsilon_{ij})$ stands for the trace of the strain tensor. ε_l is the longitudinal strain component. Note that m_l^* and m_t^* are generally assumed to be constant since they do not change significantly under small or moderate strain [12], [18]. In other words, the strains do not alter the energy dispersion in conduction band, the first part of Equation (2.12), but just shift the band edge, the second part. Applying Equation (2.12), the quantities of band edge shift for the six conduction band minima along the $\langle 100 \rangle$ directions can be expressed as [12]

$$\Delta E_C = \Xi_d (\varepsilon_{xx} + \varepsilon_{yy} + \varepsilon_{zz}) + \Xi_u \varepsilon_{xx} \text{ for the valleys along } [100] \text{ and } [\bar{1}00] \quad (2.13a)$$

$$\Delta E_C = \Xi_d (\varepsilon_{xx} + \varepsilon_{yy} + \varepsilon_{zz}) + \Xi_u \varepsilon_{yy} \text{ for the valleys along } [010] \text{ and } [0\bar{1}0] \quad (2.13b)$$

$$\Delta E_C = \Xi_d (\varepsilon_{xx} + \varepsilon_{yy} + \varepsilon_{zz}) + \Xi_u \varepsilon_{zz} \text{ for the valleys along } [001] \text{ and } [00\bar{1}] \quad (2.13c)$$

Note that the shear strain terms do not contribute to the band shift, and the strain-induced band edge shift is only proportional to the normal strain terms.

2.3.2 Hamiltonian for Valence Band ($\mathbf{k} \cdot \mathbf{p}$ Framework)

The influences of strain on valence band structures include not only band shifts, but also strong band warping. Thus, the deformation potential theory, which considers only the band shift, cannot serve for valence band. In order to calculate the strain-altered valence band structures of bulk silicon, we employ the six-band $\mathbf{k} \cdot \mathbf{p}$ method [20]. The $\mathbf{k} \cdot \mathbf{p}$ method is based on perturbation theory and symmetry

consideration [18]. The strain effects can be easily introduced to $k \cdot p$ framework [18], [21]. According to Pikus and Bir [18], the strain Hamiltonian is formally identical to the $k \cdot p$ Hamiltonian (Luttinger Hamiltonian) [18]. The correspondence between the strain and $k \cdot p$ Hamiltonian is $k_i k_j \leftrightarrow \varepsilon_{ij}$ and the total Hamiltonian is given by

$H = H_{k \cdot p} + H_{strain}$ [18]. The total Hamiltonian is expressed by [18], [21]

$$H = H_{k \cdot p} + H_{strain} = \begin{bmatrix} -P-Q & L & -M & 0 & \frac{1}{\sqrt{2}}L & -\sqrt{2}M \\ L^+ & -P+Q & 0 & -M & \sqrt{2}Q & -\sqrt{\frac{3}{2}}L \\ -M^+ & 0 & -P+Q & -L & -\sqrt{\frac{3}{2}}L^+ & -\sqrt{2}Q \\ 0 & -M^+ & -L^+ & -P-Q & \sqrt{2}M^+ & \frac{1}{\sqrt{2}}L^+ \\ \frac{1}{\sqrt{2}}L^+ & \sqrt{2}Q^+ & \sqrt{\frac{3}{2}}L & \sqrt{2}M & -P-\Delta & 0 \\ -\sqrt{2}M^+ & -\sqrt{\frac{3}{2}}L^+ & -\sqrt{2}Q^+ & \frac{1}{\sqrt{2}}L & 0 & -P-\Delta \end{bmatrix} \quad (2.14)$$

where $P = P_k + P_\varepsilon$, $Q = Q_k + Q_\varepsilon$, $L = L_k + L_\varepsilon$, and $M = M_k + M_\varepsilon$. The symbol Δ is the split-off energy. The $k \cdot p$ terms in the Hamiltonian are defined as

$$P_k = \frac{\hbar^2}{2m_0} \gamma_1 (k_x^2 + k_y^2 + k_z^2) \quad (2.15a)$$

$$Q_k = \frac{\hbar^2}{2m_0} \gamma_2 (k_x^2 + k_y^2 - 2k_z^2) \quad (2.15b)$$

$$L_k = \frac{\hbar^2}{m_0} \sqrt{3} \gamma_3 (k_x - ik_y) k_z \quad (2.15c)$$

$$M_k = -\frac{\hbar^2}{2m_0} \sqrt{3} [\gamma_2 (k_x^2 - k_y^2) - 2i\gamma_3 k_x k_y] \quad (2.15d)$$

where γ_1 , γ_2 , and γ_3 are the Luttinger parameters. m_0 is the mass of free electron. k_x , k_y , and k_z are the wavevectors along x, y, and z-axis, respectively. The strain terms in the Hamiltonian are defined as

$$P_\varepsilon = -a_v(\varepsilon_{xx} + \varepsilon_{yy} + \varepsilon_{zz}) \quad (2.16a)$$

$$Q_\varepsilon = -\frac{b}{2}(\varepsilon_{xx} + \varepsilon_{yy} - 2\varepsilon_{zz}) \quad (2.16b)$$

$$L_\varepsilon = -d(\varepsilon_{xz} - i\varepsilon_{yz}) \quad (2.16c)$$

$$M_\varepsilon = \frac{\sqrt{3}}{2}b(\varepsilon_{xx} - \varepsilon_{yy}) - id\varepsilon_{xy} \quad (2.16d)$$

where a , b , and d are the deformation potentials for valence band. The components of strain tensor are defined in Equation (2.5) and (2.6). The values of the Luttinger parameters and deformation potentials for silicon are given in Table 1. Note that the valence band edge for unstrained silicon is at zero value in this expression.

For the sake of brevity, many works ignored the coupling effect of the split-off band. In this case, the Hamiltonian of the top and second band can be described by a 4×4 Hamiltonian [the upper-left 4×4 matrix block in Equation (2.14)].

$$H = \begin{bmatrix} -P-Q & L & -M & 0 \\ L^+ & -P+Q & 0 & -M \\ -M^+ & 0 & -P+Q & -L \\ 0 & -M^+ & -L^+ & -P-Q \end{bmatrix} \quad (2.17)$$

Then, the analytic solution of the valence band structure for top two bands can be obtained as

$$E(k) = -P_k - P_\varepsilon \pm \sqrt{|Q_k + Q_\varepsilon|^2 + |L_k + L_\varepsilon|^2 + |M_k + M_\varepsilon|^2} \quad (2.18)$$

In section 2.4.2, we will discuss the differences in the strain-induced subband energy shift calculated by the 6×6 and 4×4 Hamiltonian.

2.3.2.1 Various Materials (Si, Ge, and GaAs)

The valence bands for all diamond and zinc blende structure semiconductors whose band gap is much larger than the split-off energy can be calculated using the Luttinger Hamiltonian. Thus, using the corresponding parameters, the deformation potentials, Luttinger parameters, elastic stiffness constants, and split-off energy, as listed in Table 2.1, the band structures for the other two typical semiconductors, Ge and GaAs, can be evaluated as well.

2.4 Types of Stress and Various Wafer Orientations

In this section, we first define the directions of normal, longitudinal, and transverse stress for three conventional wafer orientations, (001), (110), and (111). Then, the stress tensors and strain tensors for these wafer orientations are expressed as a function of the corresponding normal, longitudinal, and transverse stress.

Fig. 2.3, 2.4, and 2.5 show the surface orientations and the corresponding stress directions for (001), (110), and (111) wafer, respectively. The shadow region indicates the wafer surface. For (001) wafer, the surface normal or out-of-plane direction is along [001], the longitudinal (channel) direction is along [110], and the transverse direction, which is perpendicular to the channel in the plane, is along $[\bar{1}\bar{1}0]$. The biaxial stress for (001) wafer is along [100] and [010] directions with the same magnitude of stress, that is, $\sigma_{[100]} = \sigma_{[010]}$. For (110) wafer, the surface normal direction is along [110]. The $[\bar{1}\bar{1}0]$ direction is chosen as the channel direction for higher hole mobility in the plane [19]. The transverse direction is along $[00\bar{1}]$. For (111) wafer, the surface normal is along [111], the longitudinal direction is along $[\bar{1}\bar{1}0]$, and the transverse direction is along $[11\bar{2}]$. The stress directions for the three wafer orientations are also summarized in Table 2.2. Note that (110) and (111) wafers have no so-called biaxial stress since the longitudinal and transverse direction are not

symmetric in silicon crystal.

In addition, the channel directions are indeed the same on (001), (110), and (111) wafer since the [110] and $[\bar{1}10]$ have the same symmetry in silicon crystal; however, the normal and transverse directions are different. Thus, if additional normal or transverse stresses exist in devices, it would induce different band structures among these wafer orientations.

Using the discussion in Section 2.1, the stress tensors and strain tensors for biaxial stress on (001) wafer, uniaxial stress along [110], $[\bar{1}10]$, [001], [111], and $[11\bar{2}]$ direction can be obtained and listed in Table 2.3. By the principle of linear superposition, the resultant strain tensor in response to the combination of normal, longitudinal, and transverse stress for the three wafer orientations are also obtained and given in Table 2.4. Note that although the normal, longitudinal, and transverse stresses on (001) and (110) wafer are along different directions, they are indeed among the same set of stress directions, that is, [110], $[\bar{1}10]$, and [001]. That implies the same strain-altered band structures can be achieved on (001) and (110) wafer with the corresponding stresses included.

2.5 Results and Discussion

2.5.1 Band Structures

Applying Table 2.4 and Equations (2.12)-(2.16), the calculations of strain-altered band structures on the three wafer orientations with various stress conditions are straightforward.

As discussed before, the band warping of silicon conduction band remains unchanged (band edge shift will be discussed in next section). The valence band structures with various strain conditions including unstressed bulk silicon, 1GPa

uniaxial longitudinal compression, 1GPa uniaxial longitudinal tension, 1GPa uniaxial transverse compression, and 1GPa uniaxial transverse tension, are shown in Fig. 2.6, 2.8, and 2.9 for (001), (110), and (111) wafer, respectively. Fig. 2.7 also shows the 1GPa biaxial compressive and tensile stress on (001) wafer. The right hand side of the figures is along the out-of-plane direction, and the left hand counterpart is along the channel direction. Moreover, the band structures are plotted in electron energy, that is, more positive value at energy axis represents smaller hole energy. The effective masses along normal and channel direction for the three lowest bands are also marked in the figures. The three lowest valence bands in Fig. 2.6-2.9 are denoted as top, second, and third band since the designations, heavy, light, and split-off, lose their meanings under stress. For example, Fig. 2.6(b) shows the band structure of bulk silicon under uniaxial compressive stress on (001) wafer. The top band along [001] direction is “heavy-hole like” and second band is “light-hole like,” but along [110] direction, the situation is reverse: the top band becomes “light-hole like” and second band is “heavy-hole like.”

2.5.2 Strain-induced Band Edge Shift

In order to give insight into the trends of strain-altered band structures from small to large strain, there are two characteristics of band structures that should be considered. One is band edge shift discussed in this section, and the other is band warping which will be modeled into effective masses and extracted in Chapter 3.

Using Equation (2.12) and Table 2.4, the band edge shift of the six conduction band minima along the $\langle 100 \rangle$ directions can be obtained. Note that the first term of Equation (2.13) shifts the six valleys in the same magnitude while the second term splits the Δ_4 valleys (the conduction band minima along [100], $[\bar{1}00]$, [010], and $[0\bar{1}0]$ directions) and Δ_2 valleys (the minima along [001] and $[00\bar{1}]$ directions) since

$\varepsilon_{xx} = \varepsilon_{yy} \neq \varepsilon_{zz}$ for all stress types in the discussion. Also note that associated with compressive (tensile) strain in one direction, there are generally a tensile (compressive) strain in the other two directions. Thus, the signs of ε_{xx} (ε_{yy}) and ε_{zz} are opposite for a single uniaxial or biaxial stress. On the other hand, with the combination of the normal, longitudinal, and transverse stress, the ε_{xx} (ε_{yy}) and ε_{zz} may be produced with the same sign. However, it indeed favors opposing sign for increasing the population in the lowest subband and enhancing mobility.

Using Table 2.4 and Equation (2.14)-(2.16) with $k_x = k_y = k_z = 0$, the strain-induced valence subband energy shift can be obtained since the valence band minima for bulk silicon are all at gamma point (see Fig. 2.6-2.9). The three lowest valence band edges versus stress with uniaxial longitudinal, uniaxial transverse stress are shown in Fig. 2.10, 2.13, and 2.14 for (001), (110), and (111) wafer, respectively. Fig. 2.11 also shows the biaxial stress case on (001) wafer. The negative value of stress indicates compressive stress and the positive value indicates tensile stress. Note that the band edge shift under uniaxial longitudinal stress on (001), (110), and (111) wafer, and uniaxial transverse stress on (001) wafer are the same since these stress directions have the same symmetry in silicon crystal.

The figures also label the quantization effective mass, which is along the direction normal to the surface, for top two bands. The “hh” denotes the effective mass of the corresponding band as “heavy-hole like” while “lh” is “light-hole like” among the two bands. It is interesting that no matter whether the stress is uniaxial longitudinal, uniaxial transverse, or biaxial on the (001) wafer, under the compressive stress the first band is heavy-hole like and the second band is light-hole like. Nevertheless, under tensile stress, the situation is reverse. This is the main mechanism

accounting for the reverse trends of the change of direct tunneling current between compressive and tensile stress. It will be discussed thoroughly in Chapter 5. The analysis can be applied to (110) and (111) wafer as well.

Moreover, the subband energy splitting between top and second band is larger under uniaxial compression (biaxial tension) than uniaxial tension (biaxial compression). The influences will be discussed in chapter 3, 4, and 5.

Next, let us compare the difference between results calculated by the 6×6 Hamiltonian and the 4×4 Hamiltonian. The latter is widely used in the previous works for device modeling [16], [22] since its solutions have very simple form for biaxial stress on (001) wafer [Equation (2.19)] and uniaxial stress along [110] [Equation (2.20)]. The solutions can be obtained through Equation (2.18) and Table 2.4. Note that the band edge is proportional to the stress.

$$E_v(k=0) = a(2S_{11} + 4S_{12})\sigma \pm (S_{11} - S_{12})b|\sigma| \quad (2.19)$$

$$E_v(k=0) = a(S_{11} + 2S_{12})\sigma \pm \left[\frac{b^2}{4}(S_{11} - S_{12})^2 + \frac{d^2}{16}S_{44}^2 \right]^{1/2} |\sigma| \quad (2.20)$$

On the other hand, the analytic solution of 6×6 Hamiltonian is complex for uniaxial stress along [110] and not listed here due to space limit. However, the solution of that for biaxial stress [Equation (2.21)] is relatively simple since biaxial stress have no shear strain terms and with $\varepsilon_{xx} = \varepsilon_{yy}$, thus, $L_\varepsilon = M_\varepsilon = 0$ in Equation (2.14).

$$E_v(k=0) = -P_\varepsilon - Q_\varepsilon \quad \text{or} \quad -P_\varepsilon - \frac{1}{2}\Delta + \frac{1}{2}Q_\varepsilon \pm \frac{1}{2}[\Delta^2 + 2Q_\varepsilon\Delta + 9Q_\varepsilon^2]^{1/2} \quad (2.21)$$

Fig. 2.12 shows the comparison between the band edge shift calculated by 6×6 (solid line) and 4×4 (dotted line) Hamiltonian under uniaxial and biaxial stress on (001) wafer. It can be seen that under uniaxial or biaxial stress, one of the top two bands can be approximated by a straight line, hence the use of Equations (2.19) and

(2.20) can get fairly good results. However, the other band is far from the linear line calculated by 4×4 Hamiltonian and even the lowest energy is not located at zero stress, that is, it first decreases and then increases while the stress increases. Therefore, the usage of analytic solutions derived from 4×4 Hamiltonian can only serve for very small stress and induces significant error under moderate and large stress as shown in Fig. 2.12. For this reason, we will apply the 6×6 Hamiltonian throughout our simulation work in Chapter 2, 3, and 4.

2.5.3 Constant Energy Surface

Constant energy surface in k-space is also an important tool for estimating the influences of strain and can be obtained from Equation (2.12) for conduction band and (2.14) for valence band. Fig. 2.16, 2.17, and 2.18 show the constant energy surface in k-space of bulk silicon for three lowest valence bands with 1GPa uniaxial longitudinal, uniaxial transverse, biaxial stress on (001) wafer, respectively. For comparison, Fig. 2.15 also shows the case of unstressed bulk silicon (the results are consistent with Ref. [23]). The three coordinate axes are along k_x , k_y , and k_z . The figures also label the effective masses along normal, longitudinal, transverse, and other principal directions. In addition, constant energy surface for bulk silicon under 1GPa uniaxial longitudinal and uniaxial transverse on (110) and (111) are shown in Fig. 2.19-2.22. Note that, in these figures, the three coordinate axes are along the normal, longitudinal, and transverse directions.

2.5.4 Two-dimensional Energy Contour in the Plane of Wafer Surface

The two-dimensional energy contour in the plane of wafer surface can help us determine the characteristics of inversion layer of MOSFETs including the conductivity effective mass, transverse effective mass, density of states, and the

symmetry of E-k relation under various stress conditions.

The energy contour of valence band can be obtained by Equation (2.14) and setting the wavevector along normal direction at zero. The results are plotted in Fig. 2.23-2.30 for various stress conditions and wafer orientations as discussed above. Note that the horizontal and vertical axes are along k_x and k_y for (001) wafer and, contrary to that, they are along the longitudinal and transverse directions for (110) and (111) wafers.

2.5.5 Advantageous Strains and Wafer Orientations

The general expression of conductivity for n- or p-MOSFETs operating in inversion condition can be described by

$$\text{Conductivity} = q \left[n_1 \left(\frac{q\tau_1}{m_{c1}} \right) + n_2 \left(\frac{q\tau_2}{m_{c2}} \right) \right] \quad (2.22)$$

where q , n , τ , and m_c are the elementary charge, carrier density, scattering relaxation time, and conductivity effective mass along channel direction, respectively. The subscript denotes the first and second subband in the inversion layer of MOSFETs.

For high performance and low power requirements, *advantageous* strains need to meet following criteria [2], [24]-[26]: (1) small conductivity effective mass of the lowest subband, m_{c1} , for enhancing the mobility since most of carriers occupy the lowest subband; (2) large quantization effective mass along the out-of-plane direction of the lowest subband, which enhances the carrier population by lowering the quantization energy in the inversion layer; (3) large 2D DOS effective mass, or large transverse effective mass, of the lowest subband which also increases the carrier population of the lowest subband; (4) large energy splitting of the two lowest subbands for lowering the intervalley (optical phonon) scattering; and (5) the strain-induced subband shift and confinement effect in inversion layer are additive,

that is, the band shifted down by strain must also have a larger quantization effective mass, whereas the band shifted up by strain must have a smaller quantization effective mass. The requirement not only enhances mobility due to increased carrier population in lowest subband which have small conductivity effective mass, but also reduces the power dissipation due to decreased gate direct tunneling current (details will be discussed in Chapter 4).

Let us first examine the potential stress types and wafer orientations with these criteria for nMOSFETs, then, for pMOSFETs. The quantization, conductivity, and DOS effective masses of the lowest subbands for nMOSFETs operating in inversion conditions are given by [27]-[29] and listed in Table. 2.5. For conservative reason, we assume the stress is not large enough to perturb significantly the original system described in [27]-[29]. Under this assumption, the effective masses keep constant under strain, that is, strain has no influences on the criteria 1-3. In addition, the total carrier density in inversion layer does not change significantly when the carriers repopulate from one subband to another subband due to the strain-induce subband energy shift.

For criterion 5, uniaxial longitudinal, uniaxial transverse, and biaxial tension are advantageous strains for (001) wafer since these strains lift the $\Delta 4$ valleys, which have smaller quantization effective mass, and shift down the $\Delta 2$ valleys, which have larger quantization effective mass [see Equation (2.13) and Table 2.4]. On the other hand, the uniaxial longitudinal compression are advantageous strains for (110) wafer since these strains lift the $\Delta 2$ valleys, which have smaller quantization effective mass, and shift down the $\Delta 4$ valleys, which have larger quantization effective mass. Note that the $\Delta 4$ valleys are the conduction band minima along $[100]$, $[\bar{1}00]$, $[010]$, and $[0\bar{1}0]$ directions while $\Delta 2$ valleys are the minima along $[001]$ and $[00\bar{1}]$ directions on both (001) and (110) wafer [27]. For the (111) wafer, the six valleys are degenerate

in inversion layer and have the same conductivity effective mass, that is, the strain-induced subband energy shift does not provide additional benefits for the conductivity.

For comparing the (001) and (110) wafer, let us consider the same carriers concentration in inversion layer on (001) and (110) wafer. The quantization effective mass of the lower valleys on (001) wafer is much larger than that of (110) wafer while for higher valleys, it remains the same. That is, the occupation ratio of the lower valleys is larger on (001) wafer than that on (110) wafer due to the much lower subband energy of lower valleys compared to higher valleys on (001) wafer. In addition, the conductivity effective mass of the lower valleys is smaller on (001) wafer than that on (110) wafer while for the higher valleys it is equivalent on both wafers. Moreover, the magnitudes of strain-induced subband energy shift are equivalent since the directions of uniaxial longitudinal stress on (001) and (110) wafers have the same crystal symmetry. Therefore, the conductivity on (001) wafer is better than that on (110) wafer. However, experiments and accurate numerical simulations must be conducted to corroborate this argument.

Next, let us examine these stress types and wafer orientations for pMOSFETs using the criteria, the simulation results, Fig. 2.6-2.30, and the effective masses summarized in Table 2.6. For criterion 5, the disadvantageous strains producing smaller quantization effective mass for top band and larger quantization effective mass for second band are marked with a strikethrough on the quantization effective mass. Then, for criteria 1-3, the advantageous strains producing smallest conductivity effective mass, largest transverse effective mass, and best quantization effective mass among these stress types and wafer orientations are emphasized with bold effective mass.

In Table 2.6, it can be seen that the uniaxial longitudinal compression on both

(001) and (110) wafers is better among all advantageous strains. For uniaxial longitudinal compression on (001) wafer, it can provide smallest conductivity effective mass and largest transverse effective mass of the top band, but the quantization effective masses are not as desirable as that on (110) wafer. On the other hand, uniaxial longitudinal compression on (110) wafer can provide the smallest conductivity effective mass as that on (100) wafer, the largest quantization effective mass of the top band, and the smallest quantization effective mass of the second band, which not only increases the carrier population in top band, but also reduces the gate direct tunneling current. However, the transverse effective masses are small comparing with that on (001) wafer. Moreover, the magnitudes of strain-induced band edge shift on both wafers are equivalent as shown in Fig. 2.10(a) and Fig. 2.13(a). Indeed, there are reported simulation results [26] indicating that the mobility on (110) wafer is larger than that on (001) wafer below about 1.3GPa, but the situation is reverse above 1.3GPa. Nevertheless, the conductivity and total drive current, which relate to the carrier density and occupation ratio of each subband, were not reported in the work. Therefore, there are advantages and disadvantages on each wafer orientation, but for low power application, (110) wafer may be better than (001) wafer.

2.5.6 Influences of Additional Transverse or Normal Stress

In Section 2.5.5, we concluded that uniaxial and biaxial tensile stresses on (001) wafer favor the conductivity enhancement for nMOSFETs while it is the uniaxial longitudinal compressive stress on both (001) and (110) wafer for pMOSFETs. Then, in this section, we focus on the influences on these advantageous stress with *additional* uniaxial transverse stress, or normal stress, which is existent in process such as capping layer or STI stressor when the dimension of channel width is comparable with channel length.

Let us first consider an additional transverse stress on (001) wafer, or an additional normal stress on (110) wafer with the same sign, that is, compressive stress, and magnitude of the longitudinal stress. It is possible in process such as capping layer or STI stressor. Table 2.4 shows that the shear strain term is canceled while the normal strain term is doubled. Thus, the strain tensors reduce to the form as biaxial compressive stress on (001) wafer (a pure normal stress). It is not desirable for pMOSFETs since the benefits of longitudinal compressive stress is degraded.

Next, let us consider additional transverse stress on (001) wafer, or normal stress on (110) wafer, with the opposing sign, that is, tensile stress, and the same magnitude of longitudinal stress. [Note that uniaxial longitudinal compressive and transverse tensile stresses are both advantageous strains on (001) wafer as shown in Fig. 2.6(e), Fig. 2.17(b), Fig. 2.25(b), and Table 2.6.] Table 2.4 shows that the normal strain terms are canceled while the shear strain term doubles. Thus, the strain tensors readily reduce to a pure shear strain. It is not desirable in nMOSFETs since there is no energy splitting between the $\Delta 2$ and $\Delta 4$ valleys due to the normal strain terms being zero. Thus, the mobility enhancement of nMOSFETs by uniaxial longitudinal stress is degraded. For pMOSFETs, Fig. 2.31 shows the band structures, constant energy surfaces, and 2D energy contours of bulk silicon with addition transverse stress on (001), and (110) and the effective masses are summarized in Table. 2.7. It can be found that with additional transverse tensile stress on (001) wafer, the conductivity effective mass remains $0.12m_0$ for top band, but that reduced from $0.59m_0$ to $0.3m_0$ for second band. In addition, the transverse effective mass of top band increases from $1.37m_0$ to $1.88m_0$. Note that the simulated results for additional normal tensile stress on (110) wafer are similar to that for an additional transverse tensile stress on (001) wafer, but the normal and transverse direction are exchanged. Thus, additional transverse tensile stress on (001) wafer can further enhance the hole mobility while

additional normal tensile stress on (110) wafer can further reduce the gate direct tunneling current (the quantization effective mass of top band increase from $1.37m_0$ to $1.88m_0$). On the other hand, additional transverse tensile stress have no apparent benefits on (110) wafer as shown in Table 2.7.

To introduce the additional transverse tensile stress on (001) wafer for enhancing hole mobility, it is possible to be achieved without additional costs by modifying slightly the standard strained CMOS logic technology process flow [1]. The undertaken technology enhances the electron and hole mobility on the same wafer by first using SiGe source/drain to introduce longitudinal compressive stress in the channel of pMOSFETs and then introduces longitudinal tensile stress in the channel of nMOSFETs by applying nitride capping layer on both nMOSFETs and pMOSFETs. The disadvantage of this process flow is that it needs additional step for neutralizing the capping layer strain on pMOSFETs. However, instead of the longitudinal tensile stress with the nitride capping layer, if the tensile stress is incorporated along the transverse direction during the same step, which not only enhances the electron mobility in the same order of magnitude, but also introduces additional hole mobility enhancement. (Remind that the longitudinal and transverse directions are symmetry in silicon crystal. Thus, the energy splitting of the $\Delta 2$ and $\Delta 4$ valleys are equivalent under these two type stresses. Moreover, effective masses remain unchanged in conduction band).

2.6 Conclusion

In this chapter, the strain tensors have been expressed as a function of normal, longitudinal, and transverse stress on (001), (110), and (111) wafers, respectively. Then, the strain-altered band structures, band edge shifts, constant energy surface, 2D energy contour, and effective masses for various stress conditions and wafer

orientations have been calculated by deformation potential theory and $k \cdot p$ framework for conduction band and valence band, respectively. Utilizing these simulated results as tools to estimate the device performance, the best advantageous strains among these stress types and wafer orientations for nMOSFETs have shown to be uniaxial and biaxial tension on (001) wafer while for pMOSFETs they are uniaxial longitudinal compression on both (001) and (110) wafer. Finally, we have examined the influences of additional transverse or normal strain and have found that the additional transverse tensile stress on (001) wafer can further enhance the hole mobility.



Chapter 3

The Properties of Bulk Silicon in the Presence of Strain

3.1 Introduction

In order to model the characteristics of strained MOSFETs such as the change of gate direct tunneling current (Chapter 4), there are two important features of strain-altered band structure that should be taken into consideration. One is the strain-induced band edge shift, which has been discussed and extracted in Chapter 2. The other is the strain-induced band warping, which will be incorporated into our physical model (developed in Chapter 4) via the effective masses extracted in this chapter such as the quantization effective mass, the 2D density of state (DOS) effective mass, and 3D DOS effective mass. In Chapter 4, we will verify qualitatively and quantitatively that the strain-induced change of gate direct tunneling current can be attributed to these two features of strain-altered band structure. Moreover, utilizing the extracted 3D DOS effective masses and band edge shifts of all valleys, the conduction band effective DOS, N_c , and valence band effective DOS, N_v , can be determined. Then, following the approach of conventional “Semiconductor Device Physics,” [30], [31] the strain-altered Fermi energy level of bulk silicon, which is an important physical parameter for device modeling, can be determined. Finally, the strain-altered intrinsic carrier density of bulk silicon will be calculated as well.

Note that in Chapter 3 and 4, it is primarily focused on the silicon under uniaxial longitudinal stress and biaxial stress on (001) wafer since there are adequate

experimental data published by previous works and widely used in industry to date. Nevertheless, the approach and analysis developed here can be applied directly to other stress conditions and wafer orientations with extracted physical parameters.

3.2 Effective Mass

As discussed in Chapter 2, the conduction band effective mass of bulk silicon remains unchanged under strain. For the valence band, we assume that the constant energy surfaces can be approximated to ellipsoids, that is, the energy dispersion relations along the three axes of the ellipsoid are parabolic-like. Thus, the energy dispersion relation of bulk silicon near the gamma point can be expressed as

$$E = \frac{\hbar^2 k_a^2}{2m_a^*} + \frac{\hbar^2 k_b^2}{2m_b^*} + \frac{\hbar^2 k_c^2}{2m_c^*} \quad (3.1)$$

where k_a , k_b , and k_c are the wavevectors along the three axes of the ellipsoid, a , b , and c directions, respectively. m_a , m_b , and m_c are the effective masses along a , b , and c directions, respectively. For uniaxial stress, the directions along $[110]$, the longitudinal direction, along $[\bar{1}\bar{1}0]$, the transverse direction, and along $[001]$, the normal direction, in k -space are selected to be the three orthogonal axes of the ellipsoid due to the symmetry of uniaxial strain as shown in Fig. 2.16 and Fig. 2.24. On the other hand, for biaxial stress, the direction of $[100]$, $[010]$, and $[001]$ in k -space are selected to be the three orthogonal axes of the ellipsoid due to the symmetry of biaxial strain as shown in Fig. 2.18 and Fig. 2.16. Note that the effective masses along $[100]$, $[010]$, $[110]$, and $[\bar{1}\bar{1}0]$ are the same under biaxial stress due to the symmetry of silicon crystal and biaxial strain. Therefore, for biaxial stress, the energy contour is circle-like near the gamma point under large strain, while for uniaxial stress, the energy contour is ellipse-like.

Also, note that the constant energy surfaces, or 2D energy contours, of the heavy

hole band of unstrained bulk silicon, as shown in Fig. 2.15 and Fig. 2.23, are indeed far from the ellipsoid or ellipse in the plane. Thus, for small strain case, the assumption of elliptic constant energy surface is not suitable. However, the approach used in Ref. [32] for deriving the effective masses of unstrained silicon cannot be applied directly to the strained case due to the complex form of energy dispersion relation under strain. In addition, the analytic solution used in [32] for heavy and light hole band are extracted from the 4×4 Hamiltonian described in Chapter 2, which ignores the mixing effect of split-off band and hence induces significant errors as compared with the 6×6 Hamiltonian. Moreover, the conventional effective masses given by the Ref. [30]-[32] for the unstrained case are extracted from bulk silicon. They are not applicable to describe the inversion layer of MOSFETs. Thus, the one band effective mass approximation is adopted in Chapter 4 for the small strain case instead of the values extracted here. On the other hand, when the strain is large enough, the crystal symmetry of band structure will be destroyed and forced to the strain symmetry. Thus, the hypothetical elliptic constant energy surface is a good approximation.

Next, the effective masses along the three axes of the ellipsoid can be defined as

$$m_{ai} = \hbar^2 \left(\frac{\partial^2 E_i}{\partial k_a^2} \right)^{-1}, \quad m_{bi} = \hbar^2 \left(\frac{\partial^2 E_i}{\partial k_b^2} \right)^{-1}, \quad m_{ci} = \hbar^2 \left(\frac{\partial^2 E_i}{\partial k_c^2} \right)^{-1} \quad (3.2)$$

where E is the energy and the subscript i denotes the i th valleys.

Consequently, based on the assumption of elliptic constant energy surface, the 3D (bulk) DOS effective mass can be derived as

$$m_{di} = (m_{ai} m_{bi} m_{ci})^{\frac{1}{3}}. \quad (3.3)$$

On the other hand, assuming energy contour in k_x - k_y plane is ellipse-like, the energy in inversion layer of MOSFETs can be expressed as

$$E = \frac{\hbar^2 k_a^2}{2m_a^*} + \frac{\hbar^2 k_b^2}{2m_b^*} + E_{inz} \quad (3.4)$$

where the E_{inz} is the quantization energy along the z direction. The subscript i and n denote the n th subband of i th valley. Then, the 2D DOS effective mass in inversion layer can be derived as

$$m_{di} = (m_{ai} m_{bi})^{\frac{1}{2}} \quad (3.5)$$

Fig. 3.1 shows the effective masses along the three axes of the ellipsoid, $m_{[110]}$, $m_{[\bar{1}10]}$, and $m_{[001]}$, versus uniaxial longitudinal stress for three lowest valence bands. Note that some of these effective masses vary significantly from small to large strain while the others remain almost constant. Thus, the influences of strain-altered effective masses cannot be ignored and must be incorporated into our physical model. It can be seen that the longitudinal (conductivity) effective mass of top band under compressive stress is much smaller than that under uniaxial tensile stress. It is consistent with the analysis in Chapter 2. Especially, the transverse and quantization effective mass increase while the uniaxial compressive stress increases. It implies that introducing larger strain into the channel is beneficial and desirable. Fig. 3.2 shows the 3D (bulk) and 2D DOS effective masses versus uniaxial longitudinal stress for three lowest valence bands. It can be observed that the 3D and 2D DOS effective masses of top band increase significantly while the uniaxial compressive stress increases from zero to 3GPa.

Fig. 3.3 shows the effective masses along the three axes of the ellipsoid, $m_{[100]}$, $m_{[010]}$, and $m_{[001]}$, versus biaxial stress for three lowest valence bands. The $m_{[100]}$ and $m_{[010]}$ are equivalent due to the strain and crystal symmetry. Then, Fig. 3.4 shows the

3D and 2D DOS effective masses versus biaxial stress for three lowest valence bands. Note that the 3D DOS effective masses for the three lowest valence bands appear to remain constant (about $0.24m_0$) due to the reverse trends between $m_{[100]}$ ($m_{[010]}$) and $m_{[001]}$ while the compressive or tensile strain increases from zero to 3GPa.

3.3 Carrier Density and Effective DOS

3.3.1 Electrons in Conduction Band

To derive the expression of carrier density of bulk silicon with non-degenerate doping as a function of band shifts and 3D DOS effective masses of all valleys, Fig. 3.5(a) shows the strain-induced energy valleys splitting for conduction band under arbitrary stress. The E_1 , E_2 , E_3 represent, respectively, the energy of conduction band minima along one of the three orthogonal axes, k_x , k_y , or k_z . Note that for uniaxial and biaxial compressive stress on (001) wafer, the E_1 and E_2 are degenerate and are the valley minima along k_x , and k_y axes while E_3 is the valley minima along k_z axis and higher than E_1 and E_2 . On the other hand, for uniaxial and biaxial tensile stress, the E_2 and E_3 are degenerate and are the valley minima along k_x , and k_y axes while E_1 is the valley minima along k_z axis and lower than E_2 and E_3 . In addition, the $\Delta E_{1,2}$ represents the band splitting between E_1 and E_2 while $\Delta E_{1,3}$ represents the band splitting between E_1 and E_3 . Then the carrier density of electron in conduction band can be expressed as

$$\begin{aligned}
 n_0 &= N_{C1} e^{-\frac{(E_C - E_F)}{k_B T}} + N_{C2} e^{-\frac{[(E_C + \Delta E_{1,2}) - E_F]}{k_B T}} + N_{C3} e^{-\frac{[(E_C + \Delta E_{1,3}) - E_F]}{k_B T}} \\
 &= \left(N_{C1} + N_{C2} e^{-\frac{\Delta E_{1,2}}{k_B T}} + N_{C3} e^{-\frac{\Delta E_{1,3}}{k_B T}} \right) e^{-\frac{(E_C - E_F)}{k_B T}} \\
 &= N_C^* e^{-\frac{(E_C - E_F)}{k_B T}}
 \end{aligned} \tag{3.6}$$

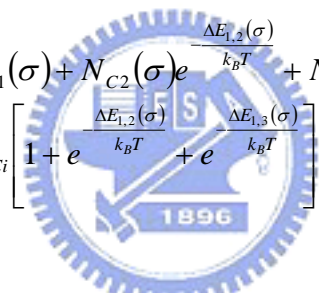
where E_f is the Fermi energy. The N_{c1} , N_{c2} , and N_{c3} are the effective DOS of the E_1 , E_2 , and E_3 , respectively, and can be expressed as

$$N_{Ci} = 2 \left(\frac{m_{di} k_B T}{2\pi\hbar^2} \right)^{\frac{3}{2}}. \quad (3.7)$$

Reminding that the strain does not alter the band warping in conduction band, and therefore, the 3D DOS effective masses remain unchanged, leading to the expression:

$$m_{d1}, m_{d2}, m_{d3} = 2^{\frac{2}{3}} \left(m_t^{*2} m_l^* \right)^{\frac{1}{3}}. \quad (3.8)$$

Consequently, the N_{c1} , N_{c2} , and N_{c3} are equivalent. Therefore, the expression of electron carrier density can be further simplified as shown in Equation (3.6) where the N_C^* is the *effective* conduction band effective DOS under stress:

$$\begin{aligned} N_C^*(\sigma) &= N_{C1}(\sigma) + N_{C2}(\sigma) e^{\frac{\Delta E_{1,2}(\sigma)}{k_B T}} + N_{C3}(\sigma) e^{\frac{\Delta E_{1,3}(\sigma)}{k_B T}} \\ &= N_{Ci} \left[1 + e^{\frac{\Delta E_{1,2}(\sigma)}{k_B T}} + e^{\frac{\Delta E_{1,3}(\sigma)}{k_B T}} \right] \end{aligned} \quad (3.9)$$


3.3.2 Holes in Valence Band

Similar to the case of conduction band, Fig. 3.5(b) shows the schematic strain-induced energy valleys splitting for the three lowest valence bands. Thus, the carrier density of hole in valence band can be expressed by

$$\begin{aligned} p_0 &= N_{V,top} e^{\frac{(E_f - E_V)}{k_B T}} + N_{V,second} e^{\frac{[E_f - (E_V - \Delta E_{1,2})]}{k_B T}} + N_{V,third} e^{\frac{[E_f - (E_V - \Delta E_{1,3})]}{k_B T}} \\ &= \left(N_{V,top} + N_{V,second} e^{\frac{\Delta E_{1,2}}{k_B T}} + N_{V,third} e^{\frac{\Delta E_{1,3}}{k_B T}} \right) e^{\frac{(E_f - E_V)}{k_B T}} \\ &= N_V^* e^{\frac{(E_f - E_V)}{k_B T}} \end{aligned} \quad (3.10)$$

where the $N_{V,top}$, $N_{V,second}$, and $N_{V,third}$ are the effective DOS of the three lowest valence bands, respectively, and can be determined by the 3D DOS effective masses shown in

Fig. 3.2 and 3.4 for uniaxial and biaxial stress, respectively. Therefore, one can write

$$N_{v_i} = 2 \left(\frac{m_{di} k_B T}{2\pi\hbar^2} \right)^{\frac{3}{2}}. \quad (3.11)$$

Then, the *effective* valence band effective DOS under stress, N_v^* , can be expressed as

$$N_v^*(\sigma) = N_{v_1}(\sigma) + N_{v_2}(\sigma) e^{-\frac{\Delta E_{1,2}(\sigma)}{k_B T}} + N_{v_3}(\sigma) e^{-\frac{\Delta E_{1,3}(\sigma)}{k_B T}}. \quad (3.12)$$

3.3.3 Simulated Results of N_c^* and N_v^*

Fig. 3.6 and Fig. 3.7 show the conduction and valence effective DOS, N_c and N_v , versus uniaxial and biaxial stress, respectively. It can be seen that for both uniaxial and biaxial stress, the N_c and N_v drop very quickly when the stress increases from zero to 1GPa, but almost remain constant above 1GPa. The phenomena can be explained by Equation (3.9) and (3.12). That is, the second and third terms in Equation (3.9) and (3.12) decrease exponentially due to the energy splitting increase when the stress increases (see Fig. 2.10 and 2.11). Ultimately, the second and third terms tend to zero, thus, N_c and N_v are dominated by the first term under large strain. Note that, it is different from the biaxial case, the N_v increases slightly when the uniaxial compressive stress increases. It can be explained by the 3D DOS effective mass of the top valence band under uniaxial stress (see Fig. 3.2), which increases significantly when the uniaxial stress increases from zero to 3GPa while for biaxial stress it remains almost constant (see Fig. 3.4).

3.4 Fermi Energy of Bulk Silicon

Using the strain-induced shift of conduction band edge extracted in Chapter 2 and the strain-altered conduction effective DOS extracted in previous section, the Fermi energy of n-type silicon under strain can be expressed as [30], [31]

$$E_c(\sigma) - E_f(\sigma) = -k_B T \ln\left(\frac{n_0}{N_c^*(\sigma)}\right). \quad (3.13)$$

Likewise, using the strain-induced shift of valence band edge and the strain-altered valence effective DOS, the Fermi energy of p-type silicon under strain can be expressed as [30], [31]

$$E_f(\sigma) - E_v(\sigma) = -k_B T \ln\left(\frac{p_0}{N_v^*(\sigma)}\right). \quad (3.14)$$

Finally, the strain-altered intrinsic Fermi energy level, E_i , can be determined by

$$E_i(\sigma) = \left(\frac{E_c + E_v}{2}\right) + \frac{k_B T}{2} \ln\left(\frac{N_v^*(\sigma)}{N_c^*(\sigma)}\right). \quad (3.15)$$

Fig. 3.8 and Fig. 3.9 show the Fermi energy of bulk silicon versus uniaxial and biaxial stress, respectively, for various doping concentrations. The figures also show how the intrinsic Fermi level, conduction band edge, and valence band edge vary with stress. Note that the band gap of unstrained silicon is 1.12eV . From Fig. 3.8, Equation (3.13), and Equation (3.14), it can be observed that the strain-induced conduction band edge shift decreases the Fermi energy of n-type silicon while the strain-induced valence band edge shift increases the Fermi energy of p-type silicon when the stress becomes large. On the other hand, the energy difference between conduction band edge and the Fermi energy of n-type silicon, or the energy difference between valence band edge and Fermi energy of p-type silicon, reduces since the DOS effective masses decrease while stress increases. Thus, different from the influences of band edge shift, the effective DOS introduces reverse influences on the strain-altered Fermi energy. Moreover, the strain-altered Fermi energies are primary dominated by the band edge shift under stress above 1GPa since the effective DOS of conduction and valence band both tend to constant when the stress becomes large.

3.5 Intrinsic Carrier Concentration

Utilizing the conduction and valence effective DOS of bulk silicon under strain extracted in Section 3.4 and the strain-induced band gap narrowing, which enhances the intrinsic carrier density, extracted in Chapter 2 and 3.4., the intrinsic carrier density can be obtained as

$$n_i = \sqrt{N_C^*(\sigma)N_V^*(\sigma)}e^{-E_G(\sigma)/2k_B T} \quad (3.16)$$

where $E_G(\sigma)$ is the band gap of bulk silicon under strain. k_B is the Boltzmann constant and T is temperature.

Fig. 3.10 shows the intrinsic carrier concentration versus uniaxial and biaxial stress. In the figure, it can be seen that the intrinsic carrier density increases slightly under 1GPa and enhances quickly above 1GPa. In addition, the intrinsic carrier density increases faster under biaxial stress than that under uniaxial stress. The phenomena can be understood by Equation (3.16), Fig. 3.6, and Fig. 3.7. For the stress under 1GPa, the conduction and valence effective DOS reduce quickly, thus suppressing the enhancement of intrinsic carrier density due to the band gap narrowing. On the other hand, when the stress becomes large, the effective DOS tends to constant. Thus, the intrinsic carrier density is primary dominated by the band gap narrowing and increases quickly when stress becomes large. Moreover, the strain-induced band gap narrowing is larger under biaxial stress than that under uniaxial stress as shown in Fig. 3.8 and Fig. 3.9. Therefore, the enhancement of intrinsic carrier density is larger under biaxial stress than that under uniaxial stress.

3.6 Conclusion

In this chapter, the quantization effective masses, the 2D DOS effective masses,

and the 3D DOS effective masses of silicon under uniaxial and biaxial stress on (001) wafer have been extracted. These extracted effective masses determine the characteristics of inversion layer in MOSFETs such as the quantization subband energy, occupation ratio of each subband, and the Fermi energy. In addition, the strain-altered conduction and valence effective DOS have been derived as a function of the strain-induced band edge shift and strain-altered 3D DOS effective mass. From the calculated results, the effective DOS drops quickly due to the band edge splitting when stress increases from zero to 1GPa, and then tends to a constant determined by 3D DOS effective mass of lowest valley for further increased stress. Furthermore, the Fermi energy of bulk silicon with non-degenerate doping has also been derived as a function of the strain-induced conduction or valence band edge shifts and the strain-altered effective DOS. The calculated results have shown that the Fermi energy is dominated by band shifts under large stress because the effective DOS tends to constant. Finally, the intrinsic carrier concentration has been derived and expressed as a function of strain-altered effective DOS and strain-induced band gap narrowing. The calculated results have shown that the intrinsic carrier density increases rapidly due to the strain-induced band gap narrowing when the stress is larger than 1GPa.

Chapter 4

Strain-induced Change of Gate Direct Tunneling Current

4.1 Introduction

There are two approaches to study the conduction band electron direct tunneling (EDT) current in unstrained nMOSFETs. One is the self-consistent Schrödinger-Poisson equation [5]. Another is triangular potential approximation [33], [34], [41]. The triangular potential approximation was also applied successfully to the hole direct tunneling (HDT) current of valence band [3], [42]. However, the physical parameters used in above studies were extracted from energy dispersion relationship (band structure) of bulk silicon. The actual dispersion relation of valence band in the channel inversion condition possesses many non-ideal properties such as band mixing, anisotropic, far from parabolic, camel back, vertical electric field-dependent, and the density of state function is deviated from the step-like function [4], [35]-[37] as shown in Fig. 1(a) for unstressed case and (b) for uniaxial longitudinal compressive stress. In Fig. 1, note that the energy of the heavy, light, and split-off spin-orbit hole band are degenerated and zero at gamma point in bulk silicon without stress.

The actual dispersion relation and the corresponding calculation procedure are too complex so that for further applications are impractical. Fortunately, the improved one band effective mass approximation (improved one band EMA) introduced in Ref. [4], [35]-[37], [42] can resolve this difficulty. This approach can achieve both the reasonably accuracy and computing efficiency.

On the other hand, the dispersion relation of valence band with external stress using six-band $k \cdot p$ method has been deeply developed [19]. Moreover, using the six-band $k \cdot p$ method and Self-consistent Schrödinger-Poisson equation to calculate hole tunneling current in pMOSFETs with various type of stress has been report [6].

In particular, there is an analytic expression for subband energy shift of conduction band under longitudinal uniaxial stress, which is a function of vertical electric field and stress [38]. Furthermore, using the analytic expression and measured electron gate direct tunneling current, it has been corroborated that the expression can be used to extract the conduction band deformation potential constant [38] and quantify channel stress in devices [39].

However, there is no available procedure, which is based on the triangular potential approximation and strain-altered dispersion relationship of silicon, to calculate the hole direct tunneling current. Therefore, in this work, model and characterize direct tunneling current in MOSFETs under uniaxial compressive stress by using the modified triangular potential approximation is demonstrated.

The simulation result can provide information for future strain engineering and later calculation. Furthermore, the model can provide an explicit physical picture for the impact of strain on the gate direct tunneling current in MOSFETs.

In this chapter, we focus on the direct tunneling current for pMOSFETs under uniaxial longitudinal compressive stress on (001) wafer, then, extend that for nMOSFETs. The same approach and analysis can be applied to other stress conditions and wafer orientation with corresponding modifications of the model.

4.2 Physical Model

4.2.1 Hole Subband Energy and Carrier Density (pMOSFETs)

Fig. 4.2 shows the band diagram of a pMOSFETs under uniaxial compressive stress (note that the band diagram may be different for other stress conditions) and biased in channel inversion condition. The figure also illustrates the quantized subband energies in the inversion layer and HDT current from the channel into the gate. $E_{C(unstressed)}$ and $E_{V(unstressed)}$ are the conduction and valence band edge in bulk silicon without external stress. E_F is the Fermi energy. $E_{C(\Delta 2)}$ and $E_{C(\Delta 4)}$ indicate the strain-induced conduction band edge shift of the $\Delta 2$ and $\Delta 4$ valleys of bulk silicon, respectively. $E_{V1}(F_{Si}=0, \sigma)$, $E_{V2}(F_{Si}=0, \sigma)$, $E_{V3}(F_{Si}=0, \sigma)$ indicate the strain-induced valence band edge shift of the three lowest bands of bulk silicon. $E_{V1}(F_{Si}, \sigma)$, $E_{V2}(F_{Si}, \sigma)$, $E_{V3}(F_{Si}, \sigma)$ are the quantized energy of the three lowest subbands in the inversion layer. Note that under uniaxial compressive stress, the order of three lowest subbands in the inversion layer are indeed the same as the three lowest bands (valleys) of bulk silicon. Φ_{BV} is the valence band edge difference between SiO₂ and Si without stress. t_{ox} is the gate oxide thickness.

In Fig. 4.2, the energy band bending induced by gate voltage in the inversion layer can be approximated by a triangular potential well. The slope of the triangular potential well can be modeled by the silicon surface electric field F_{Si} . Analogizing to Ref. [38], we assume that the impact of strain-induced band edge shift and the electric-field-induced subband energy confinement in the inversion layer are independent. Therefore, we can express the three lowest valence subband energy in the inversion layer by directly adding the triangular potential component, first term in the right hand side in Equation (4.1), and stress component, second term, as

$$E_{v1} = \left(\frac{\hbar^2}{2m_{z1}} \right)^{1/3} \left(\frac{9}{8} \pi q F_{Si} \right)^{2/3} + \Delta E_{v1}(\sigma), \quad (4.1a)$$

$$E_{v2} = \left(\frac{\hbar^2}{2m_{z2}} \right)^{1/3} \left(\frac{9}{8} \pi q F_{Si} \right)^{2/3} + \Delta E_{v2}(\sigma), \quad (4.1a)$$

and

$$E_{v3} = \left(\frac{\hbar^2}{2m_{z3}} \right)^{1/3} \left(\frac{9}{8} \pi q F_{Si} \right)^{2/3} + \Delta + \Delta E_{v3}(\sigma) \quad (4.1a)$$

where m_{z1} , m_{z2} , and m_{z3} are the quantization effective masses of the three lowest subbands, respectively, $\Delta E_{v1}(\sigma)$, $\Delta E_{v2}(\sigma)$, and $\Delta E_{v3}(\sigma)$ indicate the quantity of valence band edge shifts between strained and unstrained bulk silicon for the three lowest subbands, respectively. The split-off spin-orbit energy of bulk silicon is $\Delta = 44\text{meV}$ [35], [37].

Using 2D density of states and Fermi-Dirac statistic, the carrier density in inversion layer for each subband can be derived as

$$N_n = \left(\frac{kT}{\pi \hbar^2} \right) m_{dn}^* \ln \left(1 + \exp \left(\frac{E_F - E_{vn}}{kT} \right) \right) \quad (4.2)$$

Where m_{dn}^* is the hole DOS effective mass of the n th subband. E_{vn} is the n th subband energy defined by Equation (4.1) for the three lowest subbands.

The relationship between gate voltage V_G and F_{Si} is determined from the voltage balance equation

$$|V_G| = V_{FB} + V_{ox} + V_{poly} + V_S \quad (4.3)$$

where V_{FB} is flat-band voltage, V_{ox} is oxide voltage drop, V_{poly} is the voltage drop in polysilicon gate due to poly depletion, and V_S is the substrate band bending.

To derive the flat-band voltage for pMOSFETs under arbitrary strain in both polysilicon gate and channel, Fig. 4.3 shows the band diagram of a p^+ polysilicon/SiO₂/n-Si (pMOS) structure with a negative gate voltage. Then, to

establish the energy relation of both side with the help of the band diagram. Next, let $V_{ox} = V_{poly} = V_s = 0$ and $V_G = V_{FB}$, the expression of flat-band voltage can be derived as

$$qV_{FB} = |\Delta E_{CG1}(\sigma_{poly})| - |\Delta E_{CS1}(\sigma_{chan})| + E_{GG}(\sigma_{poly}) + kT \ln\left(\frac{N_{sub}}{N_C(\sigma_{chan})}\right) \quad (4.4)$$

where $\Delta E_{CG1}(\sigma_{poly})$ and $\Delta E_{CS1}(\sigma_{chan})$ are the quantity of conduction band edge shift for polysilicon gate and channel, respectively. The strain-altered band gap of polysilicon gate is $E_{GG} = E_G(\sigma_{poly} = 0) - |\Delta E_{CG1}(\sigma_{poly})| - |\Delta E_{VG1}(\sigma_{poly})|$ as shown in Fig. 4.3. N_{Sub} is the substrate doping concentration and $N_C(\sigma_{poly})$ is the conduction effective DOS described in Chapter 3.

The self-consistent procedure for subband calculation is described as following:

(1) given N_{poly} , t_{ox} , N_{sub} , and V_G . (2) Let $V_{ox} = \frac{k}{N}|V_G - V_{FB}|$ where $0 \leq k \leq N$ since the voltage drop of oxide must be between zero to $|V_G - V_{FB}|$. It is noteworthy that increasing the value of N will increase the accuracy of simulated results, but the computation time increases as well. (3) Using the equations summarized in Table 4.1 to calculate subband energies, carrier density of each subband, voltage drop, depletion charge, etc. (4) Examine the calculated results with Poisson equation, or the conservation of electric flux, $q(N_{inv} + N_{depl}) \approx \epsilon_{ox} F_{ox}$. Then, find the value of k and the corresponding solution with smallest error between the both sides of the electric flux conservation equation.

4.2.2 Hole Direct Tunneling Current for pMOSFETs

After modifying the subband energy expression and subband calculation

procedure for the strained silicon, we can readily apply the well-developed WKB approximation [3], [4], and [34] to calculate the tunneling current density. The hole direct tunneling current density J_G can be expressed as a sum of the tunneling current contribution of each subbands,

$$J_G = q \sum_n \frac{N_n}{\tau_n(E_{vn})}, \quad (4.5)$$

where N_n is the inversion carrier density of the n th subband and τ_n is the lifetime of the n th subband. The lifetime of an n th subband in the triangular potential well can be expressed as [3], [4]

$$\frac{1}{\tau_n(E)} = \frac{T(E)}{\int_0^{z_n} \sqrt{2m_{zn}^* [E - E_V(z)]} dz} = T(E) \times \frac{qF_{Si}}{4} \left(\frac{m_{zn}E}{3} \right)^{-1/2} \quad (4.6)$$

where z_n is the classical turning point of the n th subband, $E_V(z)$ is the Si valence band edge, $T(E)$ is the transmission probability of a carrier. Transmission probability can be written in the form of

$$T(E) = T_{WKB}(E) \cdot T_R(E) \quad (4.7)$$

where $T_{WKB}(E)$ is the typical WKB approximation of the transmission probability, and T_R is the correction factor taking into account the reflections from boundaries of the oxide. Applying parabolic dispersion relationship in the oxide [3], the $T_{WKB}(E)$ can be simplified as

$$T_{WKB}(E) = \exp \left[-\frac{2}{\hbar} \int_0^{t_{ox}} \sqrt{2m_{oxh} (E - qV(z))} dz \right] = \exp \left(\frac{4\sqrt{2m_{oxh}} (\varphi_{cath}^{3/2} - \varphi_{an}^{3/2})}{3q\hbar |F_{ox}|} \right) \quad (4.8)$$

where m_{oxh} is the effective hole mass, F_{ox} is the oxide electric field, φ_{cath} is the barrier height of tunneling hole with quantized energy E_{vn} at cathode side, and φ_{an} is that at anode side. $\varphi_{cath} = \Phi_{BV} - qV_{ox} - E_{vn}$ and $\varphi_{an} = \Phi_{BV} - E_{vn}$. The reflection

correction factor is expressed as

$$T_R(E) = \frac{4\nu_{Si}(E)\nu_{ox}(\varphi_{an})}{\nu_{Si}^2(E) + \nu_{ox}^2(\varphi_{an})} \times \frac{4\nu_{Si}(E + qV_{ox})\nu_{ox}(\varphi_{cath})}{\nu_{Si}^2(E + qV_{ox}) + \nu_{ox}^2(\varphi_{cath})} \quad (4.9)$$

where $\nu_{Si}(E)$ and $\nu_{Si}(E + qV_{ox})$ are the group velocity of the electron incident and leaving the oxide, respectively, and $\nu_{ox}(\varphi_{an})$ and $\nu_{ox}(\varphi_{cath})$ are the magnitudes of the purely imaginary group velocity of hole at the cathode and anode side within the oxide. $\nu_{Si}(E_{vn}) = \sqrt{2E_{vn}/m_{zn}}$ and $\nu_{ox}(E_{vn}) = \sqrt{2(\Phi_{BV} - E_{vn} - qV_{ox}(z))/m_{oxh}}$ for the parabolic dispersion relationship.

4.2.3 Electron Direct Tunneling Current for nMOSFETs

Fig. 4.4 illustrates the band diagram of an n^+ polysilicon/SiO₂/p-Si structure biased in channel inversion condition and stressed with uniaxial longitudinal compressive stress. The figure also shows the subband energy confinement in the inversion layer and the electron direct tunneling current from channel to gate. Similar to pMOSFETs, the strain-altered subband energy can be expressed as

$$E_{ci(\Delta 2)} = \left(\frac{\hbar^2}{2m_{z(\Delta 2)}} \right)^{1/3} \left(\frac{3}{2} q\pi F_{Si} \left(i - \frac{1}{4} \right) \right)^{2/3} + \Delta E_{c(\Delta 2)}(\sigma) \quad (4.10a)$$

$$E_{ci(\Delta 4)} = \left(\frac{\hbar^2}{2m_{z(\Delta 4)}} \right)^{1/3} \left(\frac{3}{2} q\pi F_{Si} \left(i - \frac{1}{4} \right) \right)^{2/3} + \Delta E_{c(\Delta 4)}(\sigma) \quad (4.10b)$$

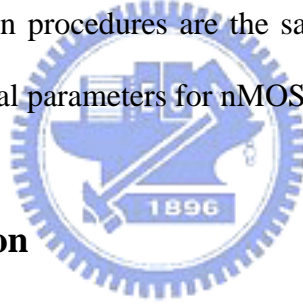
where the $\Delta E_{c(\Delta 2)}(\sigma)$ and $\Delta E_{c(\Delta 4)}(\sigma)$ are the strain-induced conduction band edge shift for the $\Delta 2$ and $\Delta 4$ valleys, respectively. The details for calculating $\Delta E_{c(\Delta 2)}(\sigma)$ and $\Delta E_{c(\Delta 4)}(\sigma)$ have been introduced in Chapter 2. The subscript i denotes the i th subband of each valleys. $m_{z(\Delta 2)}$ and $m_{z(\Delta 4)}$ are the quantization effective mass for the $\Delta 2$ and $\Delta 4$ valleys, respectively. As discussed in Chapter 2 and 3, the

quantization, 2D DOS, and 3D DOS effective mass are independent of strain for silicon conduction band. The values of the quantization and 2D DOS effective masses are given in Table 2.5. In addition, the strain-altered flat-band voltage for nMOSFETs under arbitrary strain in both polysilicon gate and channel can be derived with the help of the band diagram as shown in Fig. 4.5.

$$qV_{FB} = |\Delta E_{CG1}(\sigma_{poly})| - |\Delta E_{CS1}(\sigma_{chan})| - E_G(\sigma_{chan}) - kT \ln\left(\frac{N_{sub}}{N_V(\sigma_{chan})}\right) \quad (4.11)$$

where $E_G = E_G(\sigma_{chan} = 0) - |\Delta E_{CS1}(\sigma_{chan})| - |\Delta E_{VS1}(\sigma_{chan})|$ is the strain-altered band gap of channel as shown in Fig. 4.5. $N_V(\sigma_{chan})$ is the valence effective DOS described in Chapter 3.

The remaining calculation procedures are the same as that for pMOSFETs, but with the corresponding physical parameters for nMOSFETs.



4.3 Results and Discussion

4.3.1 Hole Direct Tunneling Current for pMOSFETs

4.3.1.1 Parameters Extraction for the Vertical Electric Field Component

For simplification, we assume that quantization and density of state effective mass are constant and have no significant change within the range of vertical electric field and stress in our calculation.

Using the triangular potential approximation and improved one-band EMA, Equations (4.1) with $\sigma = 0$, we can extract the quantization effective masses for the three lowest subbands. The quantization effective masses are the only adjustable parameter in Equation (4.1) with $\sigma = 0$ and the values for best fitting are as follows:

$m_{z1} = 0.28m_0$, $m_{z2} = 0.23m_0$, and $m_{z3} = 0.21m_0$. These values are consistent with

the values used in [4], [35]-[37] for unstressed case ($m_{z1}^* = 0.29m_0$, $m_{z2}^* = 0.24m_0$, and $m_{z3}^* = 0.22m_0$) and approximated the value used in [6] for longitudinal uniaxial compressive case ($m_{z1}^* = 0.27m_0$, $m_{z2}^* = 0.22m_0$, and $m_{z3}^* = 0.23m_0$).

Fig. 4.6 shows that the hole subband energy ($\sigma = 0$) evaluated by the improved one band EMA, which provides better computing efficiency and takes the non-ideal properties of dispersion relationship in channel inversion condition into account, well reproduced the results calculated by accurate six-band $k \cdot p$ method (with the self-consistent Schrödinger-Poisson equation) for the three lowest subbands versus F_{Si} varying from zero to 2.5MV/cm. Thus, the use of constant values for quantization effective mass is applicable.

For simplification, we adopt the density of state effective mass suggested by [36] for channel inversion and unstressed condition. Furthermore, we assume that the density of state effective mass do not have significant change under small stress condition. However, it is noteworthy that for large stress or precise computation, the change of density of state effective mass should be taken into consideration.

4.3.1.2. Calculation for the Stress Component (Valence Band Edge Shifts)

The method for calculating valence band edge shifts has been discussed in Chapter 2. Fig. 4.7 shows the hole subband energies calculated by Equation (4.1) with the quantization effective masses extracted above. The figure also shows the data evaluated by the six-band $k \cdot p$ method (with the self-consistent Schrödinger-Poisson equation).

It can be observed that our model can well reproduce the data calculated by six-band $k \cdot p$ method within the range, F_{Si} varies from 0.5MV/cm to 1.5MV/cm and

the stress varies from zero to 300MPa. Note that comparing to the subband energy and the thermal energy $kT=0.026$ eV at room temperature, the error is tolerated for later calculation. Moreover, in usual operation of pMOSFETs, which oxide thickness is thinner than 2nm, the gate voltage is between zero to 1.5V and the corresponding F_{Si} is between around 0.5MV/cm to 1.5MV/cm. Therefore, the assumption, the influences of strain-induced subband energy shift is independent of F_{Si} , is appropriate within the range of F_{Si} and σ in our discussion.

Fig. 4.8 shows the strain-induced band edge shifts in bulk silicon for both the conduction and valence band. The level of zero energy is the conduction and valence band edge without external stress, respectively.

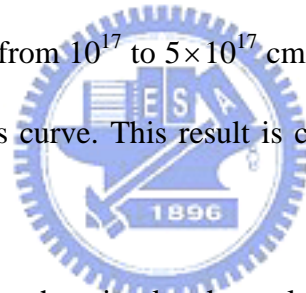
4.3.1.3. Hole Direct Tunneling Current

Our model has been verified that it can well reproduce the experimental data published by previous works, HDT current in Ref. [3], [4] and EDT current in [34], for unstrained silicon with various gate oxide thickness and doping concentration.

Then, using our model and the parameters extracted above, the simulation result, $\Delta J_G / J_G$ versus stress at $V_G=1V$, was calculated and plotted in Fig. 4.9(a). The device parameters used in simulation are as following: gate oxide thickness is 1.3nm; polysilicon and substrate doping concentration are $5 \times 10^{19} \text{ cm}^{-3}$ and 10^{17} cm^{-3} , respectively. The figure also shows the experimental data published by former works. The squares is the data measured at $V_G=1V$ in Ref. [2]. The diamonds are the data measured by four point bending jig at $V_G=1V$ for the device samples consisting of heavily doped poly-silicon gate, 1.3nm physical thickness SiO_2 gate dielectrics, and $\sim 5 \times 10^{17} \text{ cm}^{-3}$ well doping in Ref. [40]. The circles are the data measured by wafer

bending technique at $V_G=1V$ for the device samples with 10^{17} cm^{-3} n-type substrate doping and 1.3nm physical thickness nitrated SiO_2 gate insulators in Ref. [6].

In our calculation, the carrier density of third subband is only about 2% of total three subbands. Thus, according to Fermi-Dirac statistic, contribution of higher subbands is negligible [37]. Also note that the assumption of parabolic dispersion relationship in oxide is precise at $V_G=1V$ and oxide thickness is thinner than 2nm with $m_{oxh}=0.4m_0$ [3], [4]. Moreover, since the experimental data cited from Ref. [6] and [40] are measured by the wafer bending technique, the stress type and magnitude of polysilicon gate are set to be the same as that of channel [16]. Furthermore, the doping effects on the tunneling currents have been examined. It was identified that when substrate doping varies from 10^{17} to $5 \times 10^{17} \text{ cm}^{-3}$, there is no significant change on the $\Delta J_G / J_G$ versus stress curve. This result is consistent with the experimental data.



It can be observed that the simulated result of $\Delta J_G / J_G$ versus stress is consistent with the trend of experimental data published in Ref. [2], [6], but with some deviation at larger stress.

Fig. 4.9 also shows the corresponding subband energy, carrier density, and the hole direct tunneling current versus stress for the three lowest subbands. According to simulated results, the strain-induced change of HDT current is primarily results from the carrier repopulation. Under longitudinal uniaxial compressive stress, the first subband energy become lower and the second and third subbands become higher than that in unstressed case as shown in Fig. 6(b). Consequently, according to the Fermi-Dirac statistic, a number of carriers redistribute from second and third subbands into the first subband as shown in Fig. 6(c). Note that the total carrier

density remains almost constant with the stress varying from zero to 300MPa. In addition, the barrier for hole tunneling of first subband is higher and corresponding WKB transmission probability is smaller than other subbands. Therefore, the total tunneling current decreases while the stress increases as shown in Fig. 6(d).

The deviation between the experimental data and simulation results at larger stress may result from the use of constant 2D DOS effective mass in our calculation. Fig. 2.23, 2.24 and 3.2 shows that the 2D DOS effective mass of the first band indeed increase while that of the second band decreases at larger stress. Consequently, there are indeed more carriers repopulate from higher subband into the first subband than that expected by the model. Thus, the HDT current further reduced.

4.3.1.4 Uniaxial Transverse Stress

It can be observed that the experimental data measured in Ref. [2], [40] have the same trend and magnitude of the strain-induced change of HDT current under uniaxial longitudinal and transverse stress. This phenomenon can also be expected in our model since the strain-induced valence band edge shifts and the 2D DOS effective masses are equivalent under longitudinal and transverse stress on (001) wafer.

4.3.2 Electron Direct Tunneling Current for nMOSFETs

Fig. 4.10 shows the simulated results for nMOSFETs under uniaxial longitudinal compressive stress. Note that the calculation includes the first two subbands of $\Delta 2$ valleys and the first subband of $\Delta 4$ valleys since the subband energy of second subband of $\Delta 2$ valleys are close to that of the first subband of $\Delta 4$ valleys as shown in Fig4.10(b). The circles are the experimental data measured by four-point bending jig at $V_G=1V$ for the device samples consisting of arsenic doped polysilicon gate,

1.3nm nitrated SiO₂ gate dielectric, and 10^{17} cm^{-3} boron doped p well in Ref. [38]. The diamonds and squares are the data from Ref. [2] and [40] as described in the pMOSFETs case. It can be seen that the simulation results well reproduce the experimental data. The mechanism for the change of EDT current can also be explained by the carrier repopulation. Under uniaxial compressive stress, the lowest subband ($\Delta 2$ valleys) shifts up while the second subband ($\Delta 4$ valleys) shifts down as shown in Fig. 4.8(a) and Fig. 4.10(b). Consequently, a number of carriers repopulate from the lowest subband to the second subband, which has lower tunneling barrier. In addition, the barrier of the lowest subband also decreases. Thus, the EDT current increases. Note that this mechanism is reverse to that for pMOSFETs under uniaxial compressive stress. Moreover, the analysis for these two cases can also be applied to explain the change of direct tunneling current under other stress conditions.

Fig. 4.11 shows the simulation results for different substrate doping concentration, $5 \times 10^{17} \text{ cm}^{-3}$ and 10^{17} cm^{-3} . It can be seen that the change of EDT current for 10^{17} cm^{-3} doping concentration are smaller than that for $5 \times 10^{17} \text{ cm}^{-3}$. The results are also consistent with the experimental data.

4.4 Conclusion

Using the modified subband energy expression of triangular potential approximation and the WKB approximation, we have demonstrated an efficient and reasonably accurate physical model to calculate HDT and EDT current for longitudinal uniaxial compressive stressed silicon device. The improved one band EMA and the data calculated by six-band $k \cdot p$ method were used to extract the quantization effective mass. The simulated results correspond to the experimental data, $\Delta J_G / J_G$ versus σ , published by former work.

In our model, the subband energy is a function of vertical electric field and stress.

Therefore, this model can be used directly to characterize the J_G - V_G curve and be applied easily to different stress conditions on various wafer orientations with extracting the corresponding physical parameters.



Chapter 5

Conclusions

In the chapter 2, the strain tensors have been expressed as a function of normal, longitudinal, and transverse stress on (001), (110), and (111) wafers, respectively. Then, the strain-altered band structures, band edge shifts, constant energy surface, 2D energy contour, and effective masses for various stress conditions and wafer orientations have been calculated by deformation potential theory and $k \cdot p$ framework for conduction and valence band, respectively. Utilizing these simulated results as tools to estimate the device performance, we concluded that the best advantageous strains among these stress types and wafer orientations for nMOSFETs have shown to be uniaxial and biaxial tension on (001) wafer while for pMOSFETs they are uniaxial longitudinal compression on both (001) and (110) wafer. Finally, we have examined the influences of additional transverse or normal strain and have found that the additional transverse tensile stress on (001) wafer can further enhance the hole mobility.

In chapter 3, the quantization effective masses, the 2D DOS effective masses, and the 3D DOS effective masses of silicon under uniaxial and biaxial stress on (001) wafer have been extracted. In addition, the strain-altered conduction and valence effective DOS have been derived as a function of the strain-induced band edge shift and strain-altered 3D DOS effective mass. From the calculated results, the effective DOS drops quickly due to the band edge splitting when stress increases from zero to 1GPa, and then tends to a constant determined by 3D DOS effective mass of lowest valley for further increased stress. Furthermore, the Fermi energy of bulk silicon with

non-degenerate doping has also been derived as a function of the strain-induced conduction or valence band edge shifts and the strain-altered effective DOS. The calculated results have shown that the Fermi energy is dominated by band shifts under large stress because the effective DOS tends to constant. Finally, the intrinsic carrier concentration has been derived and expressed as a function of strain-altered effective DOS and strain-induced band gap narrowing. The calculated results have shown that the intrinsic carrier density increases rapidly due to the strain-induced band gap narrowing when the stress is larger than 1GPa.

In Chapter 4, a triangular potential approximation based physical model for HDT current in pMOSFETs and EDT current in nMOSFETs under longitudinal uniaxial compressive stress has been presented. A modified subband energy expression, which comprises the vertical electric field component and stress component, is used to evaluate the subband energy in the inversion layer of MOSFETs under gate bias and stress. Then, an improved one band effective mass approximation and data calculated by six-band $k \cdot p$ method are used to extract quantization effective mass. Moreover, WKB approximation is utilized to evaluate transmission probability and tunneling current. The simulated results agree with the experimental data published by former works. The primarily reason accounting for the decrease of HDT current for pMOSFETs while increase uniaxial compressive stress is that a number of carriers redistribute from higher subband into the lowest subband due to the stress induced subband energy shift. Since the barrier of the lowest subband for hole tunneling is higher and the corresponding transmission probability is smaller than other subbands, the total tunneling current decreases while stress increases. The reverse mechanism of above can also be used to explain the opposite trend of EDT current for nMOSFETs under uniaxial compressive stress. Thus, the proposed model provides a simple method to assess the influence of external stress for direct tunneling

currents in MOSFETs qualitatively and quantitatively. Moreover, with extracting the corresponding physical parameters, our model can be applied directly to various wafer orientations and different stress conditions. For example, the device with different magnitude and type of stress in poly gate and channel. Alternatively, the longitudinal and transverse stresses exist in the device in the meantime.



References

- [1] S. E. Thompson, M. Armstrong, C. Auth, M. Alavi, M. Buehler, R. Chau, S. Cea, T. Ghani, G. Glass, T. Hoffman, C.-H. Jan, C. Kenyon, J. Klaus, K. Kuhn, Z. Ma, B. McIntyre, K. Mistry, A. Murthy, B. Obradovic, R. Nagisetty, P. Nguyen, S. Sivakumar, R. Shaheed, L. Shifren, B. Tufts, S. Tyagi, M. Bohr, and Y. El-Mansy, "A 90-nm logic technology featuring strained-silicon," *IEEE Trans. Electron Devices*, vol. 51, no. 11, pp. 1790-1797, 2004.
- [2] S. E. Thompson, G. Sun, Y. S. Choi, and T. Nishida, "Uniaxial-process-induced strained-Si: extending the CMOS roadmap," *IEEE Trans. Electron Devices*, vol. 53, no. 5, pp. 1010-1020, 2006.
- [3] K. N. Yang, H. T. Huang, M. C. Chang, C. M. Chu, Y. S. Chen, M. J. Chen, Y. M. Lin, M. C. Yu, M. Jang, C. H. Yu, and M. S. Liang, "A physical model for hole direct tunneling current in p^+ poly-gate pMOSFETs with ultrathin gate oxides," *IEEE Trans. Electron Devices*, vol. 47, no. 11, pp. 2161-2166, 2000.
- [4] Y. T. Hou, M. F. Li, Y. Jin, and W. H. Lai, "Direct tunneling hole currents through ultrathin gate oxides in metal-oxide-semiconductor devices," *J. Appl. Phys.*, vol. 91, no. 1, pp.258-264, 2002.
- [5] S. H. Lo, D. A. Buchanan, Y. Taur, and W. Wang, "Quantum-mechanical modeling of electron tunneling current from the inversion layer of ultra-thin-oxide nMOSFET's," *IEEE Electron Device Lett.*, vol. 18, pp. 209-211, 1997.
- [6] X. Yang, J. Lim, G. Sun, K. Wu, T. Nishida, and S. E. Thompson, "Strain-induced changes in the gate tunneling currents in p-channel metal-oxide-semiconductor field-effect transistors," *Appl. Phys. Lett.*, vol. 88, pp. 052 108, 2006.
- [7] Roy R. Craig, Jr., *Mechanics of materials second edition*, John Wiley & Sons Inc., 1999.
- [8] H. A. Rueda, "Modeling of mechanical stress in silicon isolation technology and its influence on device characteristics," dissertation of degree of doctor of philosophy, university of Florida, 1999.
- [9] Wikipedia (http://en.wikipedia.org/wiki/Main_Page)
- [10] Fusahito Yoshida, "Fundamentals of elastic plastic mechanics," KYORITSU SHUPPAN Co., Ltd., 1997.
- [11] Y. Kanda, "A graphical representation of the piezoresistance coefficients in Silicon," *IEEE Trans. Electron Devices*, Vol. ED-29, no. 1, pp. 64-70, 1982.
- [12] Y. Kanda, "Effect of stress on Germanium and Silicon p-n junctions," *Jpn. J.*

- Appl. Phys.*, Vol. 6, No. 4, pp. 475-486, 1967.
- [13] MEMS and nanotechnology clearinghouse (<http://www.memsnet.org/material/>)
- [14] Almaz Optics, Inc. (<http://www.almazoptics.com/material.htm>)
- [15] KORTH KRISTALLE GMBH (<http://www.korth.de/eng/index.htm>)
- [16] J.-S. Lim, S. E. Thompson, and J. G. Fossum, "Comparison of threshold-voltage shifts for uniaxial and biaxial tensile-stressed n-MOSFETs," *IEEE Electron Device Lett.*, Vol. 25, no. 11, pp. 731-733, 2004.
- [17] C. Herring and E. Vogt, "Transport and deformation-potential theory for many-valley semiconductors with anisotropic scattering," *Phys. Rev.*, Vol. 101, no. 3, pp. 944-961, 1956.
- [18] Y. Sun, S. E. Thompson, and T. Nishida, "Physics of strain effects in semiconductors and metal-oxide-semiconductor field-effect transistors," *J. Appl. Phys.* **101**, 104503, 2007.
- [19] M. V. Fischetti, Z. Ren, P. M. Solomon, M. Yang, and K. Rim, "Six-band $k \cdot p$ calculation of the hole mobility in silicon inversion layers: dependence on surface orientation, strain, and silicon thickness," *J. Appl. Phys.*, vol. 94, no. 2, pp. 1079-1095, 2003.
- [20] M. Cardona and F. H. Pollak, "Energy-band structure of germanium and silicon - $k \cdot p$ method," *Phys. Rev.*, Vol. 142, no. 2, pp. 530-543, 1966.
- [21] S. Rodríguez, J. A. López-Villanueva, I. Melchor, and J. E. Carceller, "Hole confinement and energy subbands in a silicon inversion layer using the effective mass theory," *J. Appl. Phys.*, Vol. 86, no. 1, pp. 438-444, 1999.
- [22] I. Balslev, "Influence of uniaxial stress on the indirect absorption edge in Silicon and Germanium," *Phys. Rev.*, Vol. 143, no. 2, pp. 636-647, 1966.
- [23] M. Lundstrom, *Fundamentals of carrier transport second edition*, Cambridge, 2000.
- [24] N. Mohta and S. E. Thompson, "Mobility enhancement-the next vector to extend Moore's law," *IEEE CIRCUITS & DEVICES MAGAZINE*, pp. 18-23, 2005.
- [25] Y. Sun, G. Sun, S. Parthasarathy, S. E. Thompson, "Physics of process induced uniaxially strained Si," *Materials Science and Engineering B*, 135, pp. 179-183, 2006.
- [26] S.E. Thompson, S. Suthram, Y. Sun, G. Sun, S. Parthasarathy, M. Chu, and T. Nishida, "Future of strained Si/semiconductors in nanoscale MOSFETs," *Invited Paper*.
- [27] T. Ando, A. B. Fowler, and F. Stern, "Electronic properties of two-dimensional systems," *Rev. Mod. Phys.*, vol. 54, no. 2, pp. 437-670, 1982.
- [28] F. Stern, "Self-Consistent Results for n-Type Si Inversion Layers," *Phys. Rev. B*,

- vol. 5, no. 12, pp. 4891-4899, 1972.
- [29] F. Stern, W. E. Howard, "Properties of Semiconductor Surface Inversion Layers in the Electric Quantum Limit," *Phys. Rev.*, vol. 163, no. 3, pp. 816-835, 1967.
- [30] B. L. Anderson and R. L. Anderson, *Fundamentals of semiconductor devices first edition*, Mc Graw Hill, 2005.
- [31] D. A. Neamen, *Fundamentals of semiconductor physics and devices first edition*, Mc Graw Hill, 2003.
- [32] S. Takagi, M. Takayanagi, and A. Toriumi, "Characterization of inversion-layer capacitance of holes in Si MOSFET's," *IEEE Trans. Electron Devices*, vol. 46, no. 7, pp. 1446-1450, 1999.
- [33] L. F. Register, E. Rosenbaum, and K. Yang, "Analytic model for direct tunneling current in polycrystalline silicon-gate metal-oxide-semiconductor devices," *Appl. Phys. Lett.*, vol. 74, pp. 457-459, 1999.
- [34] N. Yang, W. K. Henson, J. R. Hauser, and J. J. Wortman, "Modeling study of ultrathin gate oxides using direct tunneling current and capacitance-voltage measurements in MOS devices," *IEEE Trans. Electron Devices*, vol. 46, pp. 1464-1471, July 1999.
- [35] Y. T. Hou and M. F. Li, "A novel simulation algorithm for Si valence hole quantization of inversion layer in metal-oxide-semiconductor devices," *Jpn. Appl. Phys.*, vol. 40, part 2, no. 2B, pp. L144-147, 2001.
- [36] Y. T. Hou and M. F. Li, "Hole quantization effects and threshold voltage shift in pMOSFET—assessed by improved one-band effective mass approximation," *IEEE Trans. Electron Devices*, vol. 48, no. 6, pp. 1188-1193, 2001.
- [37] Y. T. Hou and M. F. Li, "A simple and efficient model for quantization effects of hole inversion layers in MOS devices," *IEEE Trans. Electron Devices*, vol. 48, no. 12, pp. 2893-2898, 2001.
- [38] J. S. Lim, X. Yang, T. Nishida, and S. E. Thompson, "Measurement of conduction band deformation potential constants using gate direct tunneling current in n-type metal oxide semiconductor field effect transistors under mechanical stress," *Appl. Phys. Lett.*, vol. 89, pp. 073 509, 2006.
- [39] C. Y. Hsieh and M. J. Chen, "Measurement of channel stress using gate direct tunneling current in uniaxially stressed nMOSFETs," *IEEE Electron Device Lett.*, vol. 28, no. 9, pp. 818-820, 2007.
- [40] X. Yang, Y. Choi, T. Nishida, and S. E. Thompson, "Gate direct tunneling currents in uniaxial stressed MOSFETs," *IEDST*, pp. 149-152, 2007.
- [41] H. H. Mueller and M. J. Schulz, "Simplified method to calculate the band bending and the subband energies in MOS capacitors," *IEEE Trans. Electron Devices*, vol. 44, no. 9, pp. 1539-1543, 1997.

- [42] Y. T. Hou, M. F. Li, W. H. Lai, and Y. Jin, "Modeling and characterization of direct tunneling hole current through ultrathin gate oxide in p-metal-oxide-semiconductor field-effect transistors" *Appl. Phys. Lett.*, vol. 78, no. 25, pp. 4034-4036, 2001.
- [43] P. Liu, G. Lua, X. Liu, Y. Xia, Y. Chen, Y. Zhou, Y. Li, J. Pan, S. Ge, "Investigation of weak damage in $\text{Al}_{0.25}\text{Ga}_{0.75}\text{As}/\text{GaAs}$ by using RBS/C and Raman spectroscopy," *Phys. Lett. A*, 286, pp. 332-337, 2001.



Table 2.1 The deformation potentials, Luttinger parameters, elastic stiffness constants, and split-off energy for Si, Ge, and GaAs.

	Si	Ge	GaAs
a^a (eV)	2.46	1.24	1.16
b^a (eV)	-2.1	-2.9	-2.0
d^a (eV)	-4.8	-5.3	-4.8
γ_1^a	4.22	13.4	6.98
γ_2^a	0.39	4.24	2.06
γ_3^a	1.44	5.69	2.93
S_{11} ($10^{-12} m^2/N$)	7.68 ^b	9.64 ^b	11.75 ^c
S_{12} ($10^{-12} m^2/N$)	-2.14 ^b	-2.6 ^b	-3.65 ^c
S_{44} ($10^{-12} m^2/N$)	12.6 ^b	14.9 ^b	16.8 ^c
Δ_0 (eV)	0.044 ^d	0.29 ^d	0.34 ^d

^aSee Ref. 18.

^bSee Ref. 12.

^cSee Ref. 43.

^dSee Ref 30.



Table 2.2 The normal, longitudinal, and transverse direction for (001), (110), and (111) wafer.

wafer orientation	normal direction (out of plane)	longitudinal direction (in-plane)	transverse direction (in-plane)
(001)	[001]	[110]	$[\bar{1}10]$
(110)	[110]	$[\bar{1}10]$	$[00\bar{1}]$
(111)	[111]	$[\bar{1}10]$	$[11\bar{2}]$



Table 2.3 The stress tensor and strain tensor for biaxial stress on (001) wafer, uniaxial stress along $[110]$, $[\bar{1}10]$, $[001]$, $[111]$, and $[11\bar{2}]$ direction.

	Biaxial ^d	$[110]$	$[\bar{1}10]$	$[001]$	$[111]$	$[11\bar{2}]$
Stress tensor ^a ($\times \sigma_k^c$)	$\begin{bmatrix} 1 \\ 1 \\ 0 \\ 0 \\ 0 \end{bmatrix}$	$\begin{bmatrix} \frac{1}{2} \\ \frac{1}{2} \\ 0 \\ 0 \\ \frac{1}{2} \end{bmatrix}$	$\begin{bmatrix} \frac{1}{2} \\ \frac{1}{2} \\ 0 \\ 0 \\ -\frac{1}{2} \end{bmatrix}$	$\begin{bmatrix} 0 \\ 0 \\ 1 \\ 0 \\ 0 \end{bmatrix}$	$\begin{bmatrix} \frac{1}{3} \\ \frac{1}{3} \\ \frac{1}{3} \\ \frac{1}{3} \\ \frac{1}{3} \end{bmatrix}$	$\begin{bmatrix} \frac{1}{6} \\ \frac{1}{6} \\ \frac{2}{3} \\ -\frac{1}{3} \\ \frac{1}{6} \end{bmatrix}$
Strain tensor ^b ($\times \sigma_k^c$)	$\begin{bmatrix} S_{11} + S_{12} \\ S_{11} + S_{12} \\ 2S_{12} \\ 0 \\ 0 \\ 0 \end{bmatrix}$	$\begin{bmatrix} \frac{1}{2}(S_{11} + S_{12}) \\ \frac{1}{2}(S_{11} + S_{12}) \\ S_{12} \\ 0 \\ \frac{1}{4}S_{44} \end{bmatrix}$	$\begin{bmatrix} \frac{1}{2}(S_{11} + S_{12}) \\ \frac{1}{2}(S_{11} + S_{12}) \\ S_{12} \\ 0 \\ -\frac{1}{4}S_{44} \end{bmatrix}$	$\begin{bmatrix} S_{12} \\ S_{12} \\ S_{11} \\ 0 \\ 0 \end{bmatrix}$	$\begin{bmatrix} \frac{1}{3}(S_{11} + 2S_{12}) \\ \frac{1}{3}(S_{11} + 2S_{12}) \\ \frac{1}{3}(S_{11} + 2S_{12}) \\ \frac{1}{6}S_{44} \\ \frac{1}{6}S_{44} \\ \frac{1}{6}S_{44} \end{bmatrix}$	$\begin{bmatrix} \frac{1}{6}(S_{11} + 5S_{12}) \\ \frac{1}{6}(S_{11} + 5S_{12}) \\ \frac{1}{3}(2S_{11} + S_{12}) \\ -\frac{1}{6}S_{44} \\ -\frac{1}{6}S_{44} \\ \frac{1}{12}S_{44} \end{bmatrix}$

^aThe form of stress tensor is defined by Equation (2.2).

^bThe form of strain tensor is defined by Equation (2.6).

^c σ_k indicates the stress applied along k -direction.

^dFor biaxial stress on (001) wafer, k is along $[100]$ or $[010]$ and $\sigma_{[100]} = \sigma_{[010]}$.

Table 2.4 The resultant strain tensors in response to the combination of normal, longitudinal, and transverse stress for the three wafer orientations

Wafer orientation	Strain tensor
Biaxial stress on (001) wafer	$\begin{bmatrix} (S_{11} + S_{12})\sigma_{[100]} + S_{12}\sigma_{norm} \\ (S_{11} + S_{12})\sigma_{[100]} + S_{12}\sigma_{norm} \\ 2S_{12}\sigma_{[100]} + S_{11}\sigma_{norm} \\ 0 \\ 0 \\ 0 \end{bmatrix}$
Uniaxial stress on (001) wafer	$\begin{bmatrix} \frac{1}{2}(S_{11} + S_{12})(\sigma_{long} + \sigma_{tran}) + S_{12}\sigma_{norm} \\ \frac{1}{2}(S_{11} + S_{12})(\sigma_{long} + \sigma_{tran}) + S_{12}\sigma_{norm} \\ S_{12}(\sigma_{long} + \sigma_{tran}) + S_{11}\sigma_{norm} \\ 0 \\ 0 \\ \frac{1}{4}S_{44}(\sigma_{long} - \sigma_{tran}) \end{bmatrix}$
Uniaxial stress on (110) wafer	$\begin{bmatrix} \frac{1}{2}(S_{11} + S_{12})(\sigma_{norm} + \sigma_{long}) + S_{12}\sigma_{tran} \\ \frac{1}{2}(S_{11} + S_{12})(\sigma_{norm} + \sigma_{long}) + S_{12}\sigma_{tran} \\ S_{12}(\sigma_{norm} + \sigma_{long}) + S_{11}\sigma_{tran} \\ 0 \\ 0 \\ \frac{1}{4}S_{44}(\sigma_{norm} - \sigma_{long}) \end{bmatrix}$
Uniaxial stress on (111) wafer	$\begin{bmatrix} \frac{1}{2}(S_{11} + S_{12})\sigma_{long} + \frac{1}{6}(S_{11} + 5S_{12})\sigma_{ltran} + \frac{1}{3}(S_{11} + 2S_{12})\sigma_{norm} \\ \frac{1}{2}(S_{11} + S_{12})\sigma_{long} + \frac{1}{6}(S_{11} + 5S_{12})\sigma_{ltran} + \frac{1}{3}(S_{11} + 2S_{12})\sigma_{norm} \\ S_{12}\sigma_{long} + \frac{1}{3}(2S_{11} + S_{12})\sigma_{ltran} + \frac{1}{3}(S_{11} + 2S_{12})\sigma_{norm} \\ -\frac{1}{6}S_{44}\sigma_{ltran} + \frac{1}{6}S_{44}\sigma_{norm} \\ -\frac{1}{6}S_{44}\sigma_{ltran} + \frac{1}{6}S_{44}\sigma_{norm} \\ -\frac{1}{4}S_{44}\sigma_{long} + \frac{1}{12}S_{44}\sigma_{ltran} + \frac{1}{6}S_{44}\sigma_{norm} \end{bmatrix}$

Table 2.5 Numerical values of effective mass for silicon conduction band in inversion layer given by [27].

surface	(100)		(110)		(111)
valleys	lower	higher	lower	higher	all
degeneracy	2	4	4	2	6
Normal mass (m_0)	0.916	0.190	0.315	0.190	0.258
Conductivity mass (m_0)	0.190	0.315	0.283	0.315	0.296
DOS effective mass (m_0)	0.190	0.417	0.324	0.417	0.358



Table 2.6 The conductivity, transverse, and quantization effective masses of the top band for bulk silicon with various stress conditions and wafer orientations. The quantization effective masses of the second band are also listed.

wafer	Stress type		$m_{c,1st}(m_0)$	$m_{tran,1st}(m_0)$	$m_{norm,1st}(m_0)$	$m_{norm,2nd}(m_0)$
(001)	Uniaxial	$\sigma < 0$	0.12	1.37	0.28	0.22
	longitudinal	$\sigma > 0$	0.46	0.18	0.21	0.24
	Uniaxial	$\sigma < 0$	1.37	0.12	0.28	0.22
	transverse	$\sigma > 0$	0.18	0.46	0.21	0.24
	Biaxial	$\sigma < 0$	0.22	0.22	0.29	0.27
		$\sigma > 0$	0.28	0.28	0.18	0.29
(110)	Uniaxial	$\sigma < 0$	0.12	0.28	1.37	0.15
	longitudinal	$\sigma > 0$	0.46	0.21	0.18	0.17
	Uniaxial	$\sigma < 0$	0.28	0.18	0.28	0.22
	transverse	$\sigma > 0$	0.22	0.29	0.22	0.22
(111)	Uniaxial	$\sigma < 0$	0.12	0.17	0.47	0.18
	longitudinal	$\sigma > 0$	0.46	0.29	0.19	0.20
	Uniaxial	$\sigma < 0$	0.37	0.23	0.68	0.17
	transverse	$\sigma > 0$	0.19	0.25	0.18	0.19

Table 2.7 Comparison the effective masses between the 1GPa uniaxial longitudinal compressive stress with and without additional 1GPa uniaxial transverse tensile stress for (001) and (110) wafer.

wafer	Additional transverse stress	$m_{c,1st}$ (m_0)	$m_{c,2nd}$ (m_0)	$m_{tran,1st}$ (m_0)	$m_{norm,1st}$ (m_0)	$m_{norm,2nd}$ (m_0)
(001)	Without	0.12	0.59	1.37	0.28	0.22
	With	0.12	0.3	1.88	0.28	0.18
(110)	Without	0.12	0.59	0.28	1.37	0.15
	With	0.12	1.21	0.29	1.32	0.12



Table 4.1. Equations for subband calculation.

Description	Equation
Oxide electric field	$F_{ox} = \frac{V_{ox}}{t_{ox}}$
Potential drop due to poly depletion	$V_{poly} = \frac{\epsilon_{ox}^2 F_{ox}^2}{2q\epsilon_{Si}N_{poly}}$
Substrate band bending	$V_s = V_G - V_{FB} - V_{poly} - V_{ox}$
Quasi-Fermi level	$E_F = qV_s - \left(E_G + kT \ln \left(\frac{N_{sub}}{N_c} \right) \right) \text{ for pMOSFETs}$ $E_F = qV_s - \left(E_G + kT \ln \left(\frac{N_{sub}}{N_v} \right) \right) \text{ for nMOSFETs}$
Silicon surface field	$F_{Si} = \frac{\epsilon_{ox} F_{ox}}{\epsilon_{Si}}$
Subband energies	Equation (4.1) for pMOSFETs Equation (4.10) for nMOSFETs
Inversion carrier density per subband	$N_{ij} = \left(\frac{n_v m_{d_j} kT}{\pi \hbar^2} \right) \ln \left(1 + \exp \left(\frac{E_F - E_{ij}}{kT} \right) \right)$
Total inversion layer carrier per area	$N_{inv} = \sum N_{ij}$
Total inversion QM channel thickness	$Z_{ij} = \frac{2\epsilon_{Si} E_{ij}}{3q\epsilon_{ox} F_{ox}}$
Average QM channel thickness	$Z_{QM} = \sum \frac{Z_{ij} N_{ij}}{N_s}$
Silicon potential drop	$V_{depl} = V_s - \frac{qN_s Z_{QM}}{\epsilon_{Si}} - \frac{kT}{q}$
Ionized impurity density per area	$N_{depl} = \sqrt{\frac{2\epsilon_{Si} V_{depl} N_{sub}}{q}}$

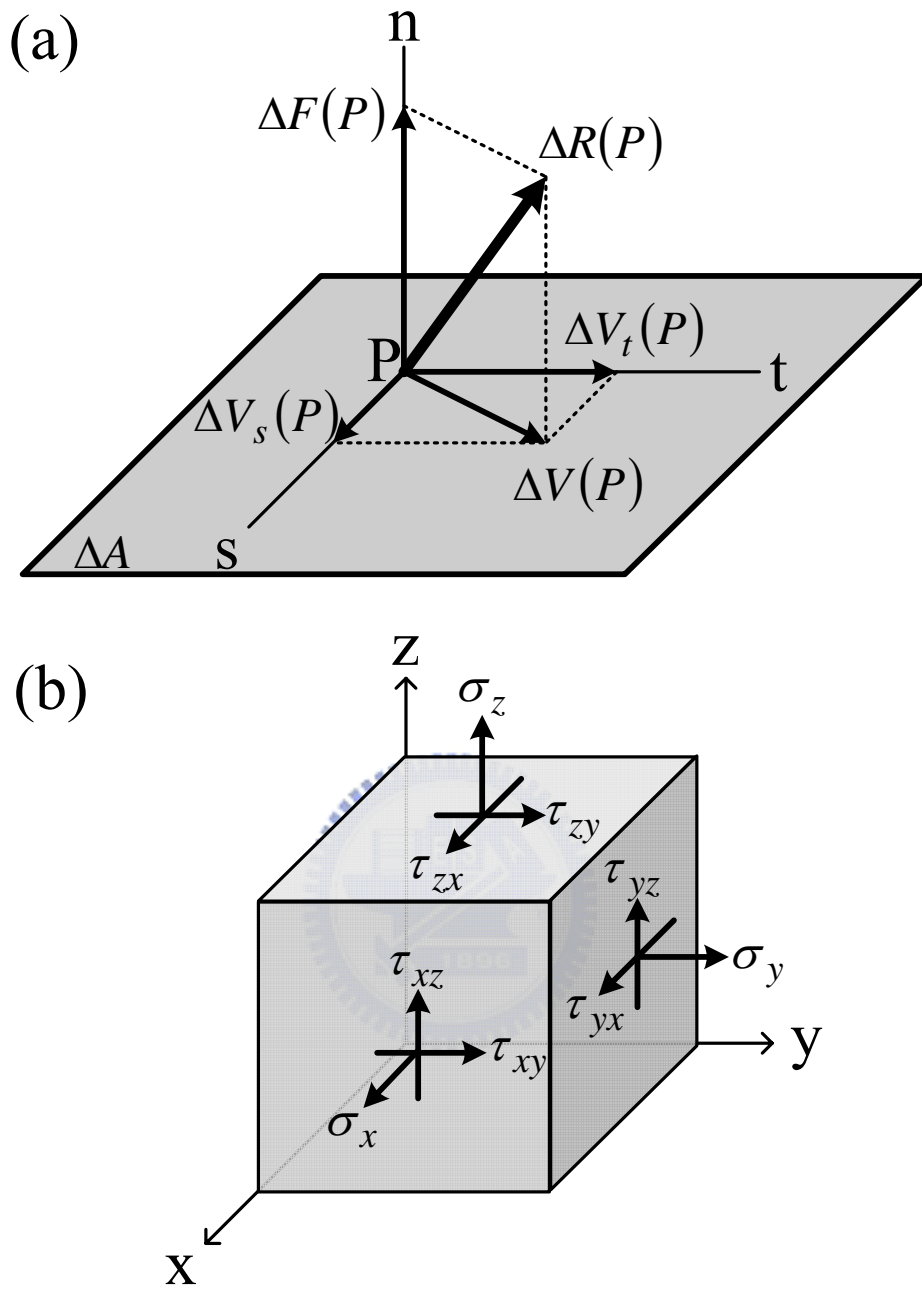


Fig. 2.1. (a) An arbitrary force $\Delta R(P)$ acting on an infinitesimal area ΔA at point P . The normal component of the force is $\Delta F(P)$ and the tangential components of the force are $\Delta V_s(P)$ and $\Delta V_t(P)$ along two orthogonal directions in the plane. (b) Schematic of the nine components defining the stress state at an arbitrary point in three dimensions.

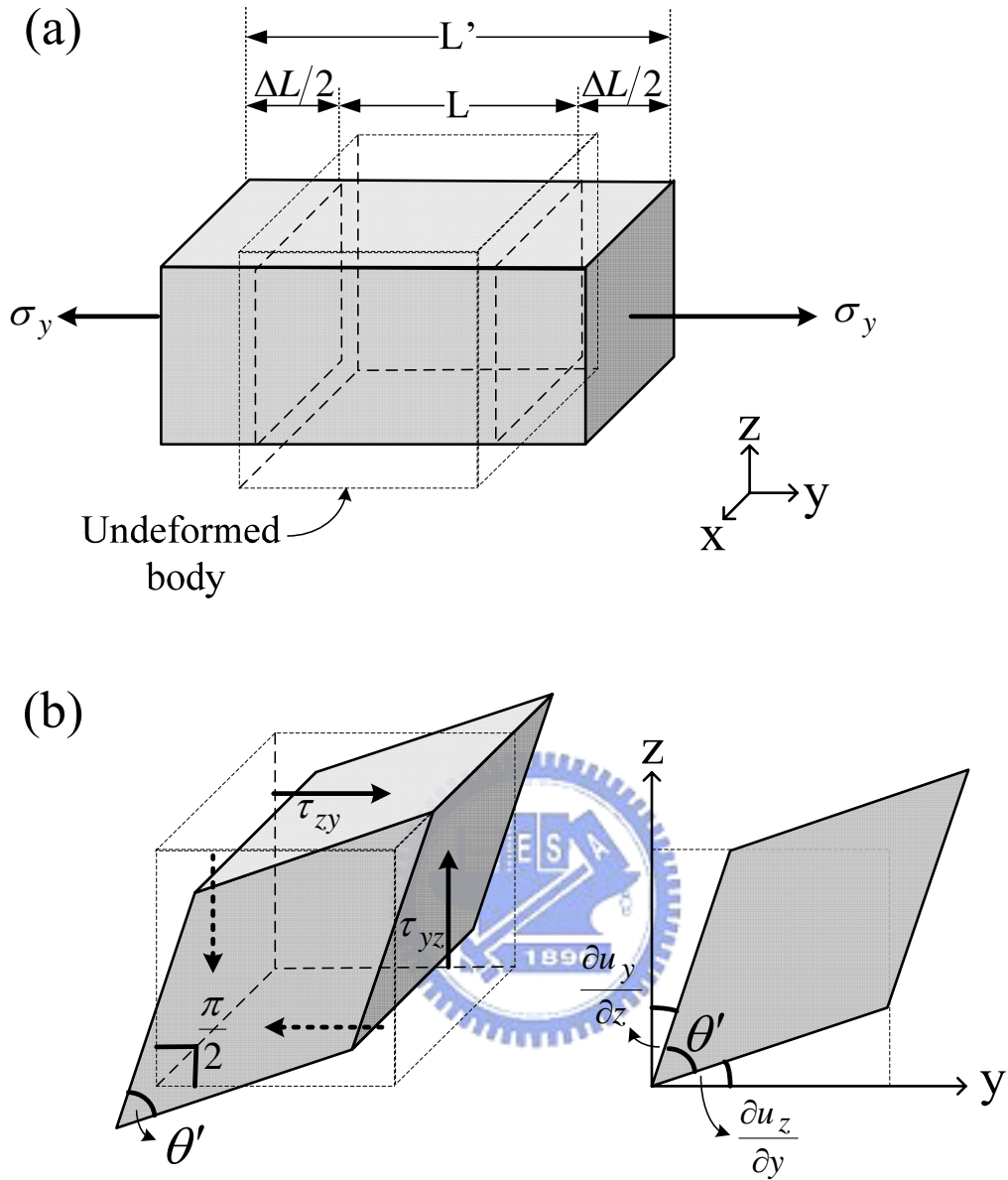


Fig. 2.2. (a) Schematic of the deformation of a body applied to normal stress along y -axis; and (b) schematic the deformation of a body applied to pure shear stress. Dash line indicates the size and shape of the original body before deformation and solid line indicates those of the body after deformation

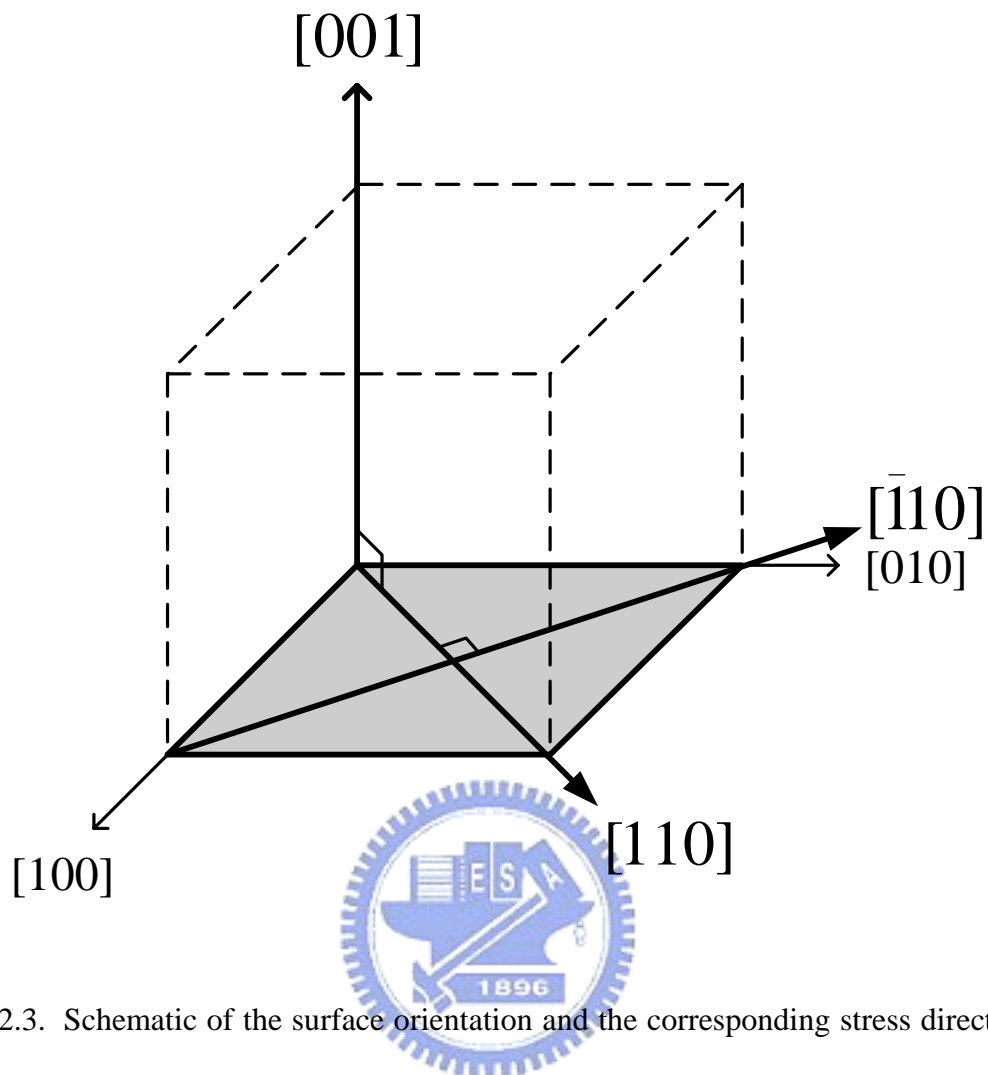


Fig. 2.3. Schematic of the surface orientation and the corresponding stress directions for (001) wafer. The shadow region indicates the wafer surface. The surface normal is $[001]$, the longitudinal (channel) direction is $[110]$, and the transverse direction, which is perpendicular to the channel in the plane, is $[\bar{1}10]$.

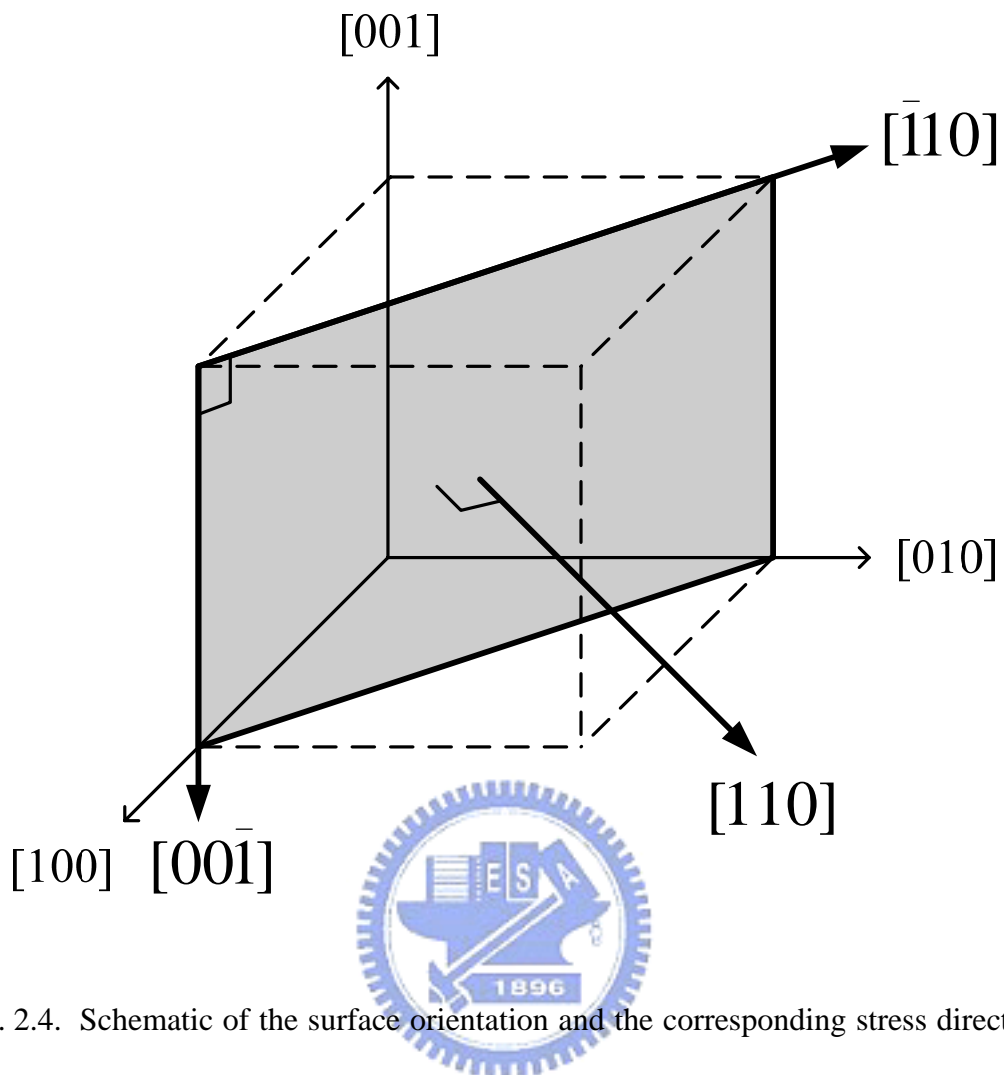


Fig. 2.4. Schematic of the surface orientation and the corresponding stress directions for (110) wafer. The shadow region indicates the wafer surface. The surface normal is $[110]$, the longitudinal (channel) direction is $[\bar{1}10]$, and the transverse direction, which is perpendicular to the channel in the plane, is $[00\bar{1}]$.

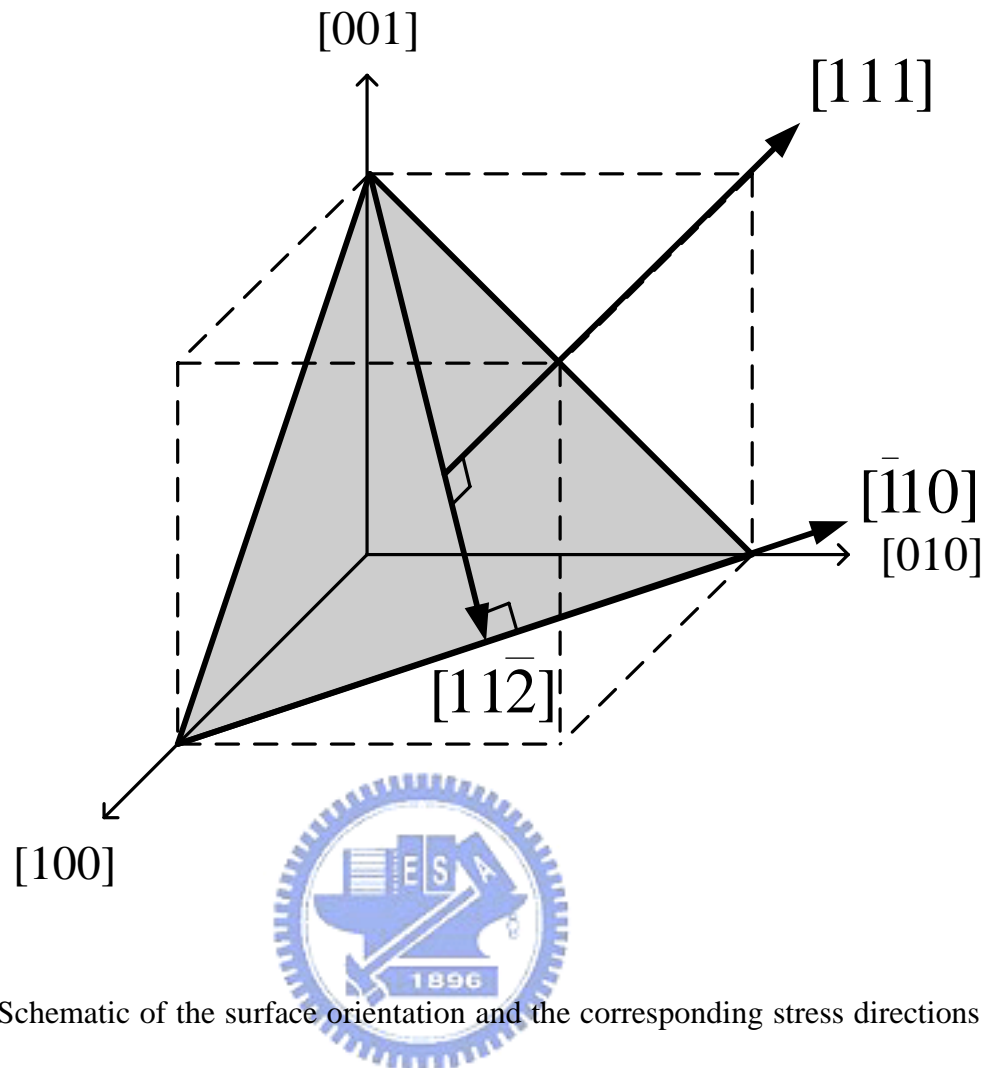


Fig. 2.5. Schematic of the surface orientation and the corresponding stress directions for (111) wafer. The shadow region indicates the wafer surface. The surface normal is [111], the longitudinal (channel) direction is $[\bar{1}10]$, and the transverse direction, which is perpendicular to the channel in the plane, is $[11\bar{2}]$.

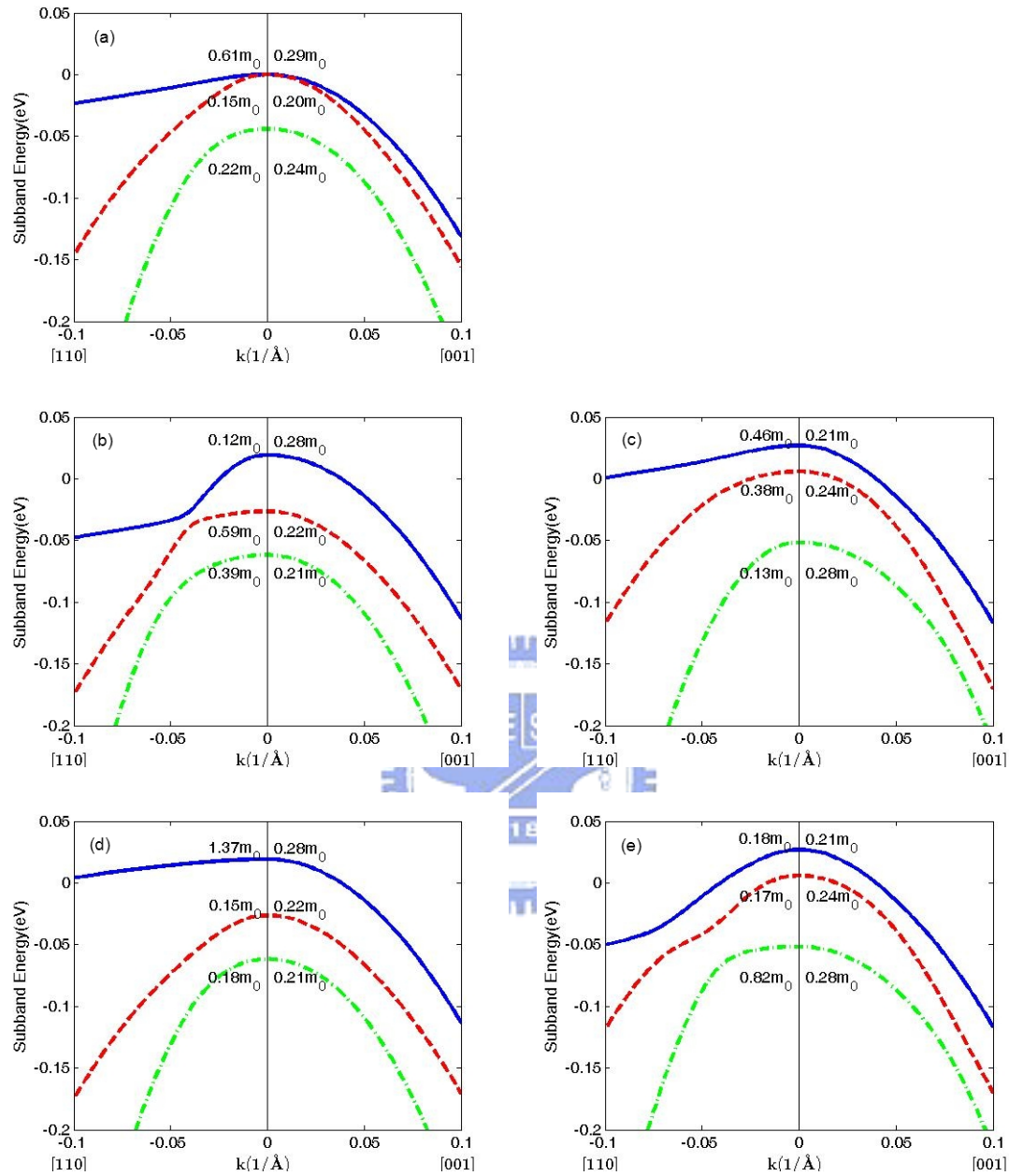


Fig. 2.6. Silicon valence band structures for (a) unstressed, (b) 1GPa uniaxial longitudinal compressive, (c) 1GPa uniaxial longitudinal tensile, (d) 1GPa uniaxial transverse compressive, and (e) 1GPa uniaxial transverse tensile stress on (001) wafer.

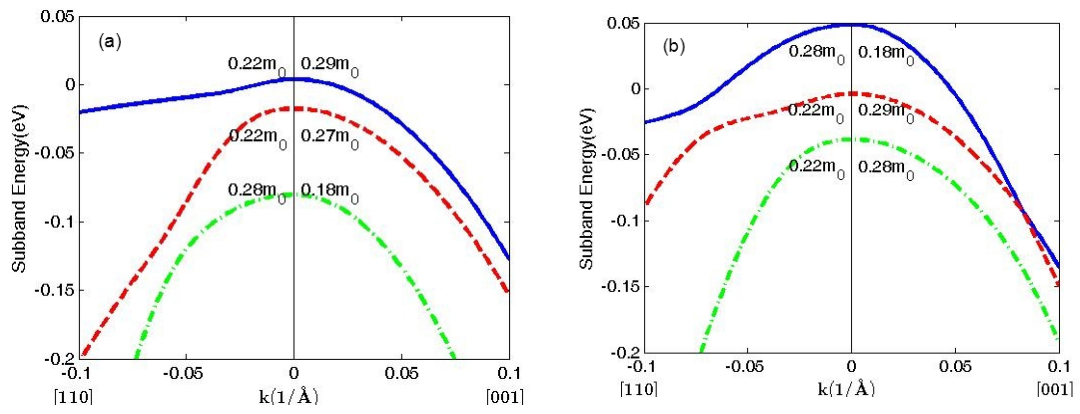


Fig. 2.7. Silicon valence band structures for (a) 1GPa biaxial compressive and (b) 1GPa biaxial tensile stress on (001) wafer.



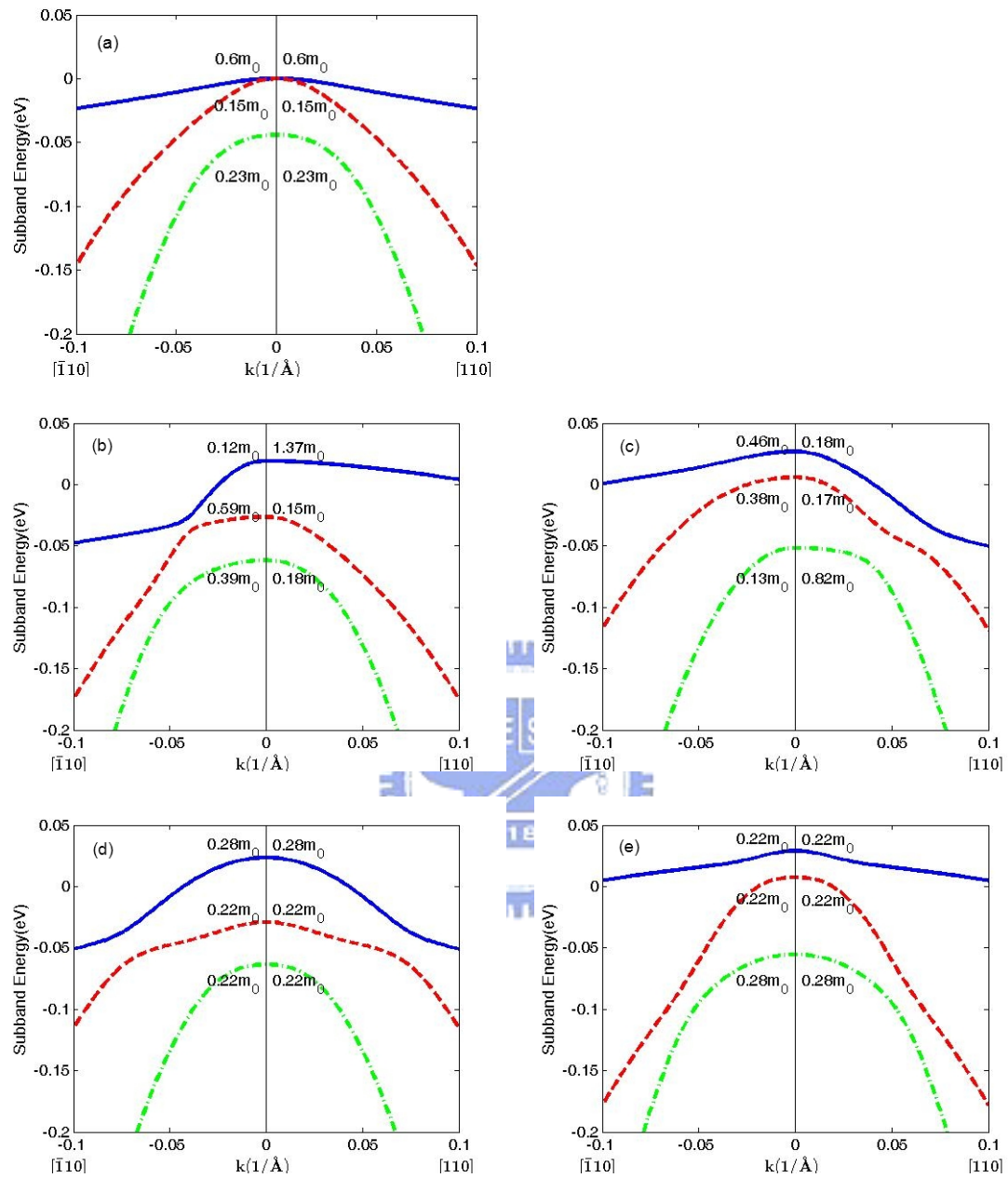


Fig. 2.8. Silicon valence band structures for (a) unstressed, (b) 1GPa uniaxial longitudinal compressive, (c) 1GPa uniaxial longitudinal tensile, (d) 1GPa uniaxial transverse compressive, and (e) 1GPa uniaxial transverse tensile stress on (110) wafer.

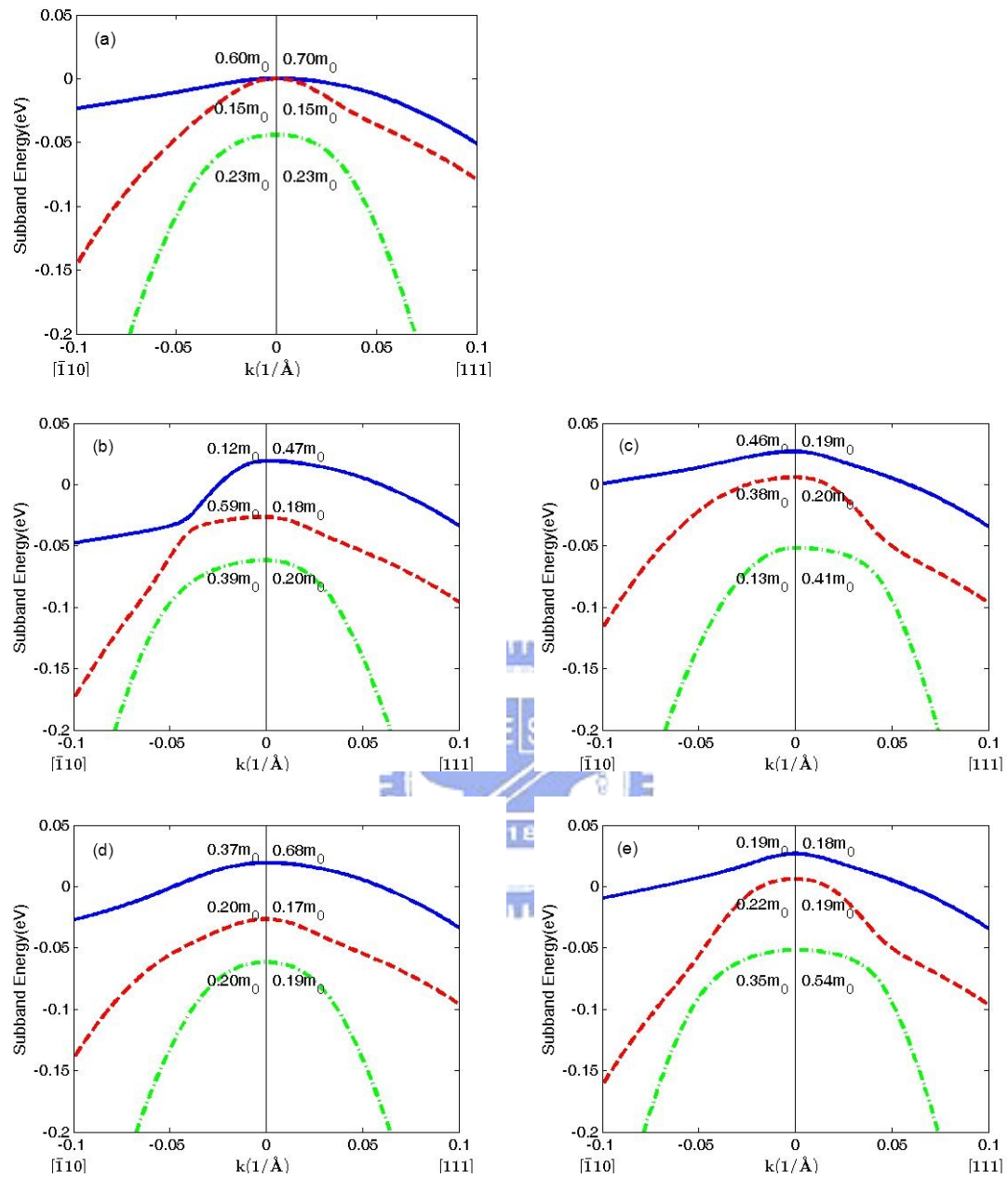


Fig. 2.9. Silicon valence band structures for (a) unstressed, (b) 1GPa uniaxial longitudinal compressive, (c) 1GPa uniaxial longitudinal tensile, (d) 1GPa uniaxial transverse compressive, and (e) 1GPa uniaxial transverse tensile stress on (111) wafer.

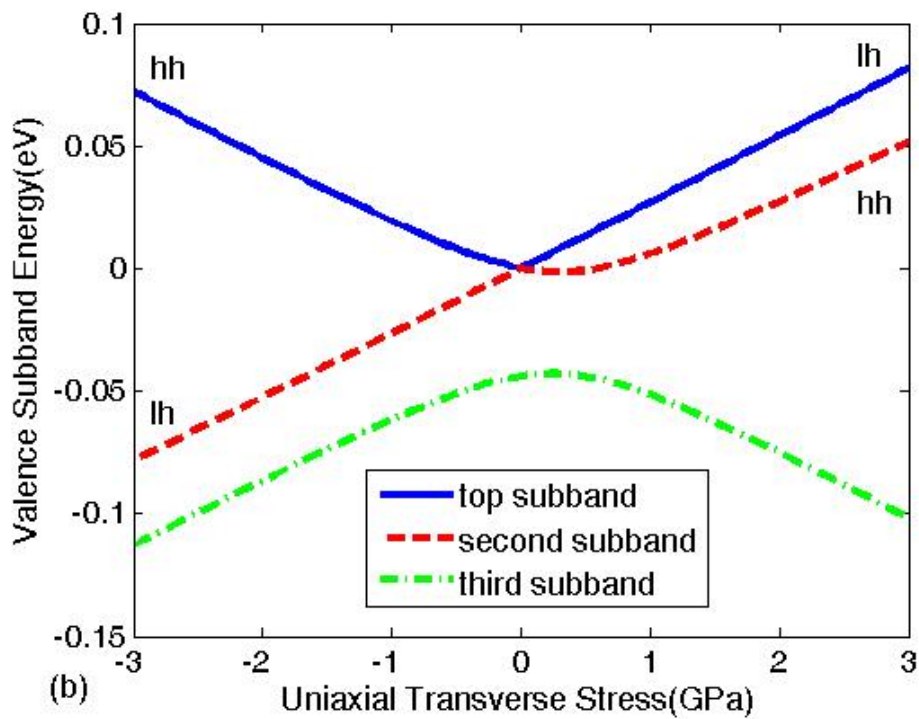
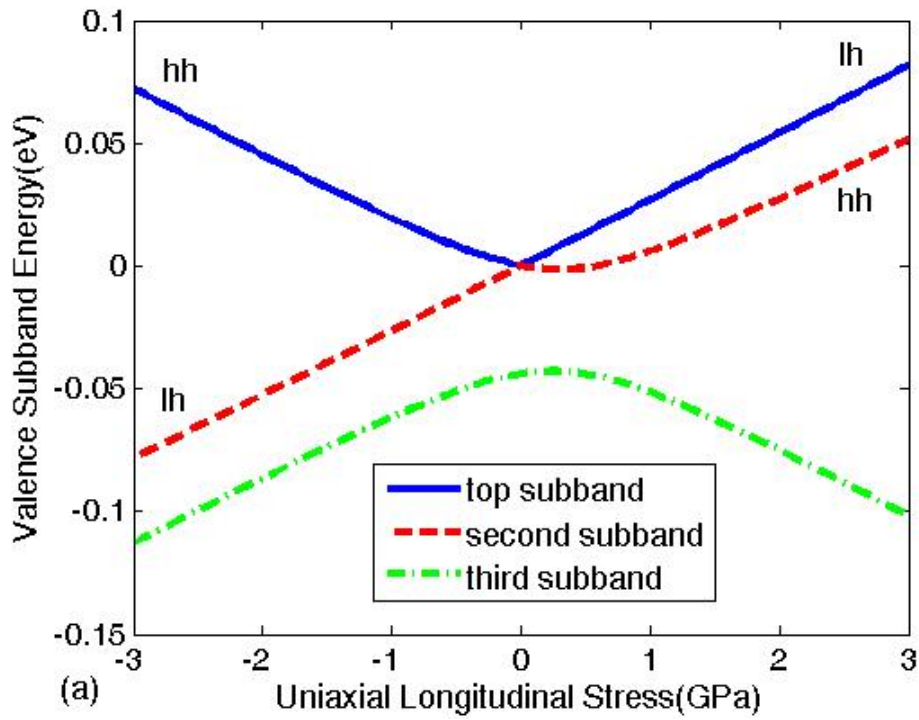


Fig. 2.10. Strain-induced hole subband energy shift versus (a) uniaxial longitudinal and (b) uniaxial transverse stress on (001) wafer.

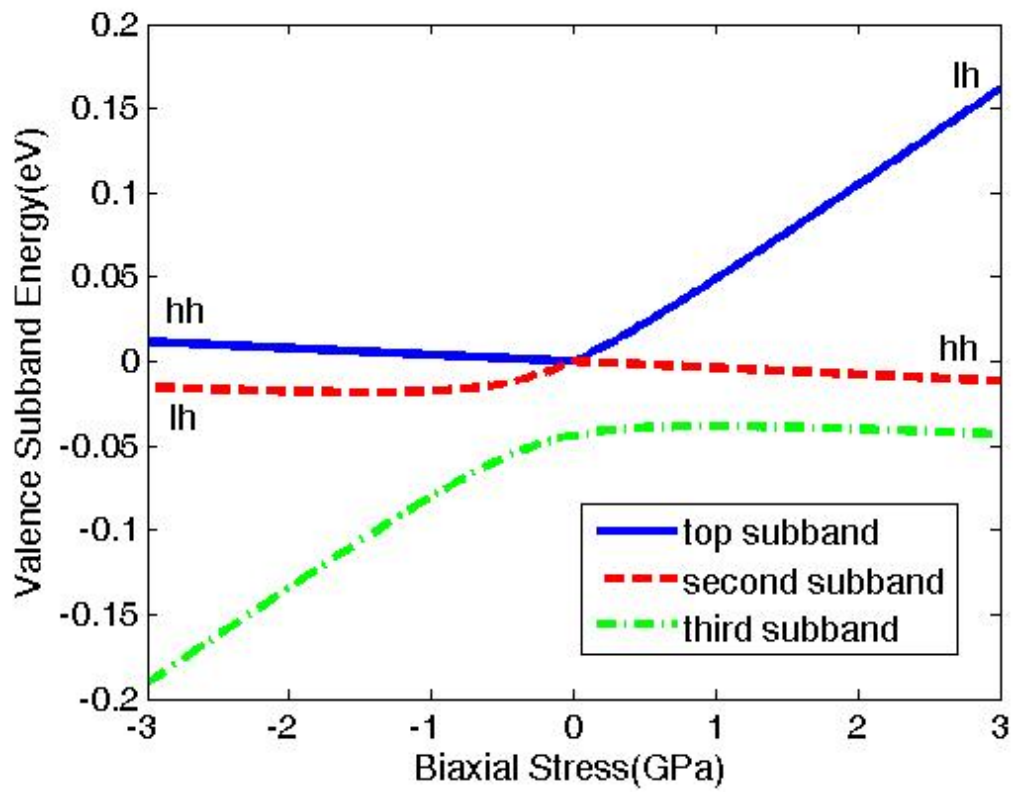


Fig. 2.11. Strain-induced hole subband energy shift versus biaxial stress on (001) wafer.

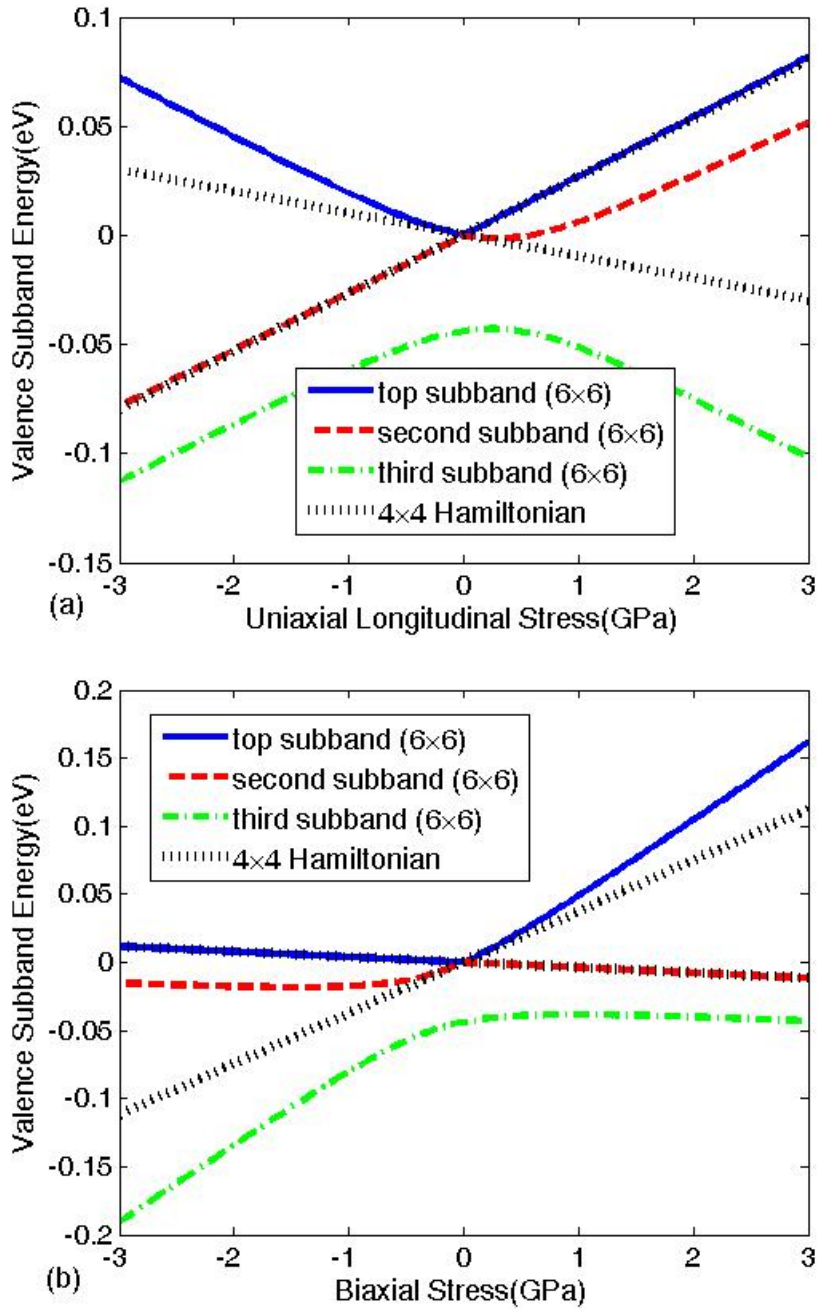


Fig. 2.12. Comparison between the strain-induced hole subband energy shift calculated by 4×4 and 6×6 Hamiltonian for (a) uniaxial longitudinal and (b) biaxial stress on (001) wafer. The solid line indicates the subband energy calculated by the 6×6 Hamiltonian. The dotted line indicates the subband energy calculated by 4 by 4 Hamiltonian.

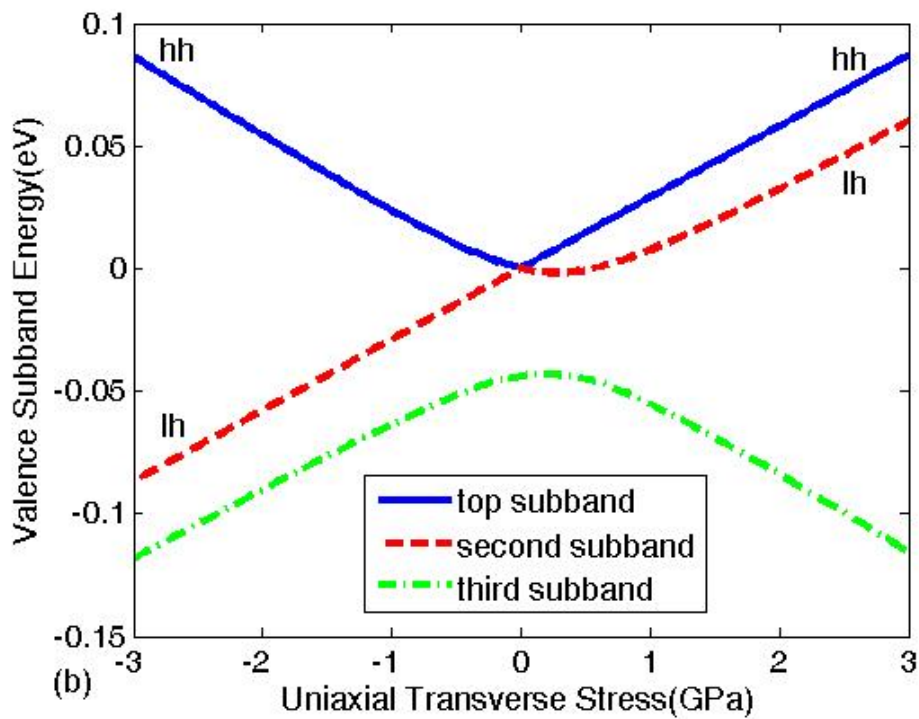
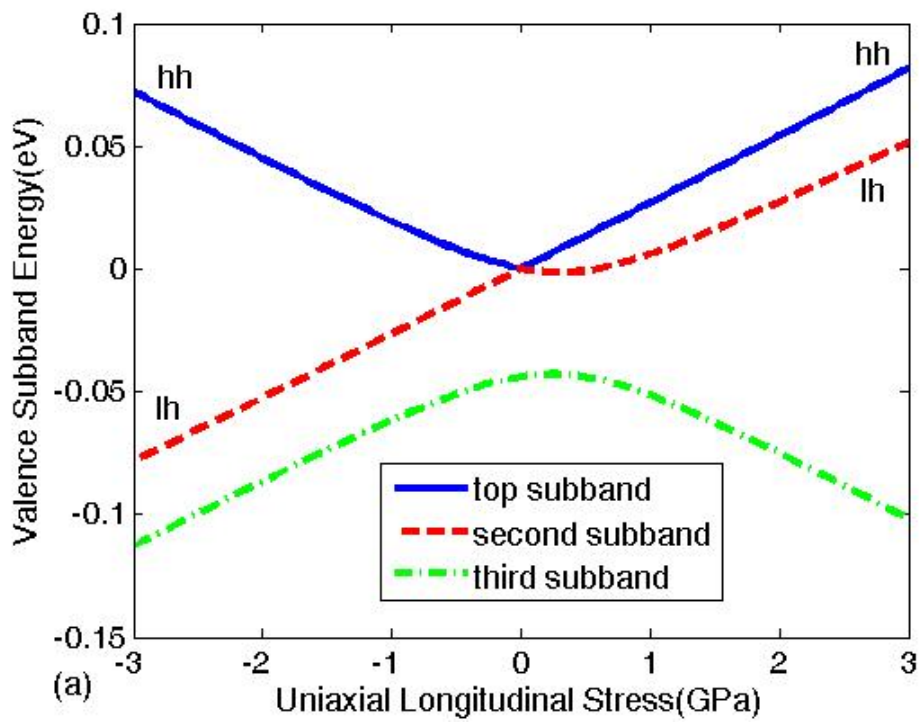


Fig. 2.13. Strain-induced hole subband energy shift versus (a) uniaxial longitudinal and (b) uniaxial transverse stress on (110) wafer.

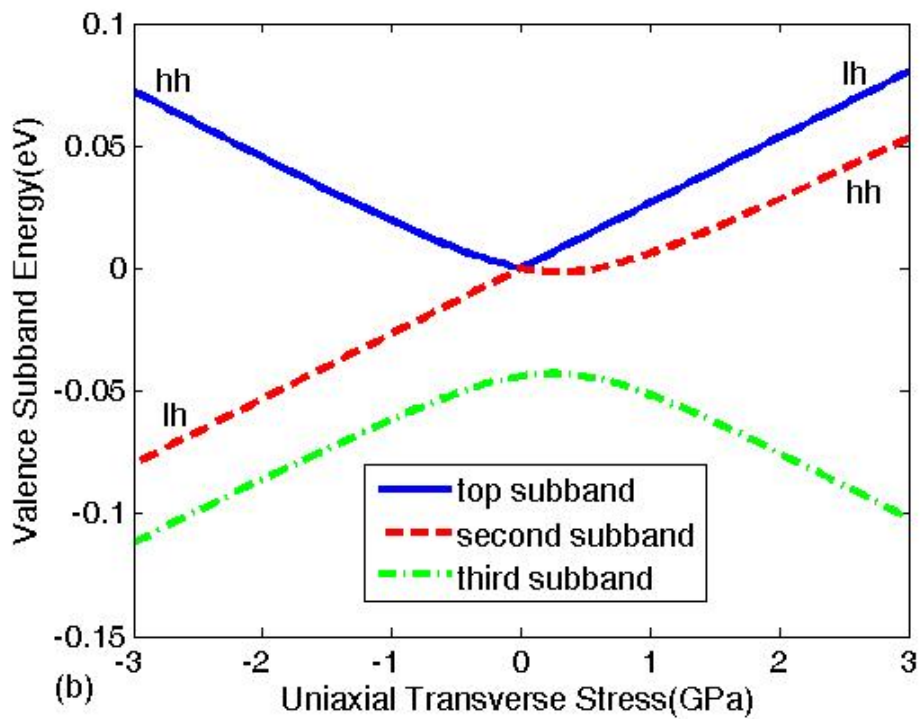
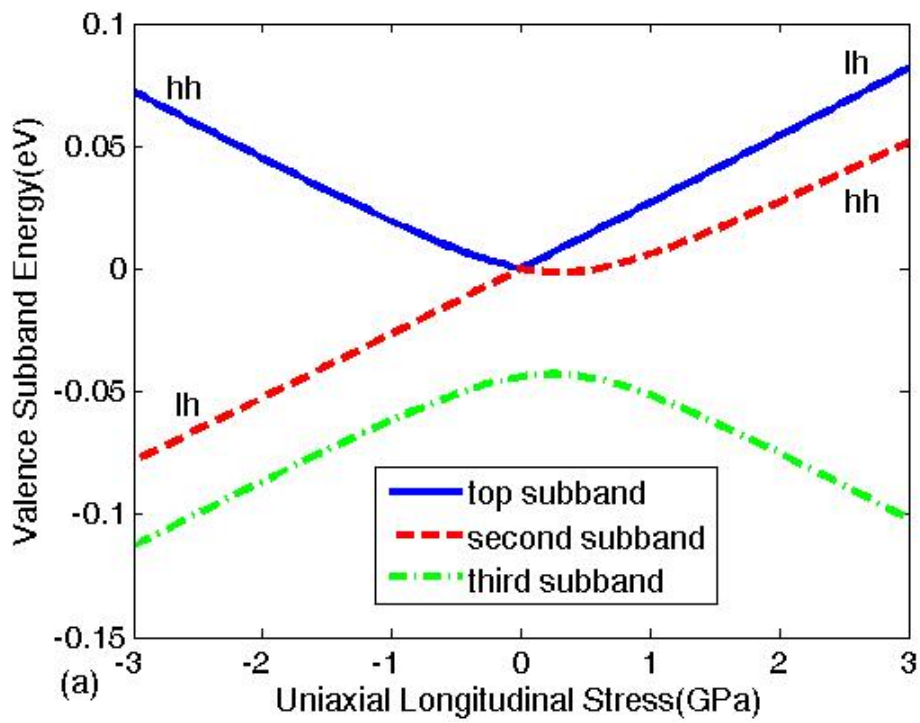
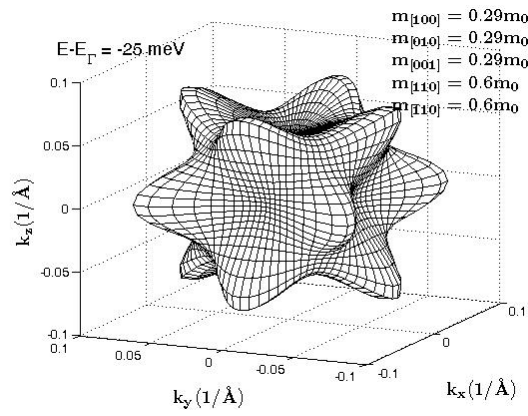
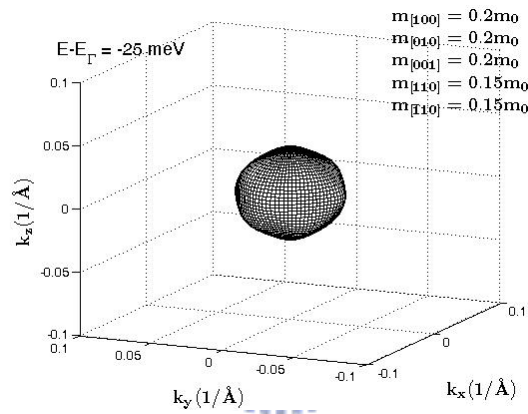


Fig. 2.14. Strain-induced subband energy shift versus (a) uniaxial longitudinal and (b) uniaxial transverse stress on (111) wafer.

Top band



Second band



Third band

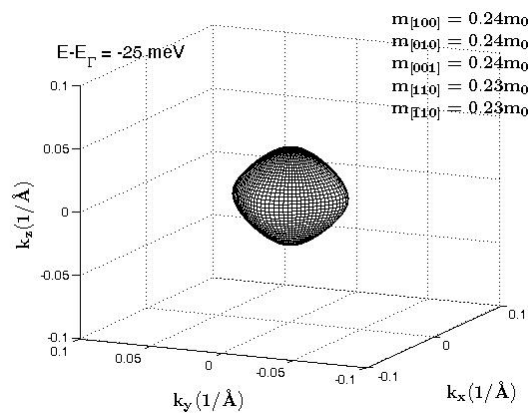
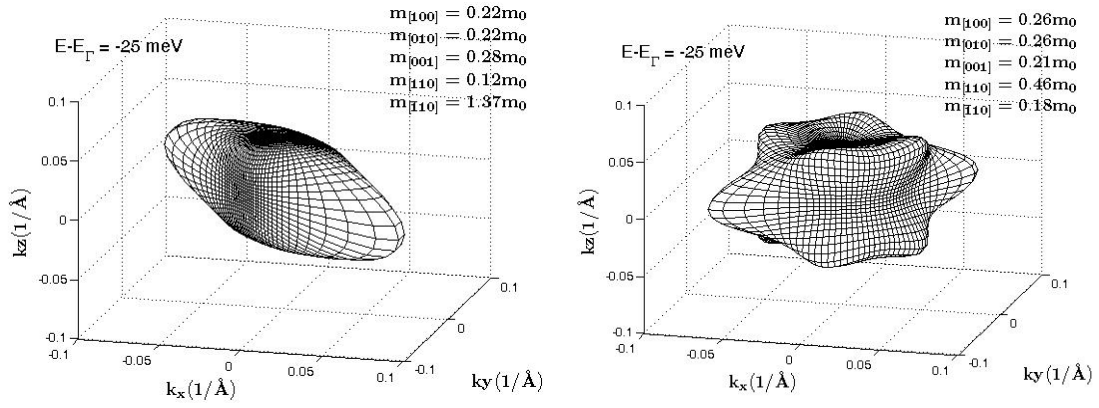
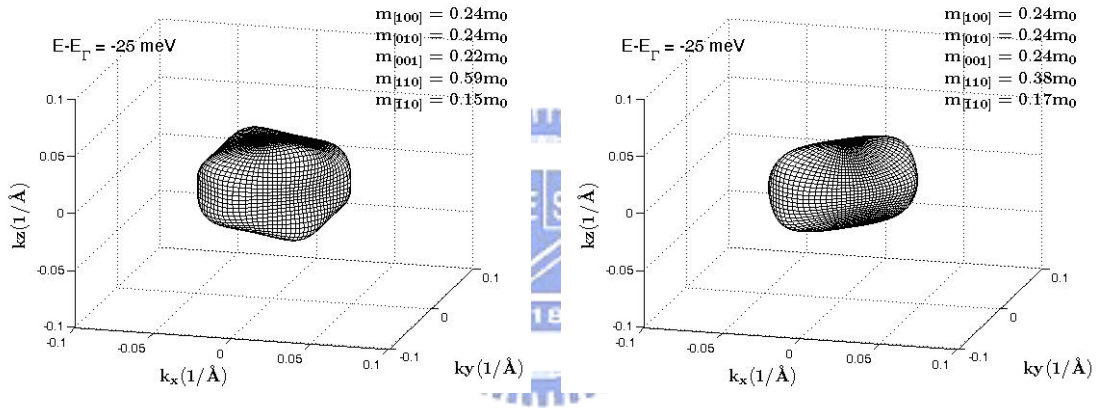


Fig. 2.15. Hole constant energy surface of unstressed bulk silicon for three lowest bands.

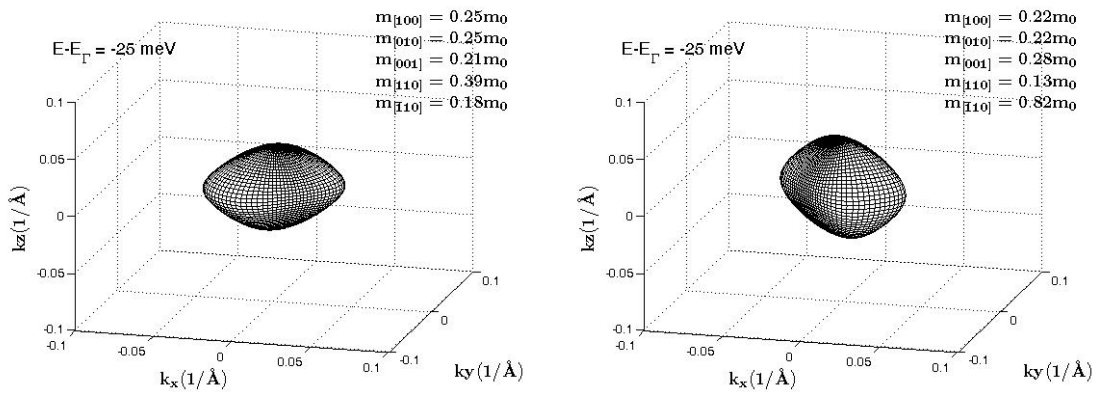
Top band



Second band



Third band

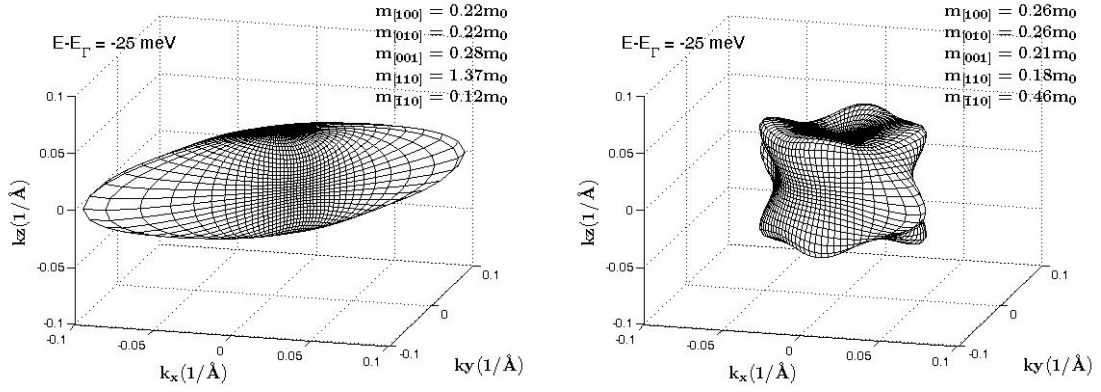


(a)

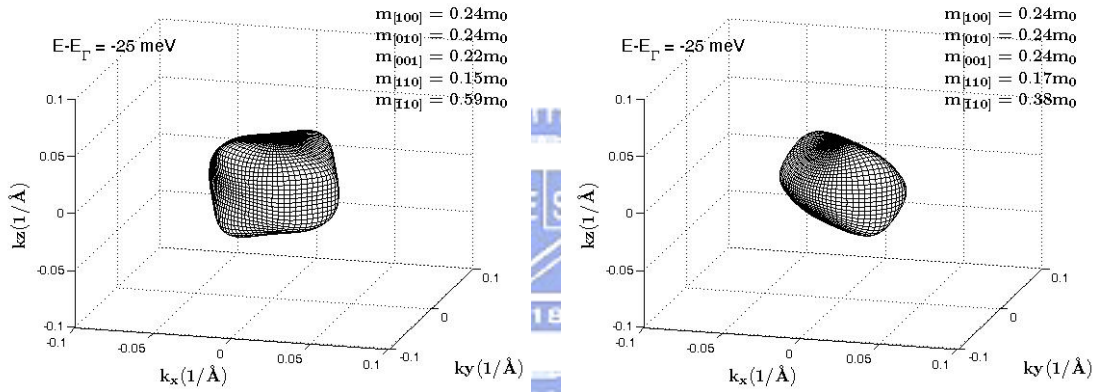
(b)

Fig. 2.16. Hole constant energy surface of silicon under 1GPa uniaxial longitudinal (a) compressive and (b) tensile stress on (001) wafer for three lowest bands.

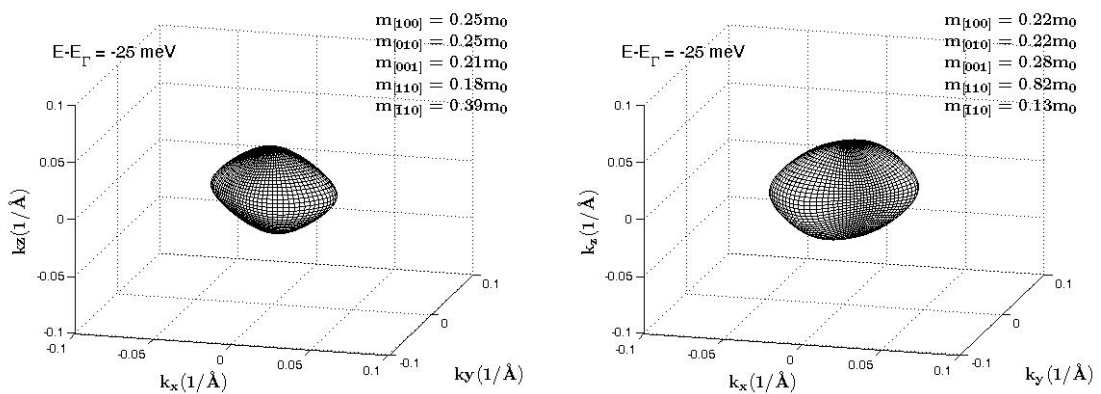
Top band



Second band



Third band

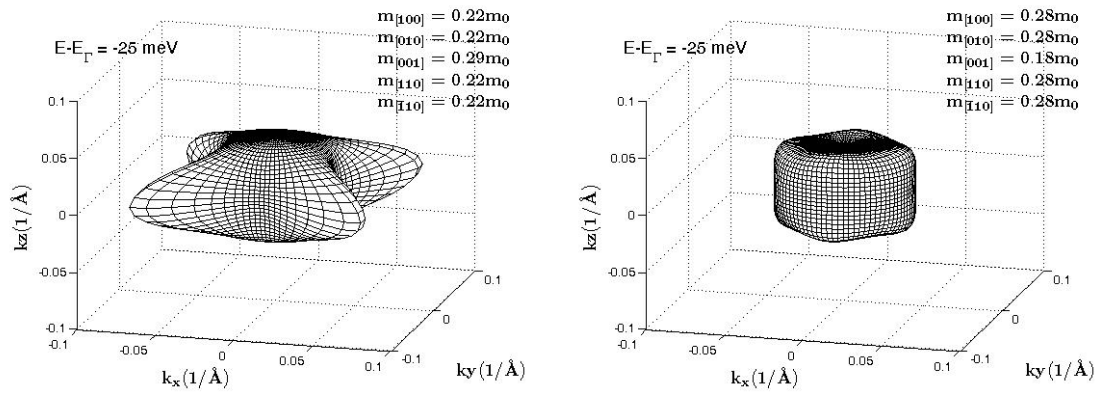


(a)

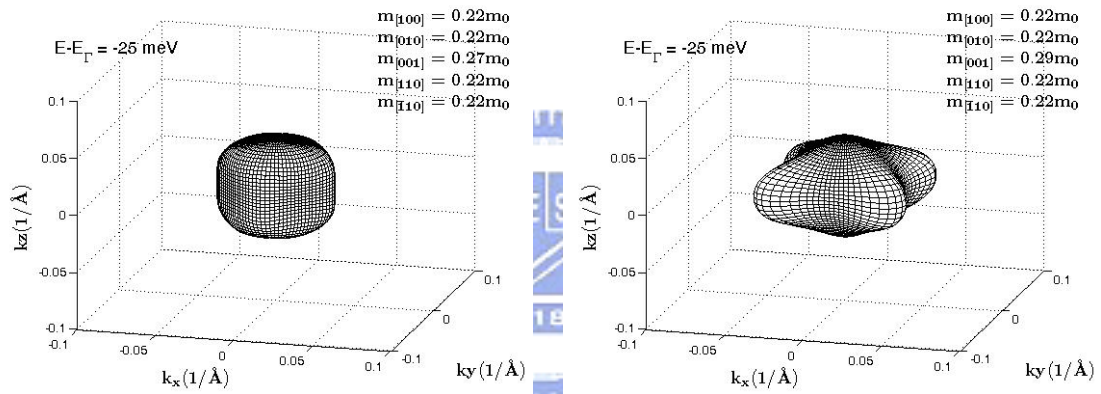
(b)

Fig. 2.17. Hole constant energy surface of silicon under 1GPa uniaxial transverse (a) compressive and (b) tensile stress on (001) wafer for three lowest bands.

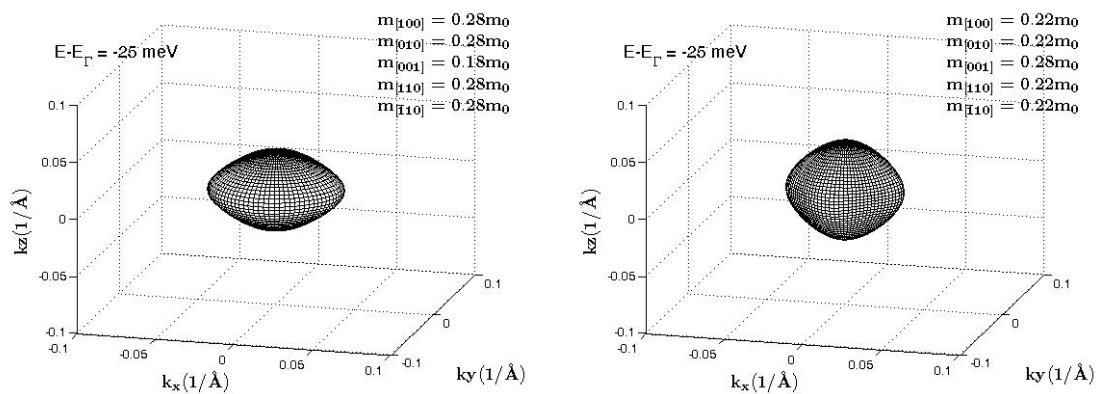
Top band



Second band



Third band

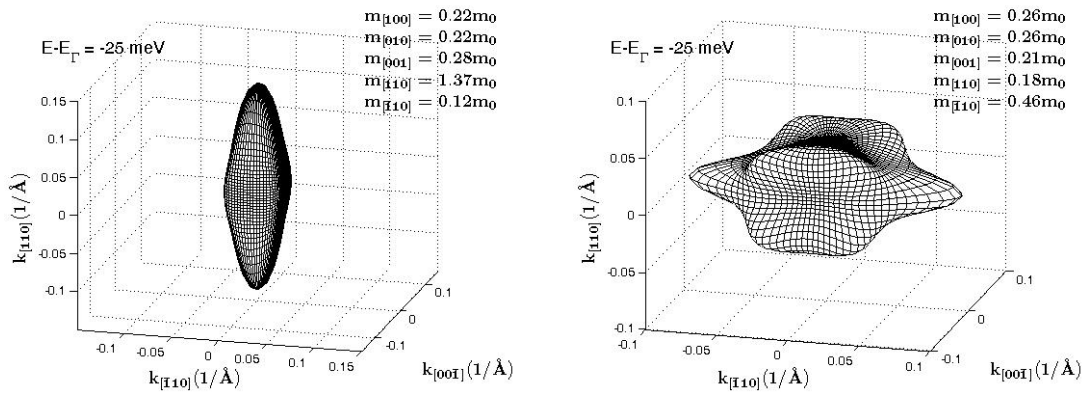


(a)

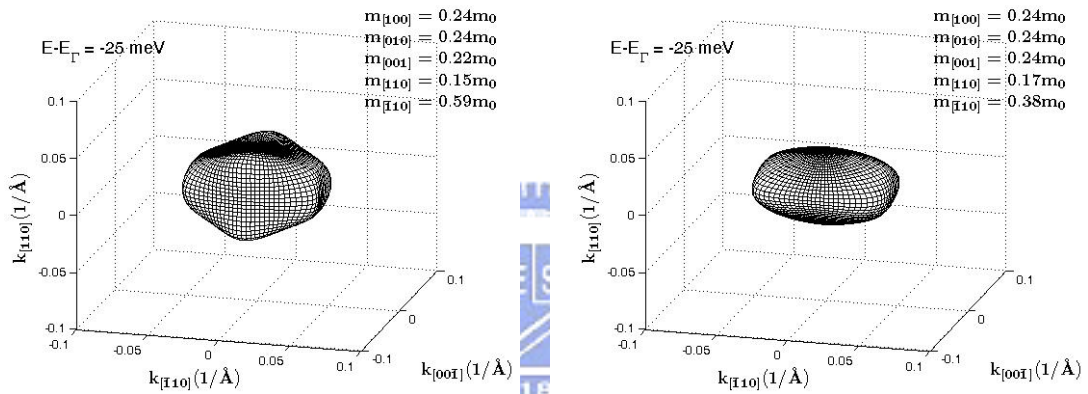
(b)

Fig. 2.18. Hole constant energy surface of Silicon under 1GPa biaxial (a) compressive and (b) tensile stress on (001) wafer for three lowest bands.

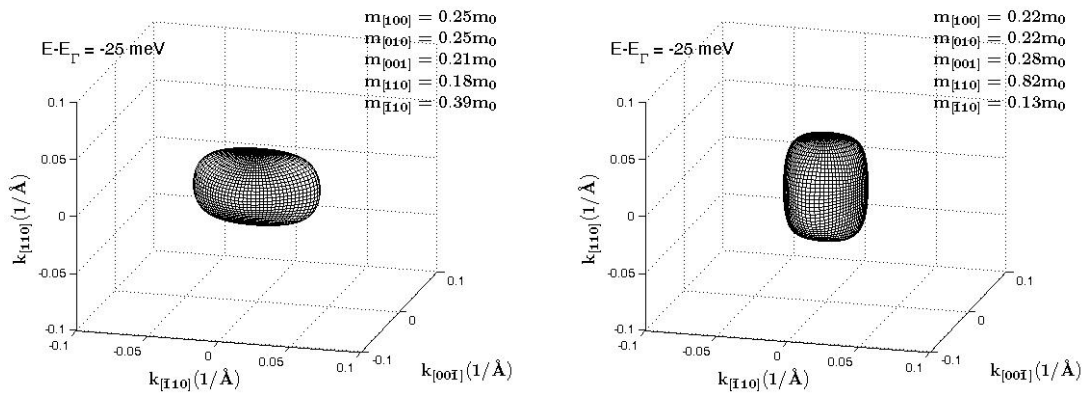
Top band



Second band



Third band

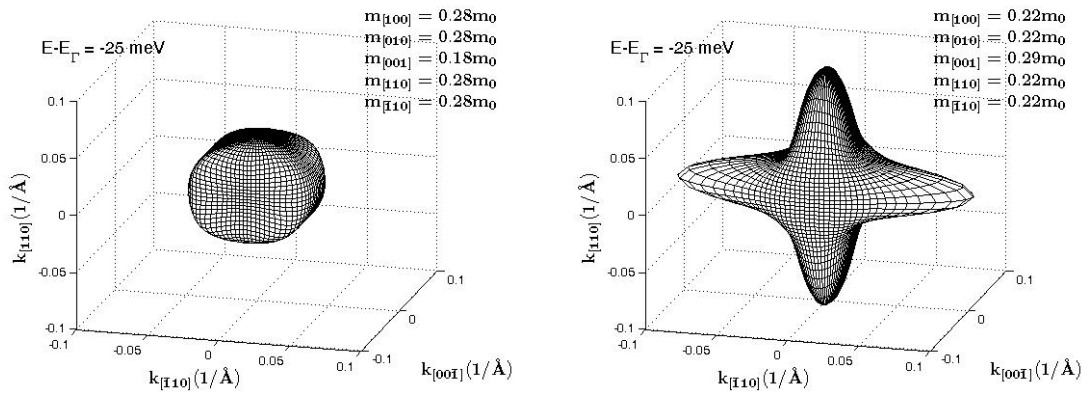


(a)

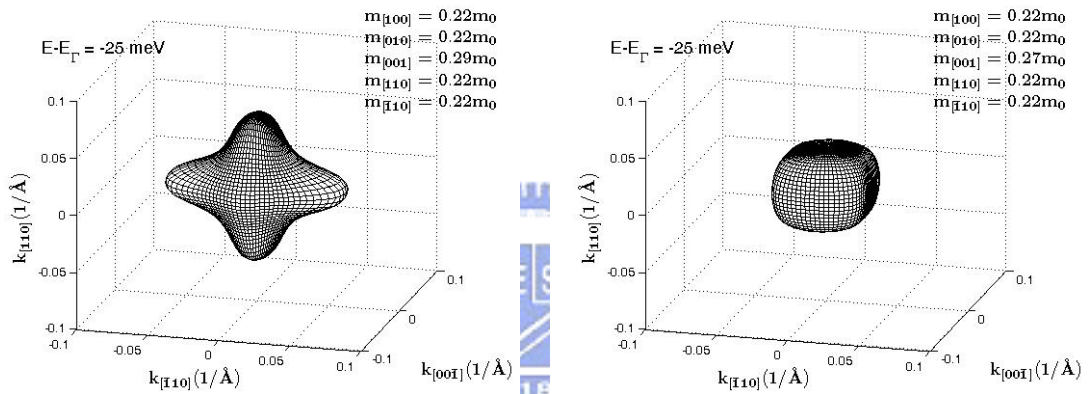
(b)

Fig. 2.19. Hole constant energy surface of silicon under 1GPa uniaxial longitudinal (a) compressive and (b) tensile stress on (110) wafer for three lowest bands.

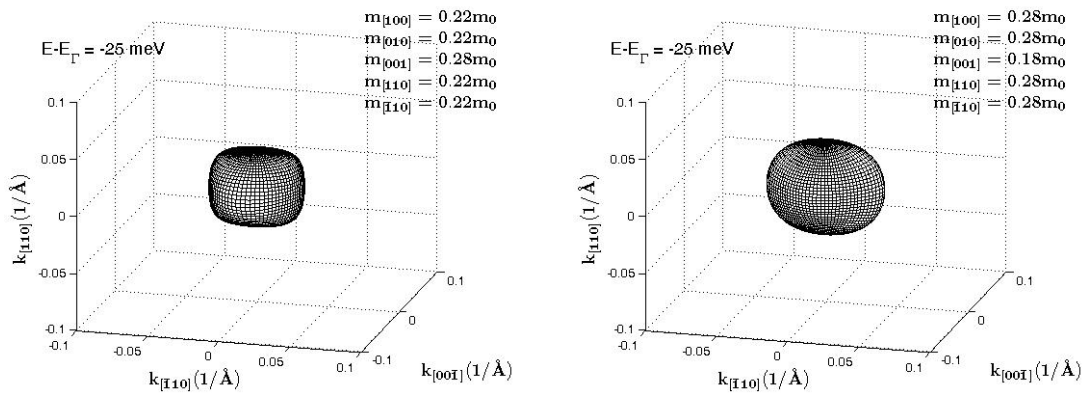
Top band



Second band



Third band

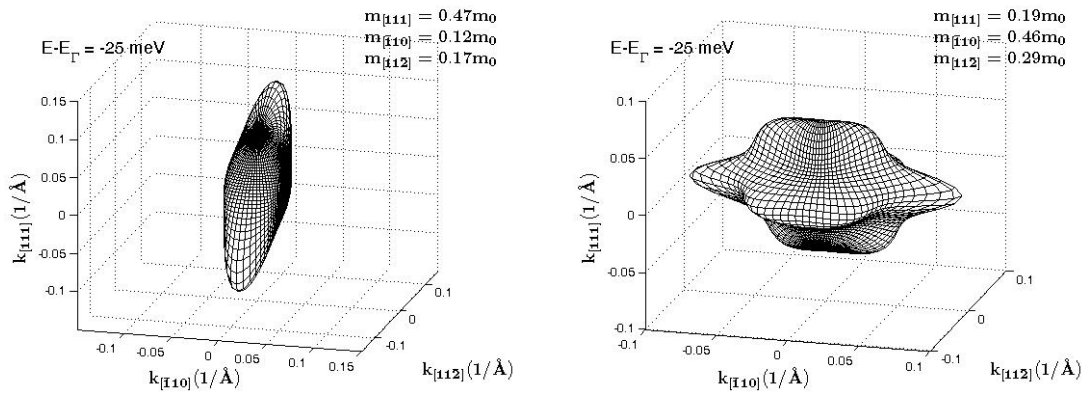


(a)

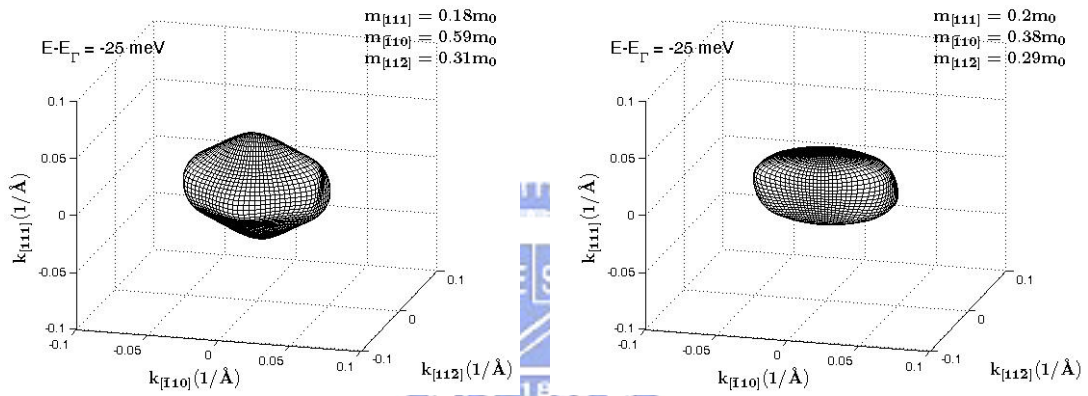
(b)

Fig. 2.20. Hole constant energy surface of silicon under 1GPa uniaxial transverse (a) compressive and (b) tensile stress on (110) wafer for three lowest bands.

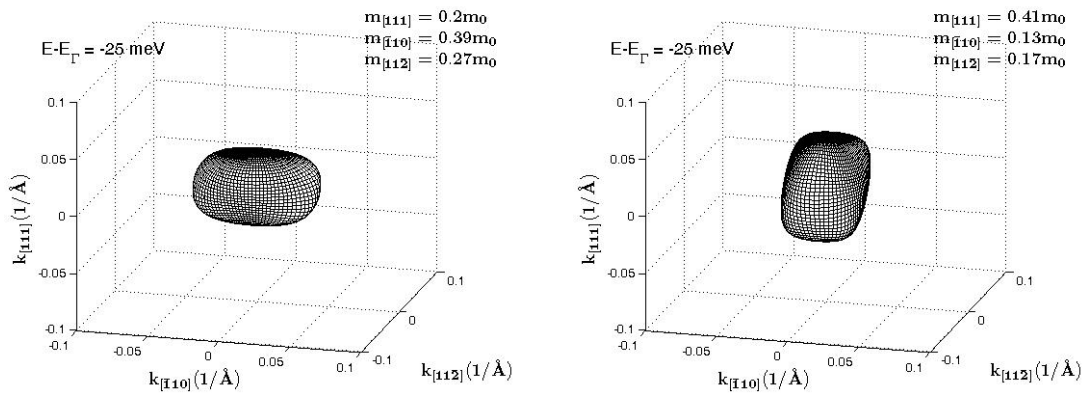
Top band



Second band



Third band

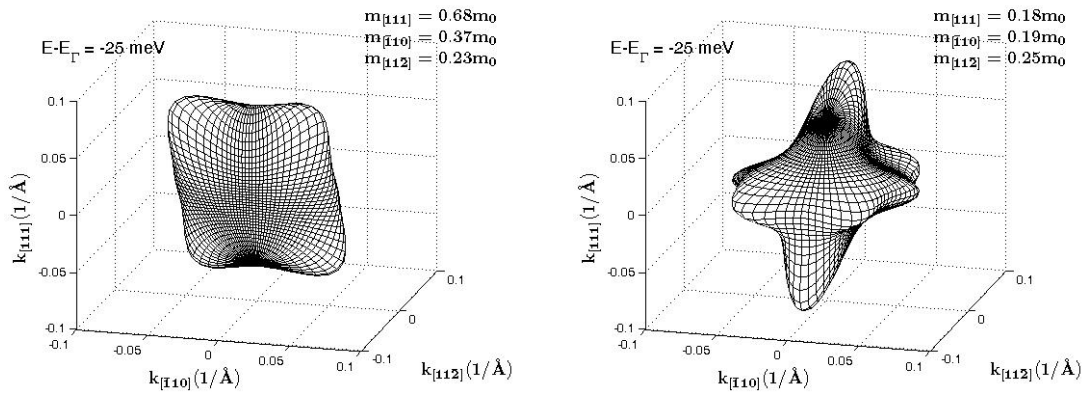


(a)

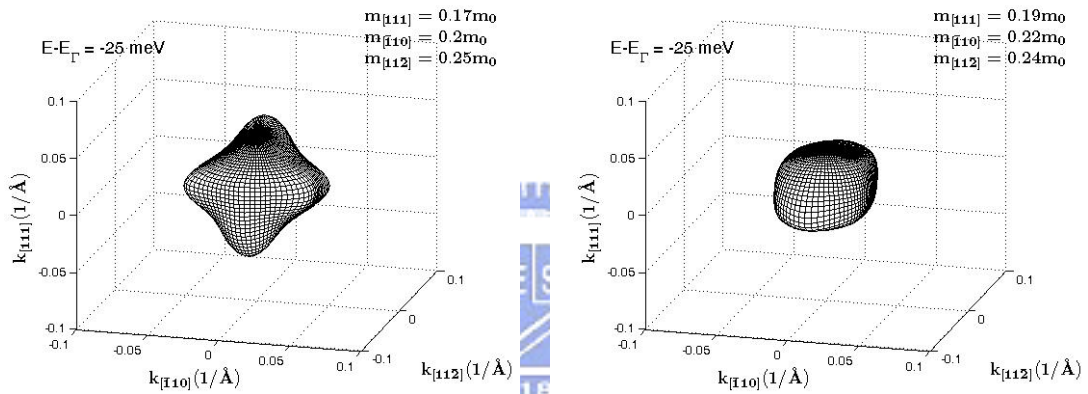
(b)

Fig. 2.21. Hole constant energy surface of silicon under 1GPa uniaxial longitudinal (a) compressive and (b) tensile stress on (111) wafer for three lowest bands.

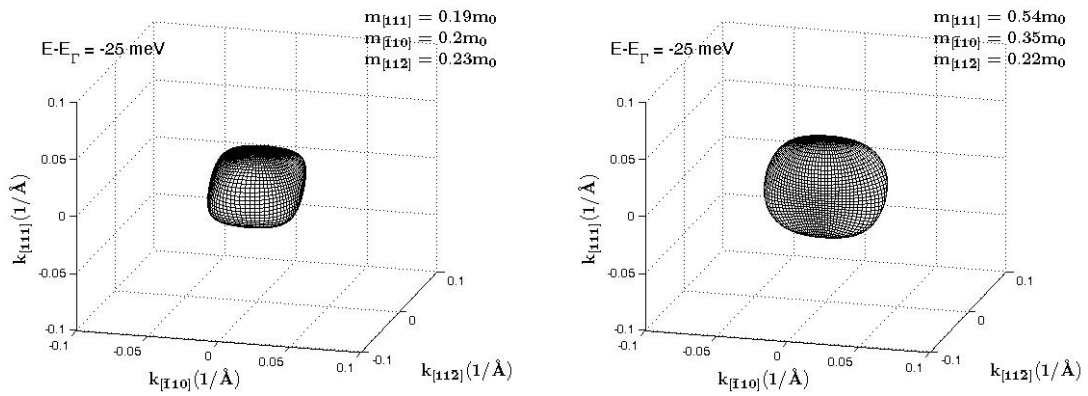
Top band



Second band



Third band

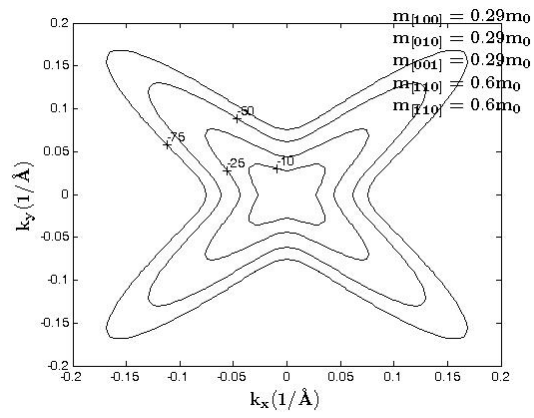


(a)

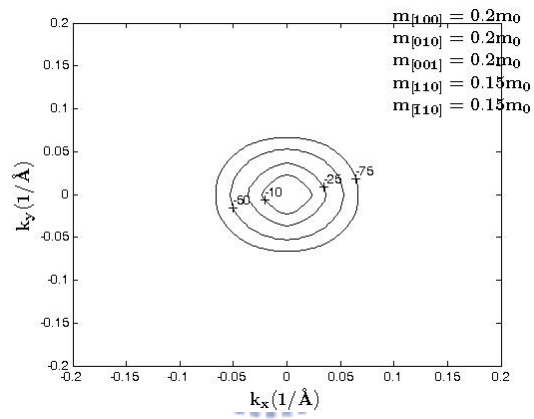
(b)

Fig. 2.22. Hole constant energy surface of silicon under 1GPa uniaxial longitudinal (a) compressive and (b) tensile stress on (111) wafer for three lowest bands.

Top band



Second band



Third band

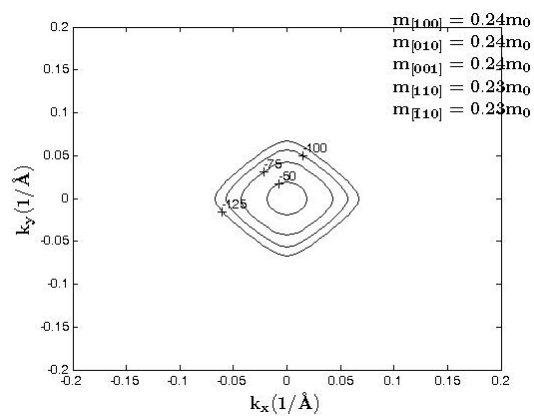
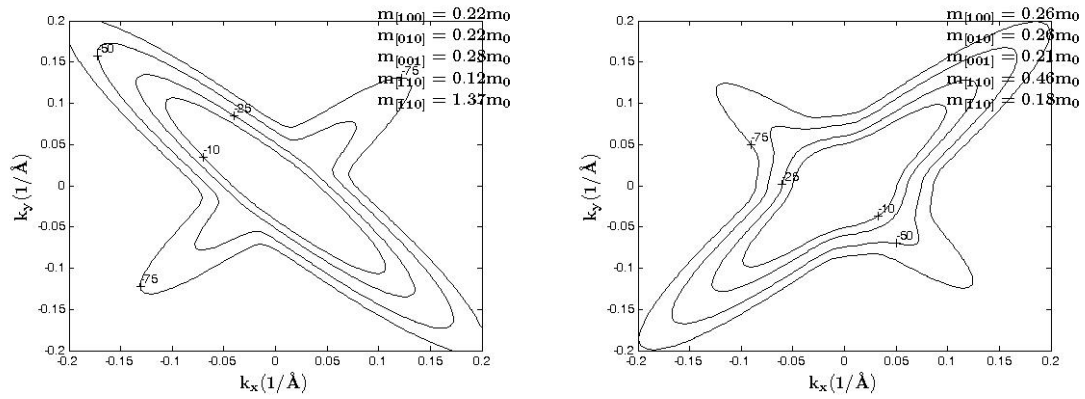
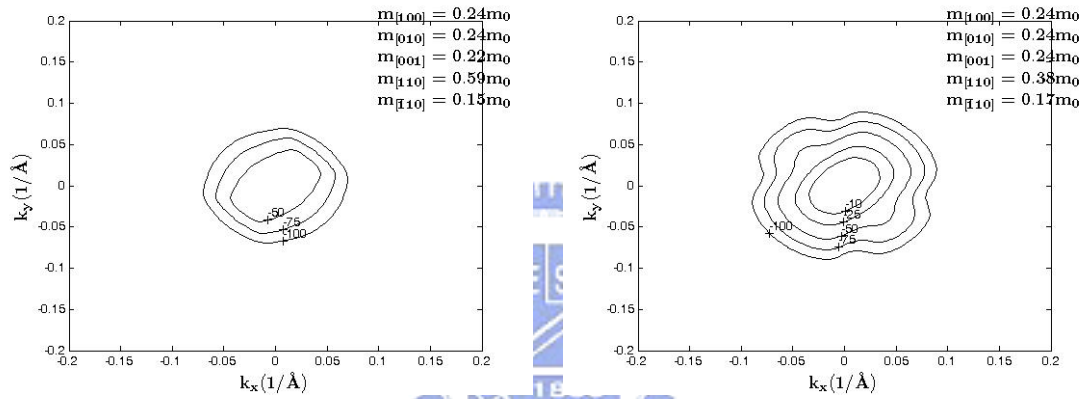


Fig. 2.23. Contour map in k_x , k_y plane ($k_z=0$) of unstressed bulk silicon on (001) wafer for three lowest valence bands.

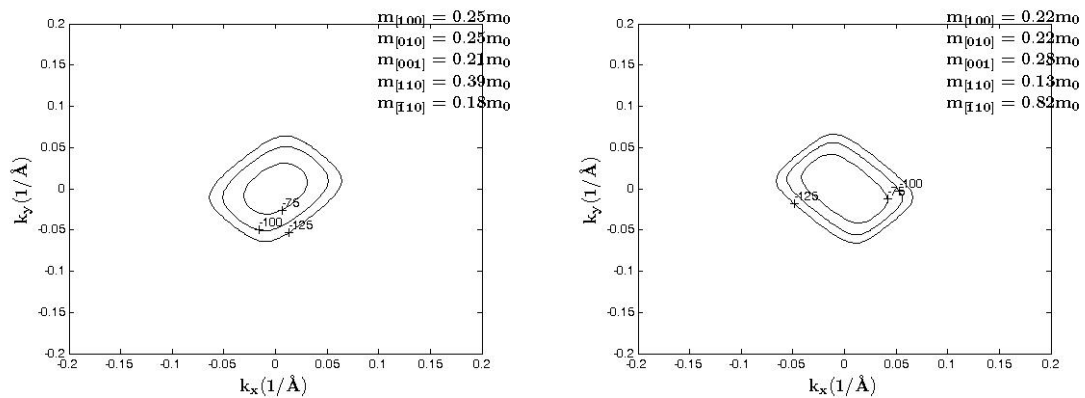
Top band



Second band



Third band

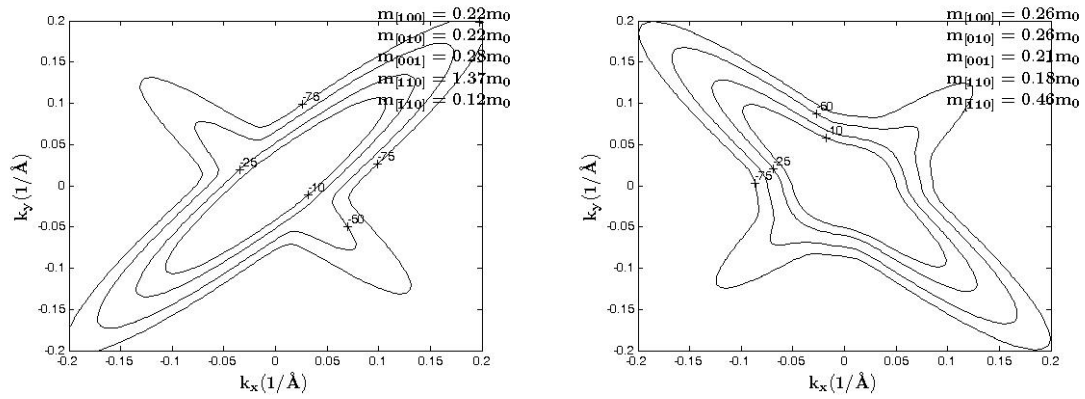


(a)

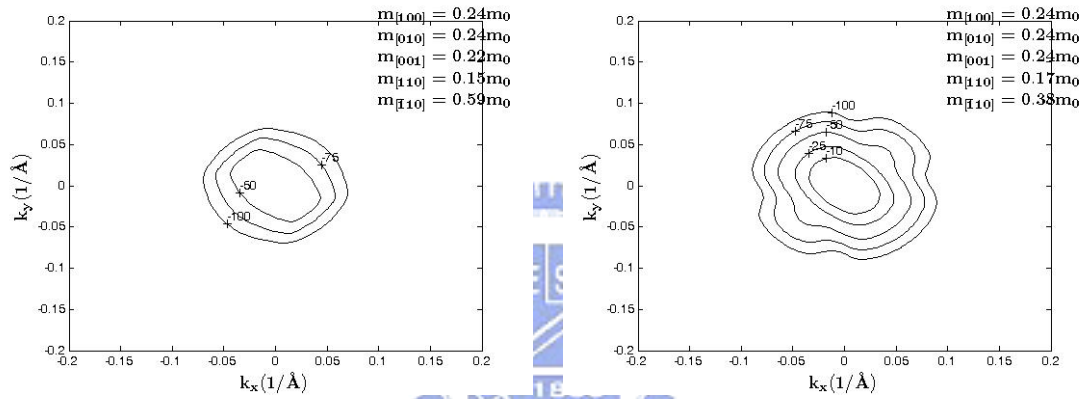
(b)

Fig. 2.24. Contour map in k_x, k_y plane ($k_z=0$) of silicon under 1GPa uniaxial longitudinal (a) compressive and (b) tensile stress on (001) wafer for three lowest valence bands.

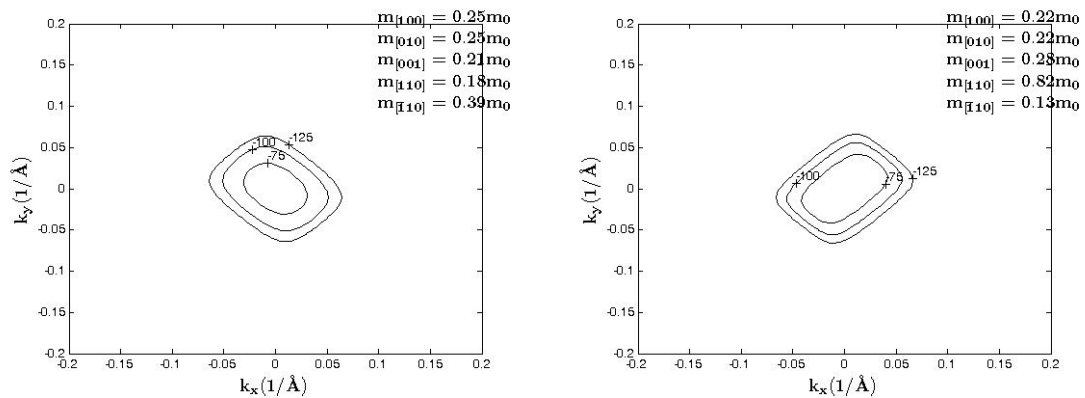
Top band



Second band



Third band

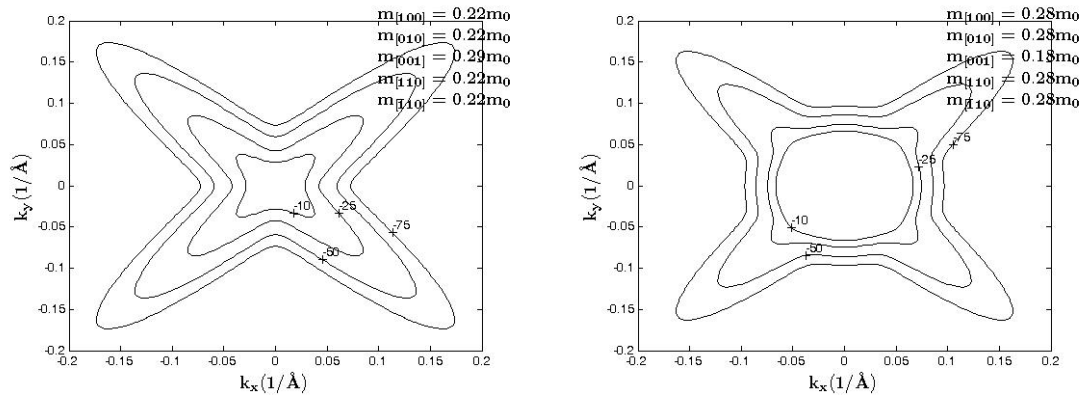


(a)

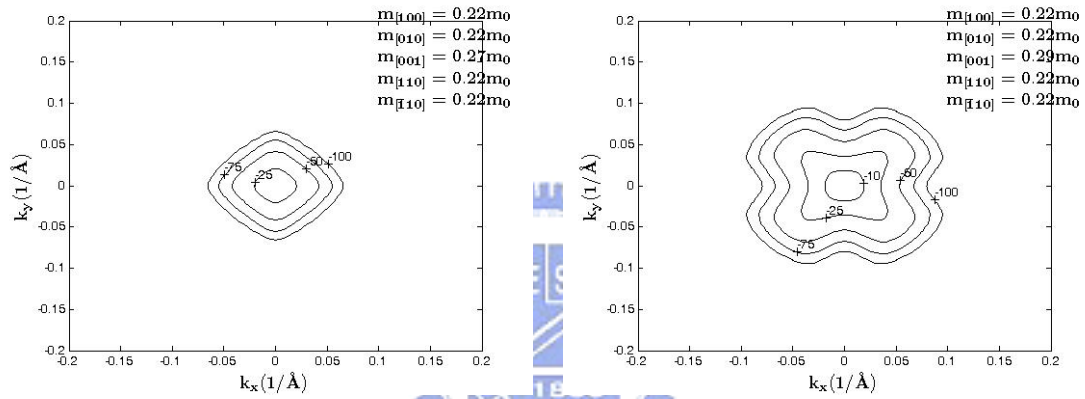
(b)

Fig. 2.25. Contour map in k_x, k_y plane ($k_z=0$) of silicon under 1GPa uniaxial transverse (a) compressive and (b) tensile stress on (001) wafer for three lowest valence bands.

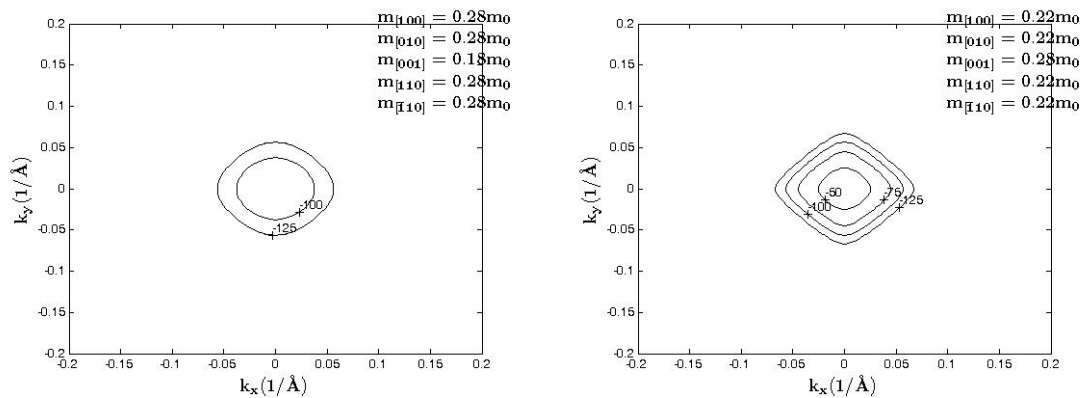
Top band



Second band



Third band

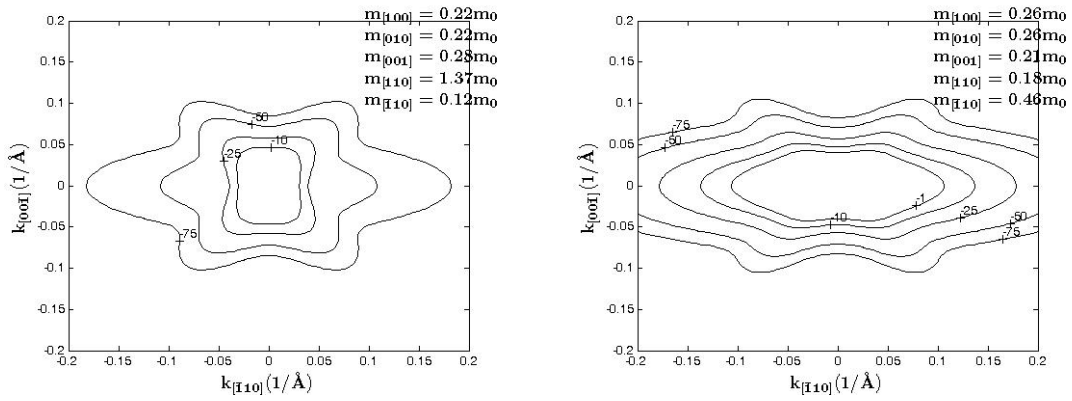


(a)

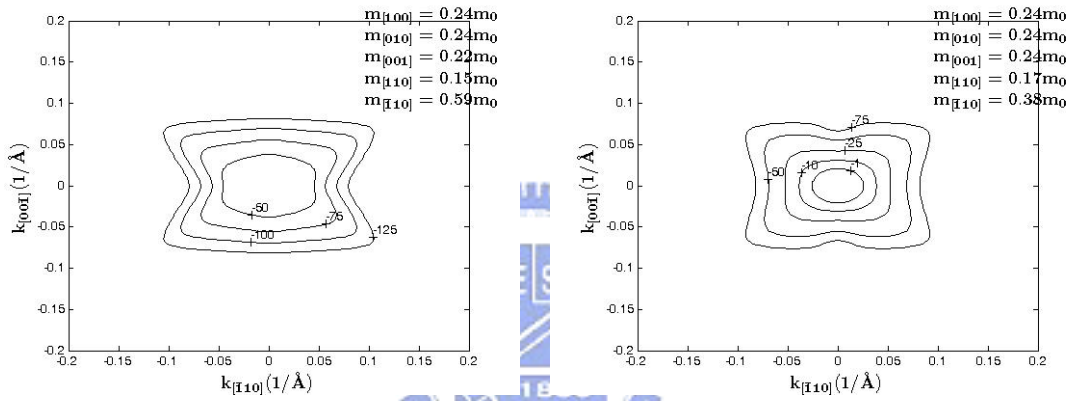
(b)

Fig. 2.26. Contour map in k_x, k_y plane ($k_z=0$) of silicon under 1GPa biaxial (a) compressive (b) tensile stress on (001) wafer for three lowest valence bands.

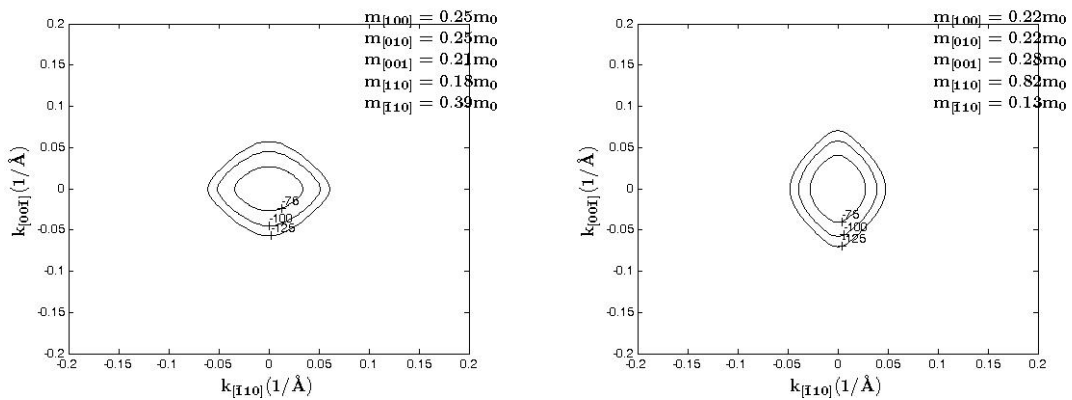
Top band



Second band



Third band

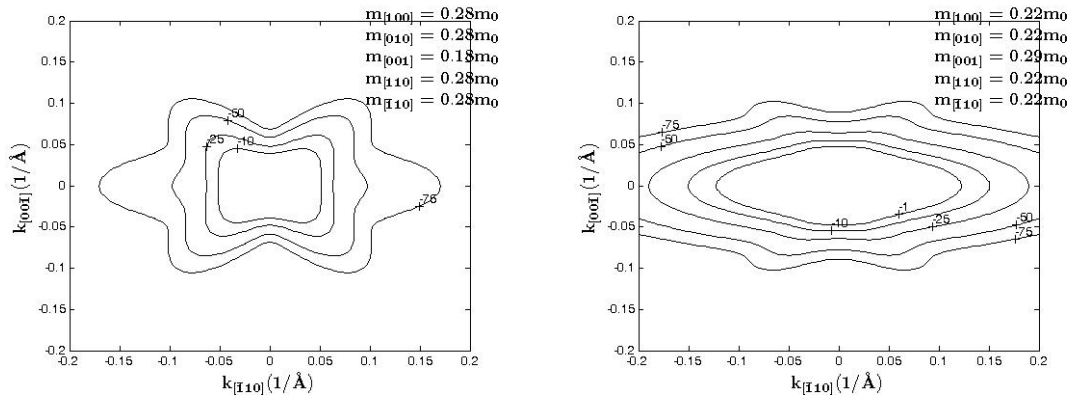


(a)

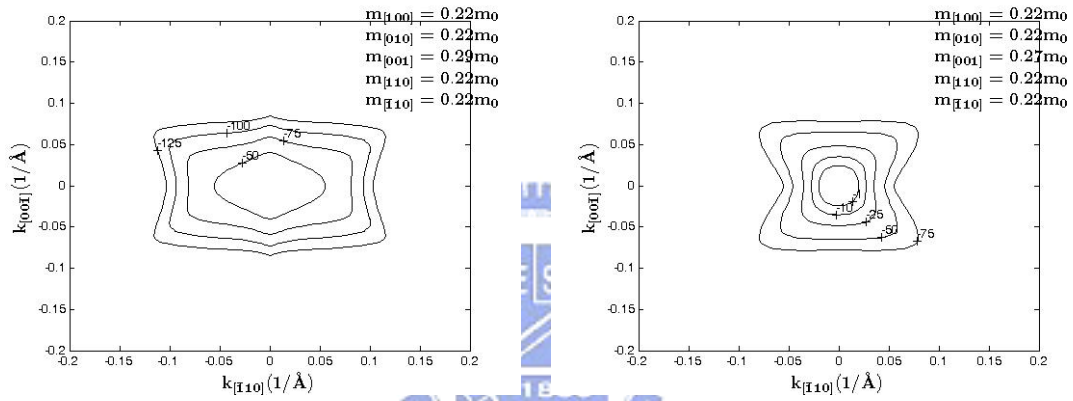
(b)

Fig. 2.27. Contour map in k_x , k_y plane ($k_z=0$) of silicon under 1GPa uniaxial longitudinal (a) compressive and (b) tensile stress on (110) wafer for three lowest valence bands.

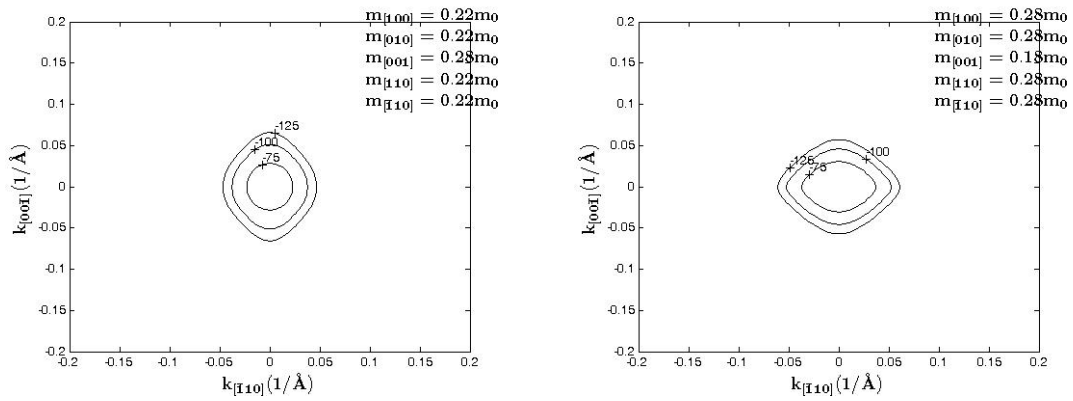
Top band



Second band



Third band

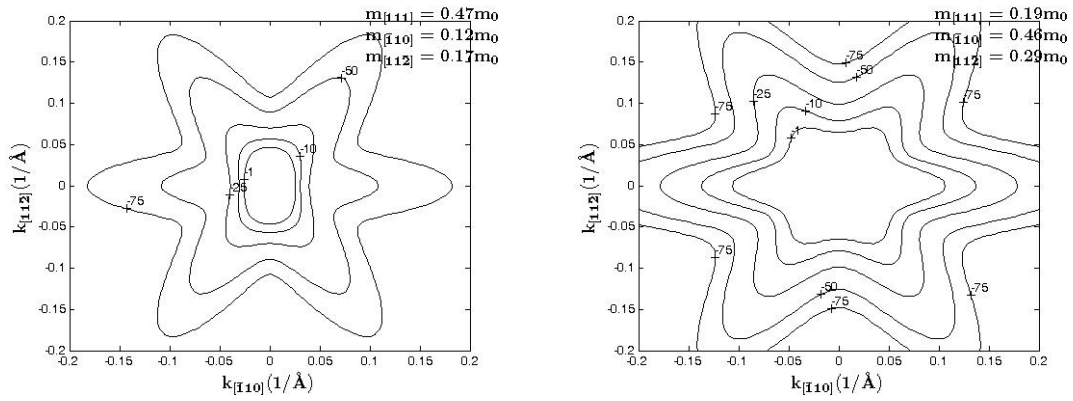


(a)

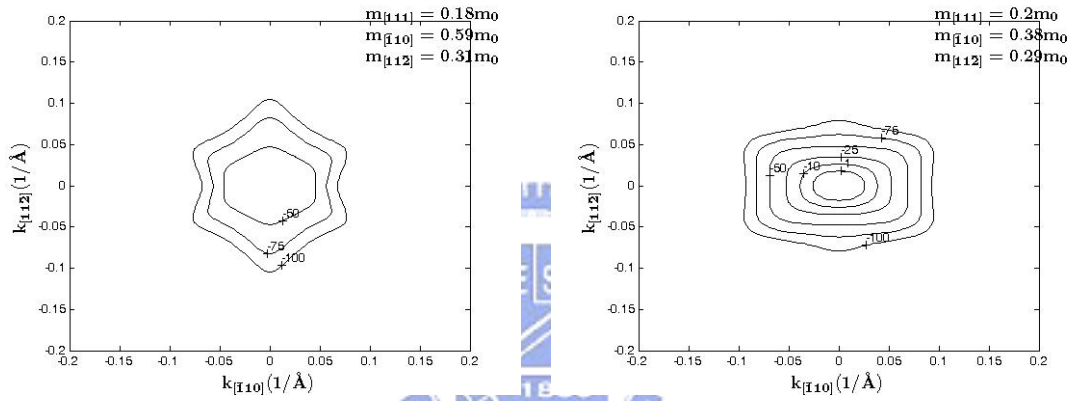
(b)

Fig. 2.28. Contour map in k_x , k_y plane ($k_z=0$) of silicon under 1GPa uniaxial transverse (a) compressive and (b) tensile stress on (110) wafer for three lowest valence bands.

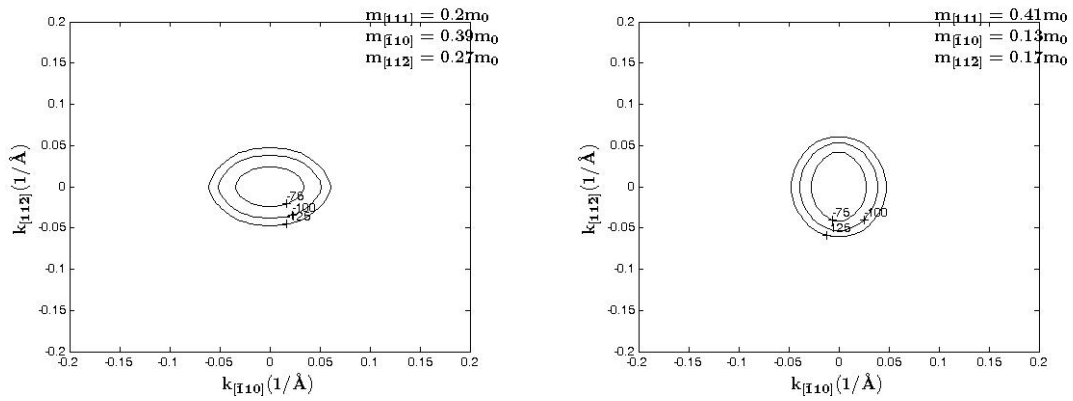
Top band



Second band



Third band

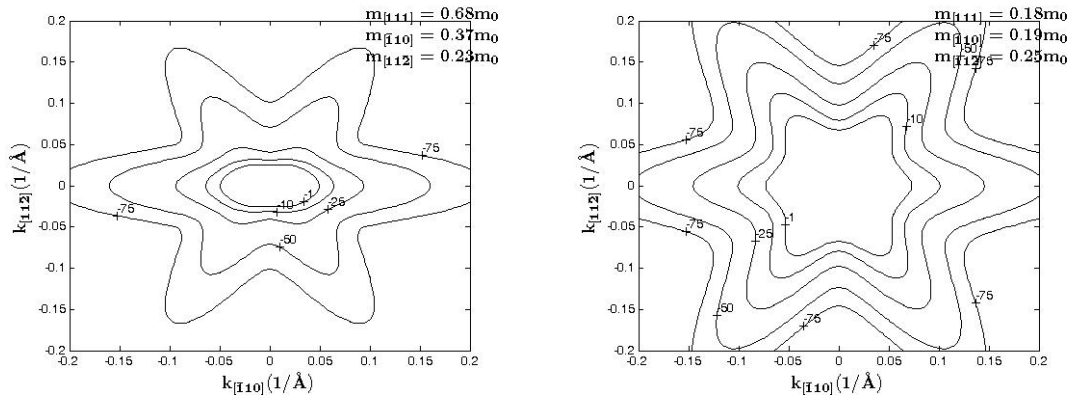


(a)

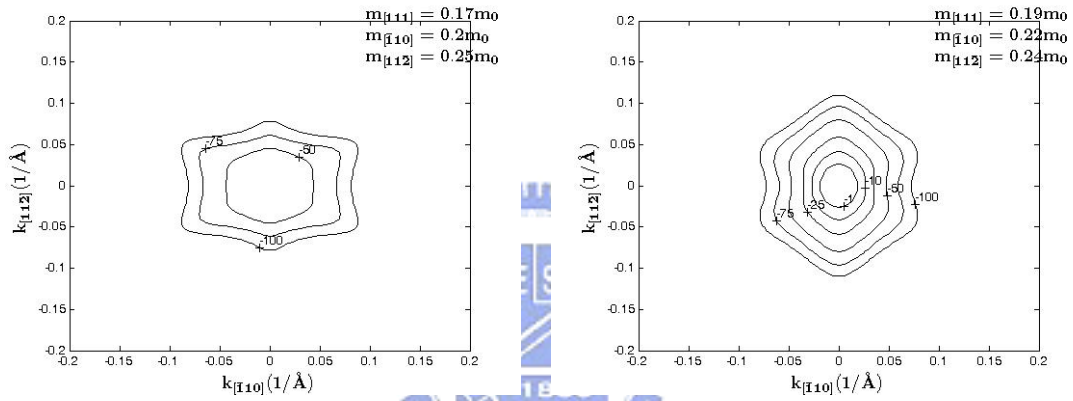
(b)

Fig. 2.29. Contour map in k_x , k_y plane ($k_z=0$) of silicon under 1GPa uniaxial longitudinal (a) compressive and (b) tensile stress on (111) wafer for three lowest valence bands.

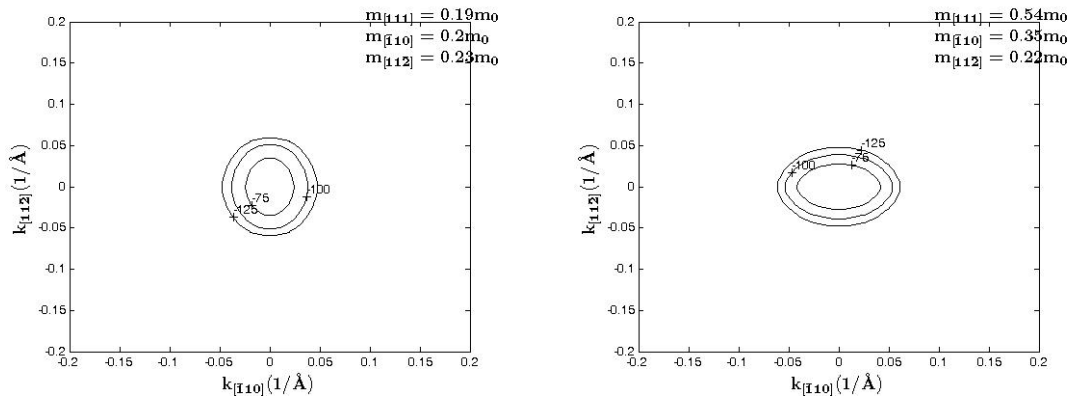
Top band



Second band



Third band

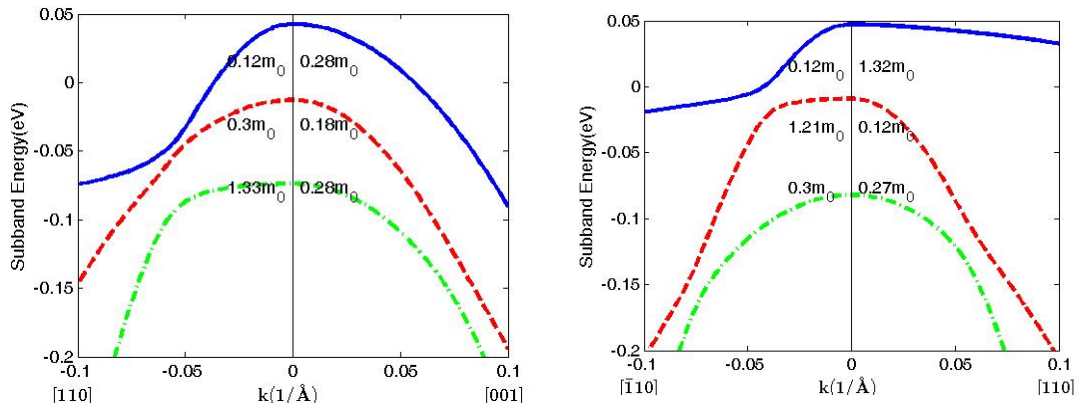


(a)

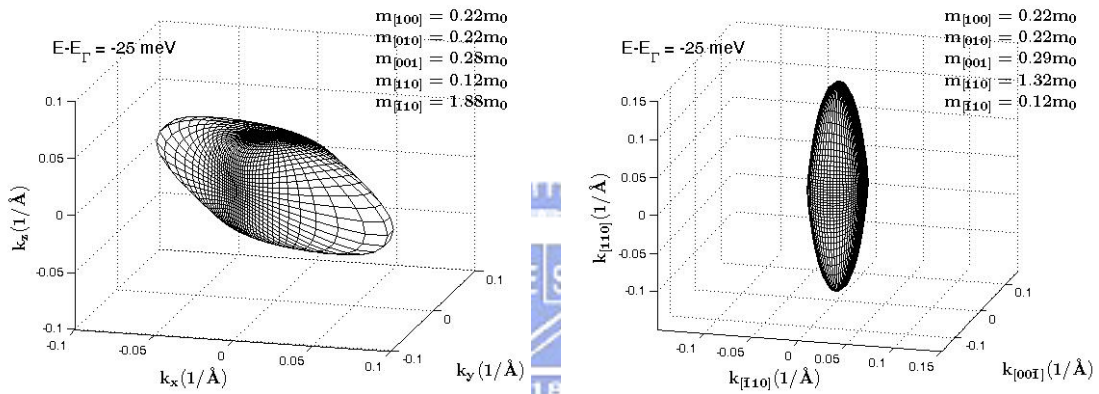
(b)

Fig. 2.30. Contour map in k_x, k_y plane ($k_z=0$) of silicon under 1GPa uniaxial transverse (a) compressive and (b) tensile stress on (111) wafer for three lowest valence bands.

Band structure



Constant energy surface



Energy contour in the surface

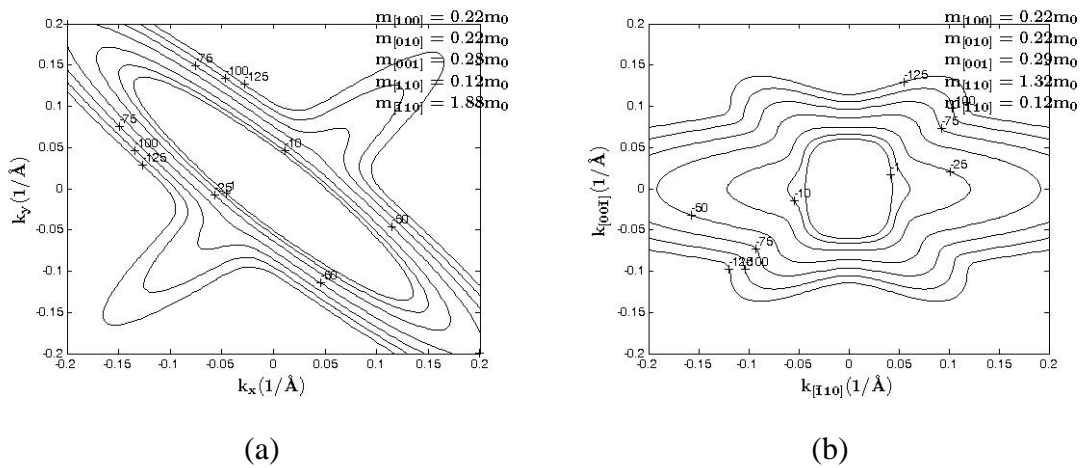


Fig. 2.31. Band structures, constant energy surface, and energy contour of bulk silicon under 1GPa longitudinal compressive stress with additional 1GPa transverse tensile stress on (a) (001) and (b) (110) wafer, respectively.

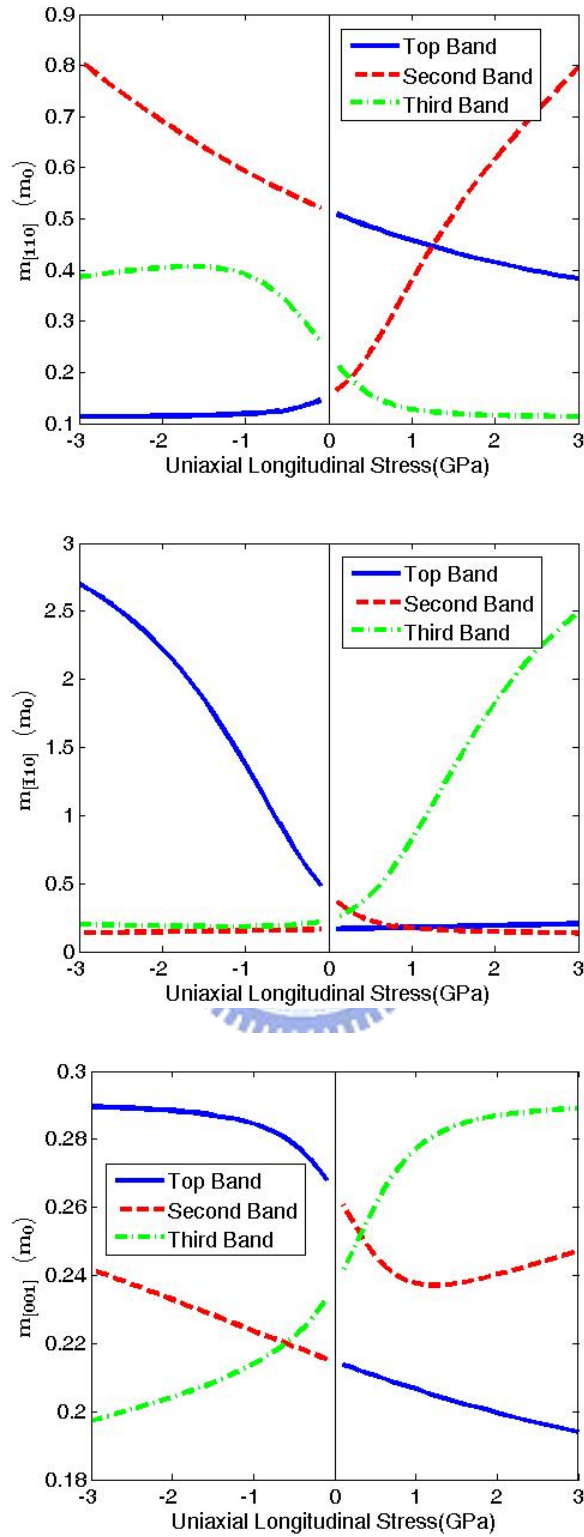


Fig. 3.1. Effective masses along the three axes of the ellipsoid, $m_{[110]}$, $m_{[\bar{1}10]}$, and $m_{[001]}$, versus uniaxial longitudinal stress for three lowest valence bands.

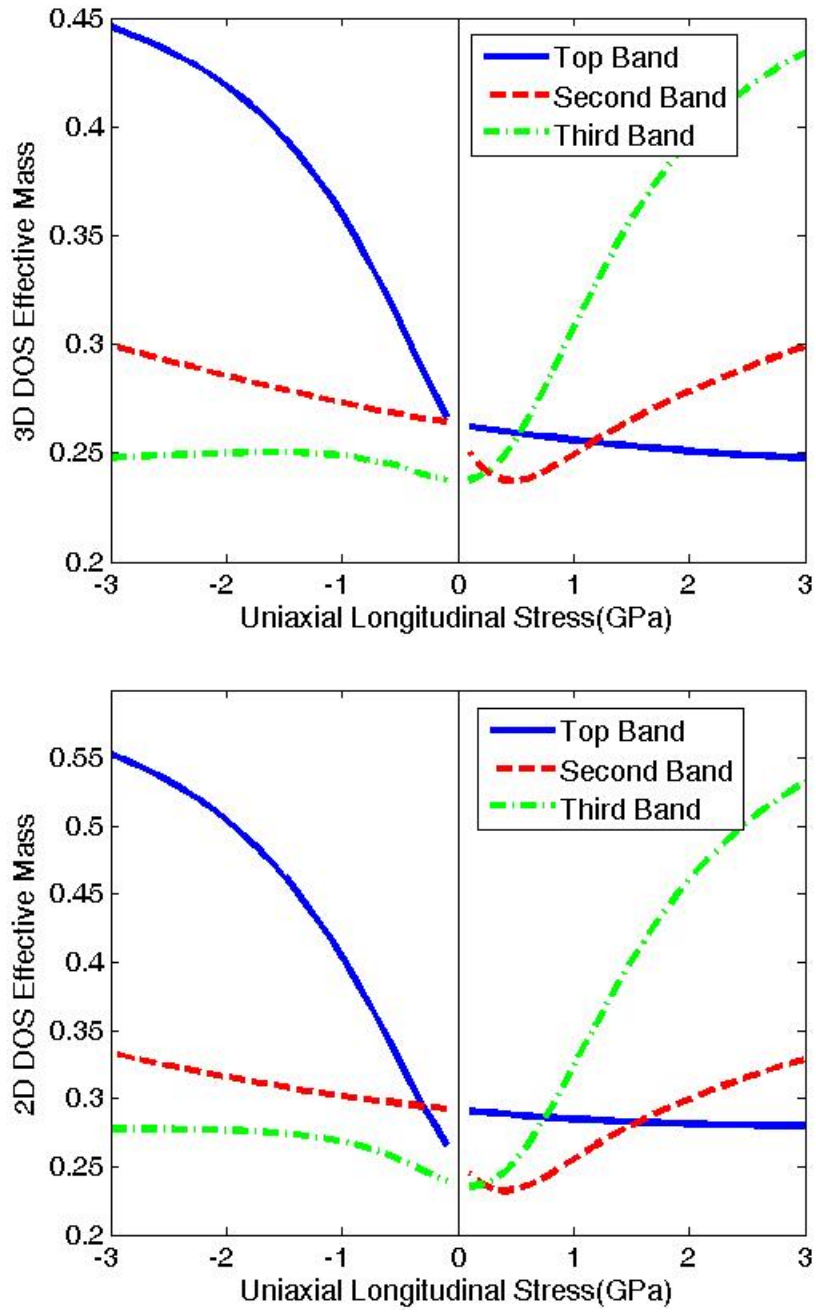


Fig. 3.2. 3D (bulk) and 2D DOS effective masses versus uniaxial longitudinal stress for three lowest valence bands.

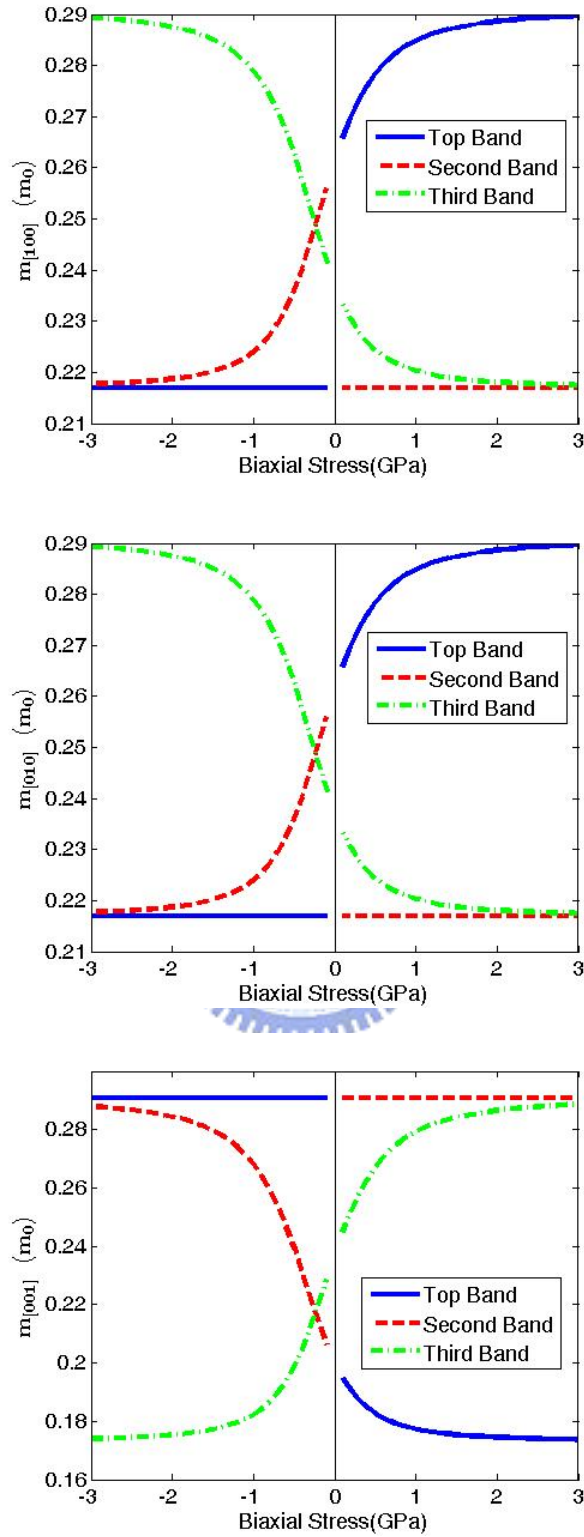


Fig. 3.3. Effective masses along the three axes of the ellipsoid, $m_{[100]}$, $m_{[010]}$, and

$m_{[001]}$, versus biaxial stress for three lowest valence bands.

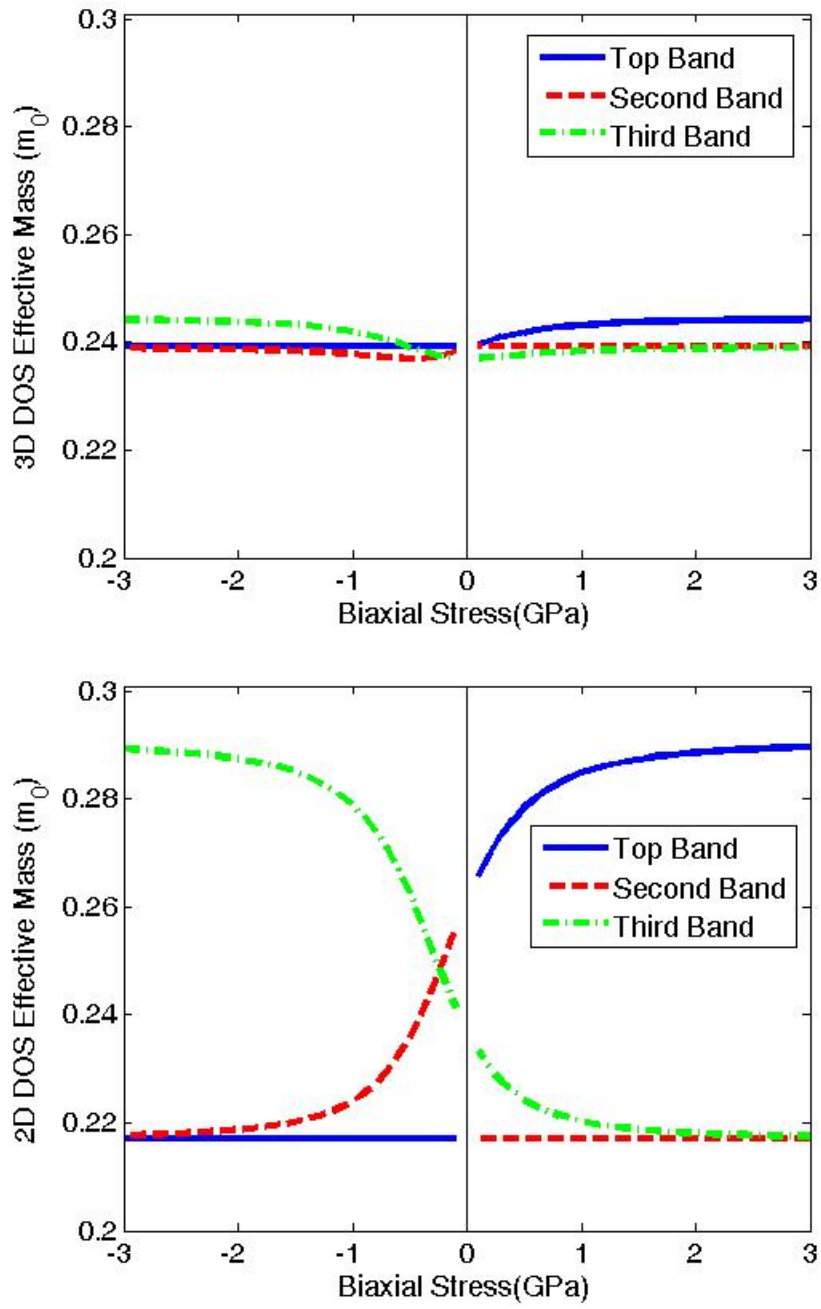


Fig. 3.4. 3D (bulk) and 2D DOS effective masses versus biaxial stress for three lowest valence bands.

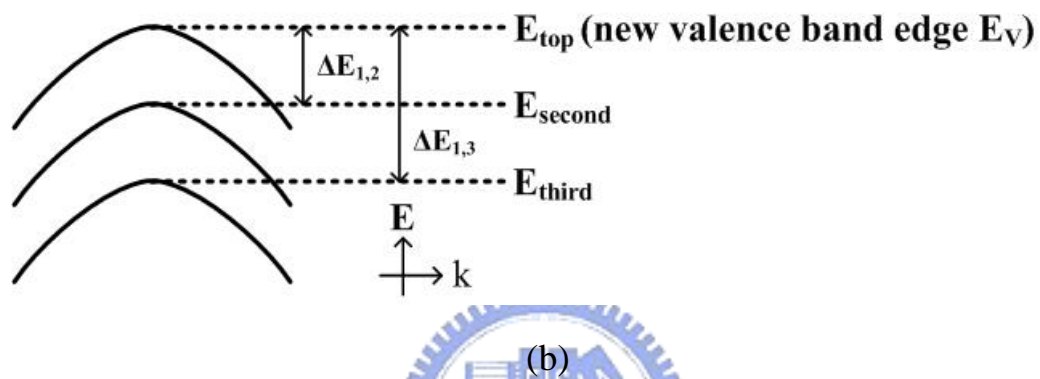
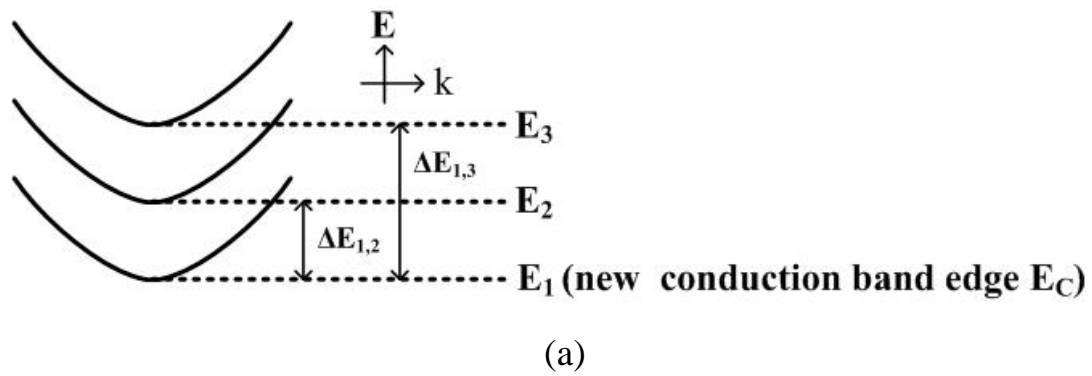


Fig. 3.5. Schematic of the strain-induced energy valleys splitting for (a) conduction band electrons and (b) valence band holes.

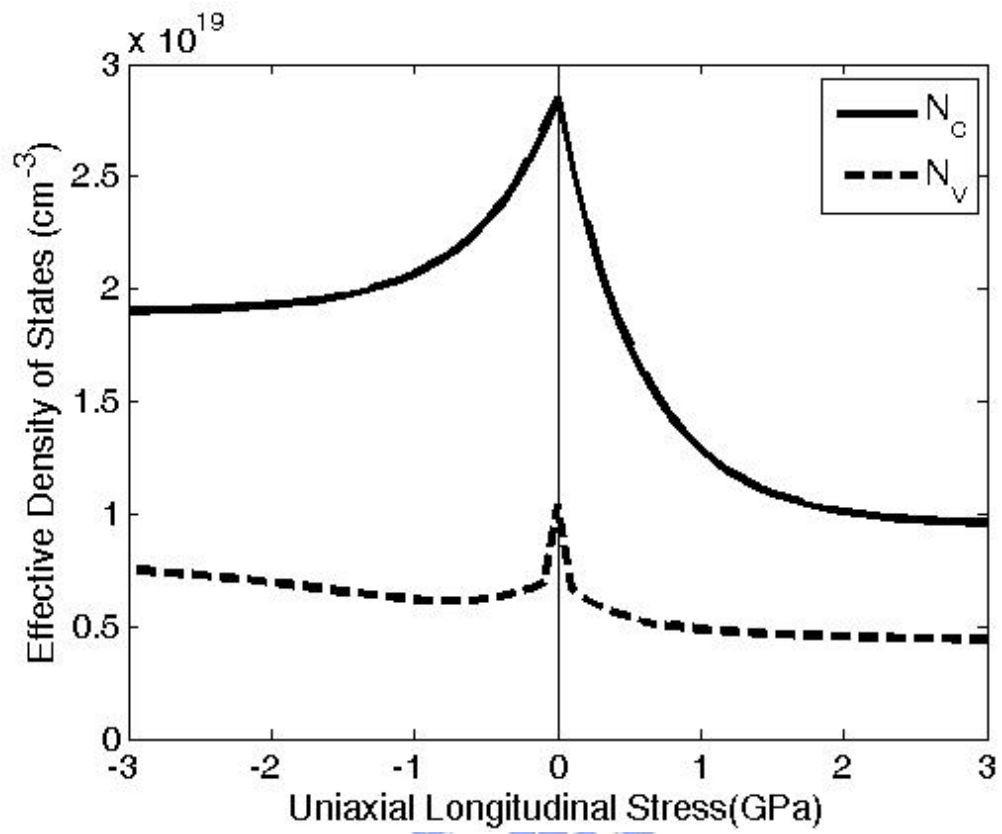


Fig. 3.6. Conduction and valence effective DOS, N_c and N_v , versus uniaxial stress.

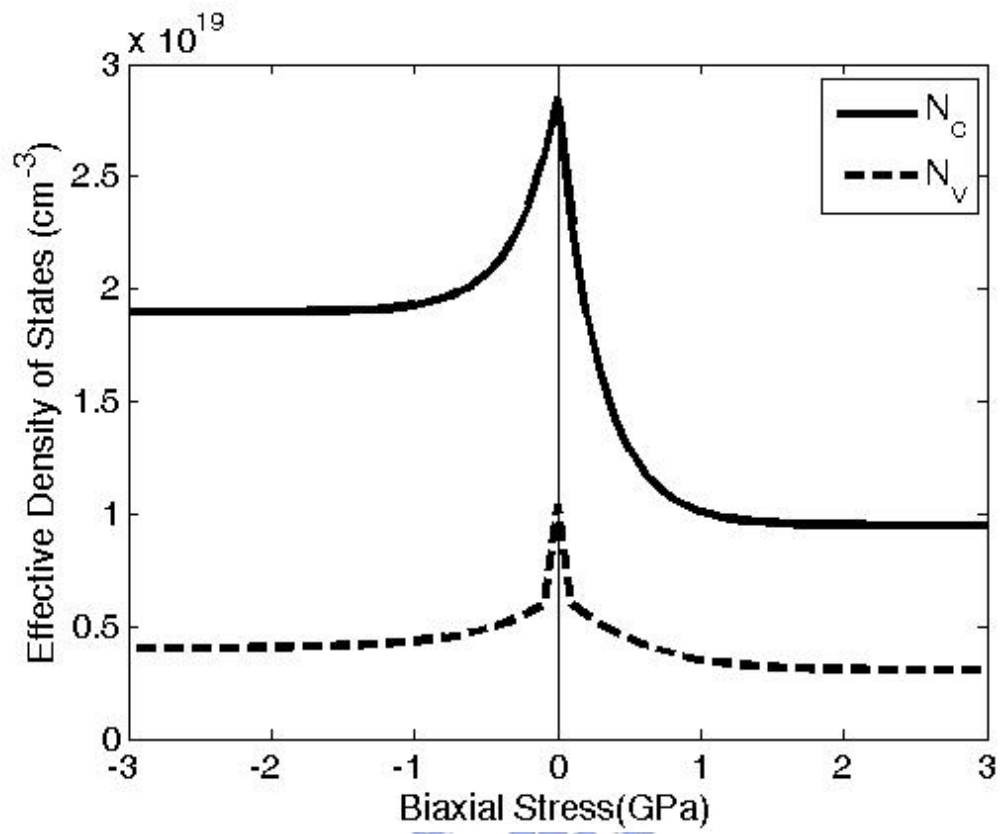


Fig. 3.7. Conduction and valence effective DOS, N_c and N_v , versus biaxial stress.



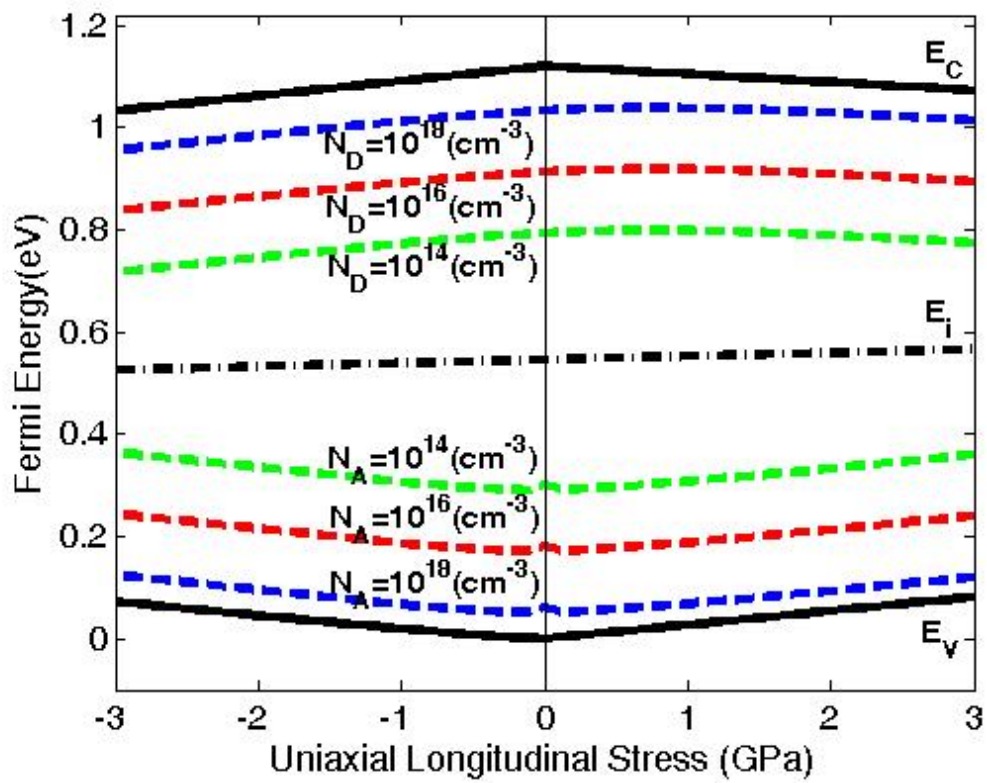


Fig. 3.8. Fermi energy of bulk silicon versus uniaxial stress for various doping concentrations. The figure also shows the intrinsic Fermi level, conduction band edge, and valence band edge versus stress.

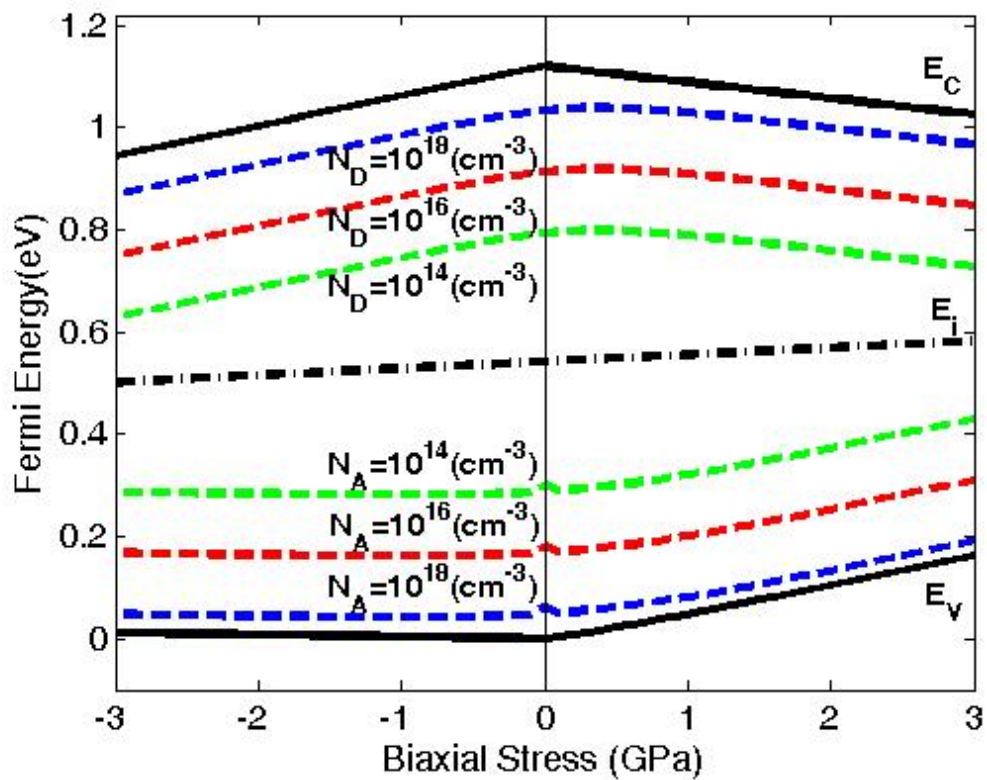


Fig. 3.9. Fermi energy of bulk silicon versus biaxial stress for various doping concentration. The figure also shows the intrinsic Fermi level, conduction band edge, and valence band edge versus stress.

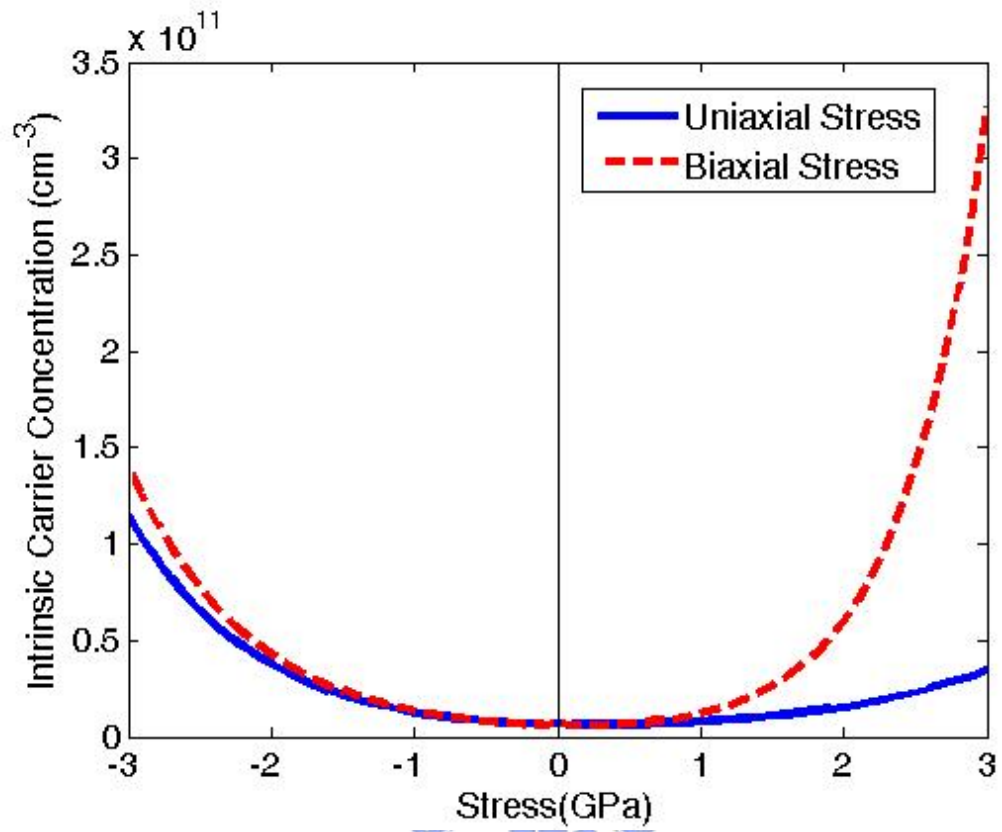


Fig. 3.10. Intrinsic carrier concentration versus uniaxial and biaxial stress.



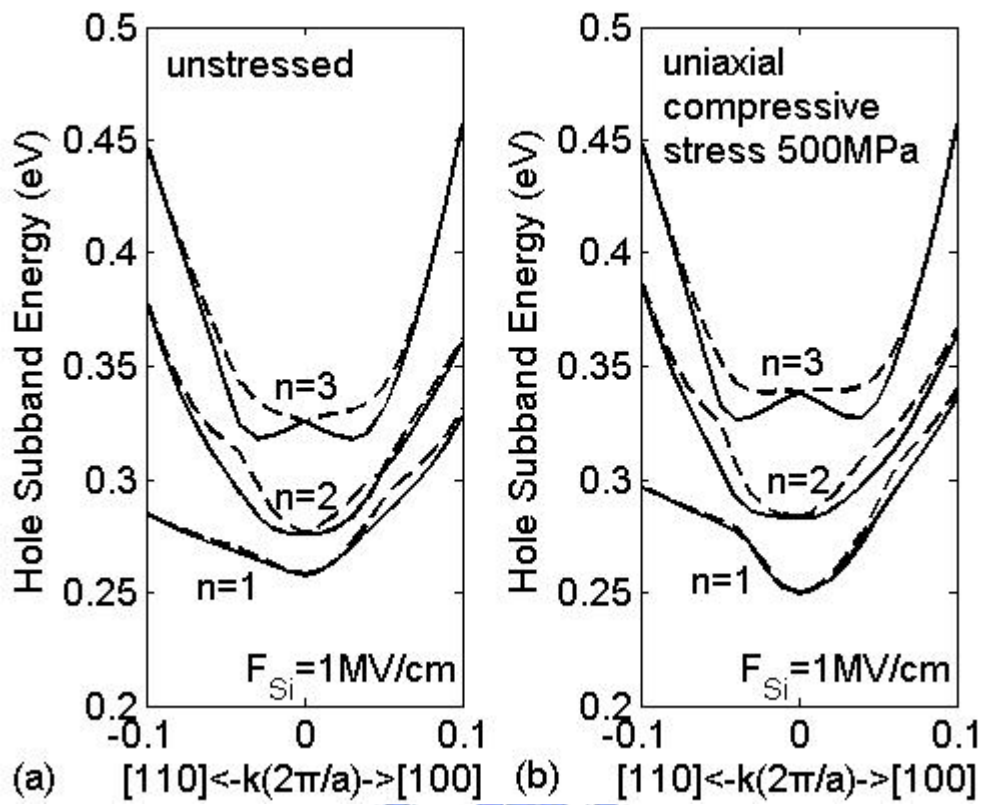


Fig. 4.1. Valence band hole dispersion relation along [100] and [110] direction for the three lowest bands calculated by six-band $k \cdot p$ method under channel inversion condition ($F_{Si}=1\text{MV/cm}$). The external stress is (a) unstressed and (b) 500MPa uniaxial compressive stress along [110] direction.

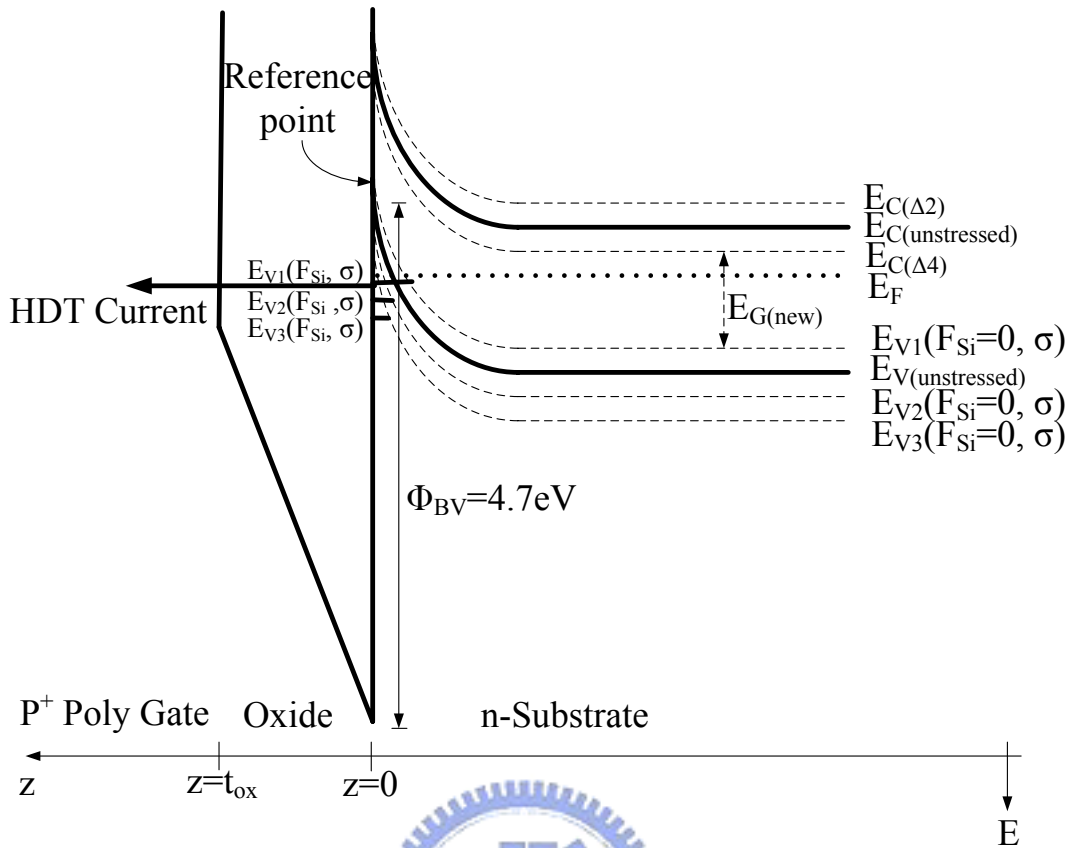


Fig. 4.2. Schematic of band diagram of a p^+ polysilicon/ SiO_2 / n -Si structure biased in channel inversion condition and stressed with uniaxial longitudinal compressive stress. The solid lines indicate the conduction and valence band edge without external stress. The dotted lines indicate the stress induced band edge shift of the conduction and valence band. The figure also shows the energy quantization effect in the channel inversion layer and hole direct tunneling current from the channel inversion layer to the polysilicon gate under stress.

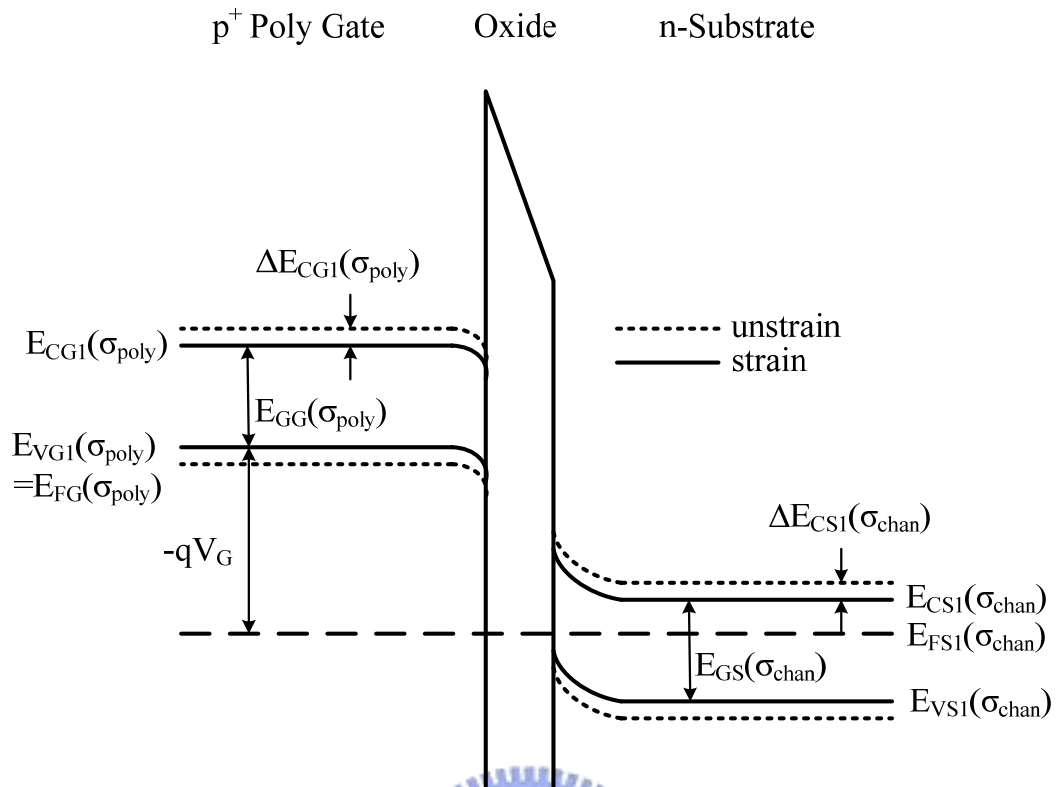


Fig. 4.3. Schematic of the band diagram of a p⁺ polysilicon/SiO₂/n-Si (pMOS) structure, which is biased a negative gate voltage. The poly gate and channel are under arbitrary strain. The expression of flat band voltage for pMOSFETs under arbitrary strain can be derived with the help of this diagram

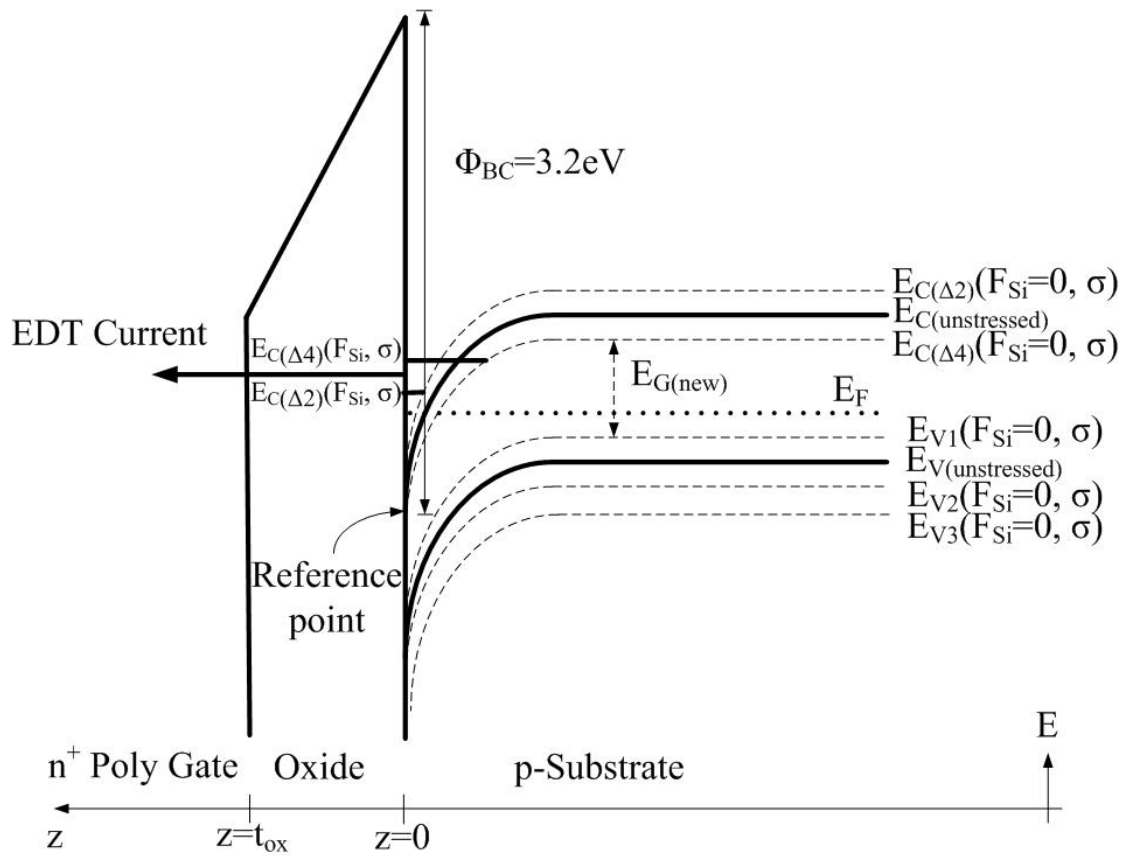


Fig. 4.4. Schematic of band diagram of an n^+ polysilicon/SiO₂/p-Si structure biased in channel inversion condition and stressed with uniaxial longitudinal compressive stress. The solid lines indicate the conduction and valence band edge without external stress. The dotted lines indicate the stress induced band edge shift of the conduction and valence band. The figure also shows the energy quantization effect in the channel inversion layer and electron direct tunneling current from the channel inversion layer to the polysilicon gate under stress.

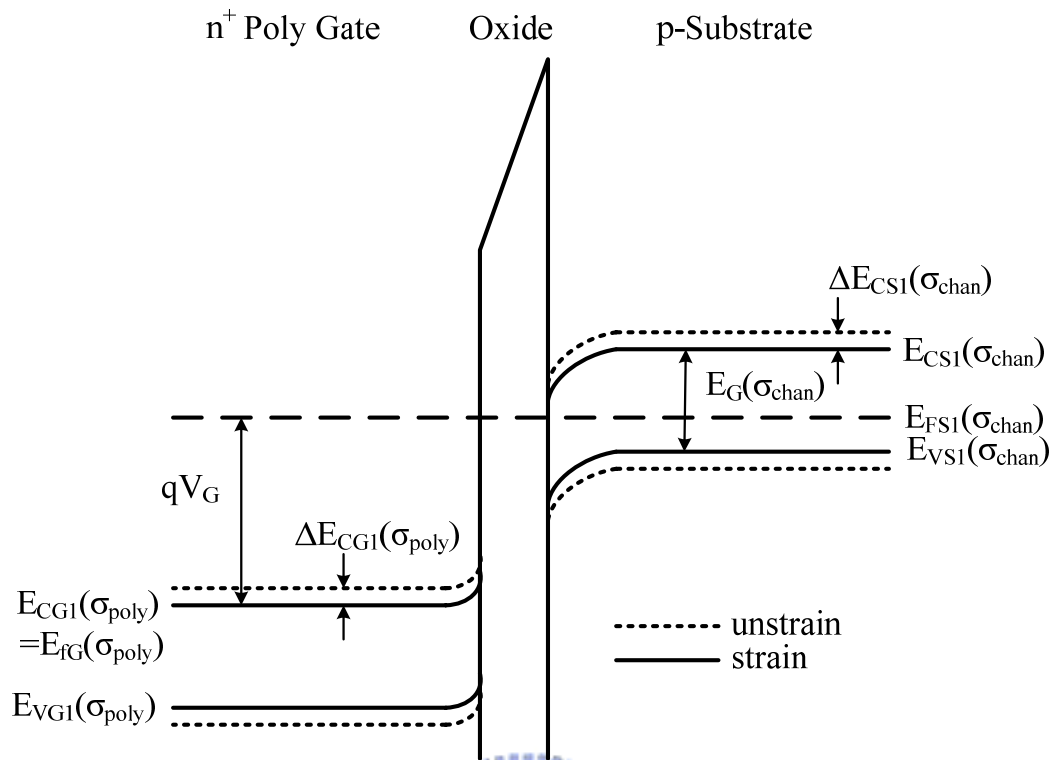


Fig. 4.5. Schematic of the band diagram of an n⁺ polysilicon/SiO₂/p-Si (nMOS) structure, which is biased a positive gate voltage. The poly gate and channel are under arbitrary strain. The expression of flat band voltage for nMOSFETs under arbitrary strain can be derived with the help of this diagram

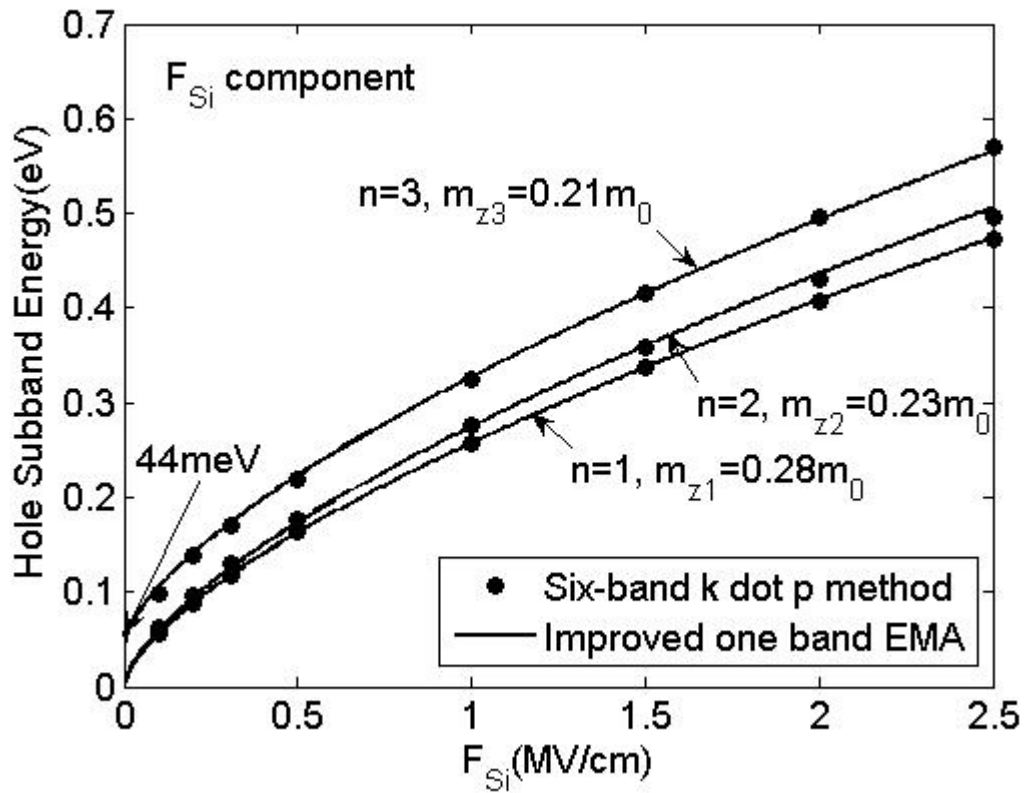


Fig. 4.6. Hole subband energy at gamma point versus F_{Si} without external stress. The circles are data calculated by the six-band $k \cdot p$ method with Schrödinger-Poisson equation. The solid lines are the fitting by the triangular potential approximation and the improved one band EMA. The figure also shows the quantization effective mass of the three lowest bands for best fitting.

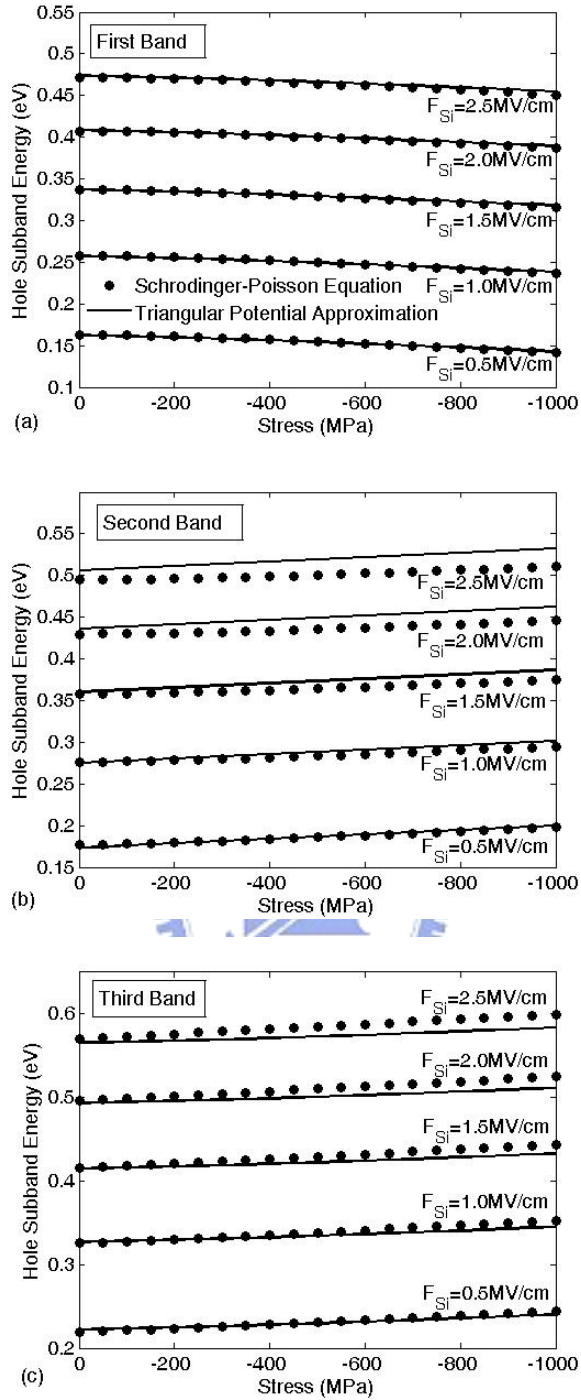


Fig. 4.7. Hole subband energy at gamma point versus stress with various F_{Si} . (a) First band, (b) second band, and (c) third band. The circles are data calculated by k dot p method with Schrödinger-Poisson equation. The solid lines are the data calculated by Equation (4.1) for the three lowest bands, respectively.

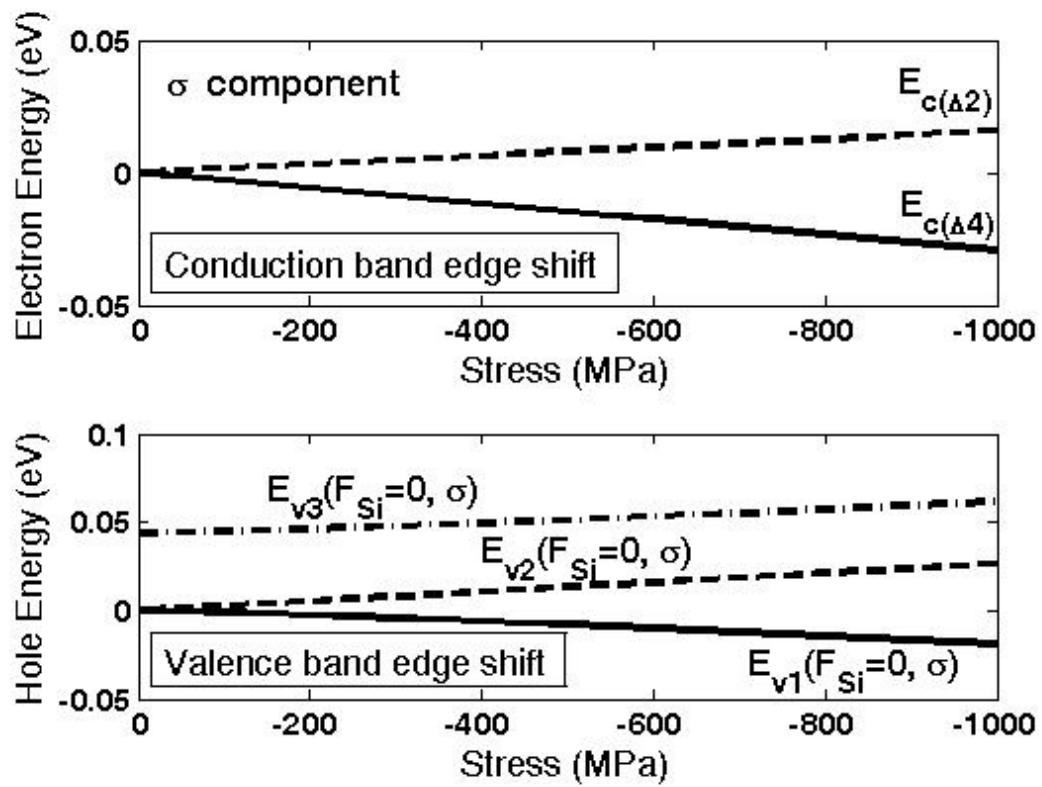


Fig. 4.8. The strain-induced band edge shift versus stress for bulk silicon (a) conduction and (b) valence band.

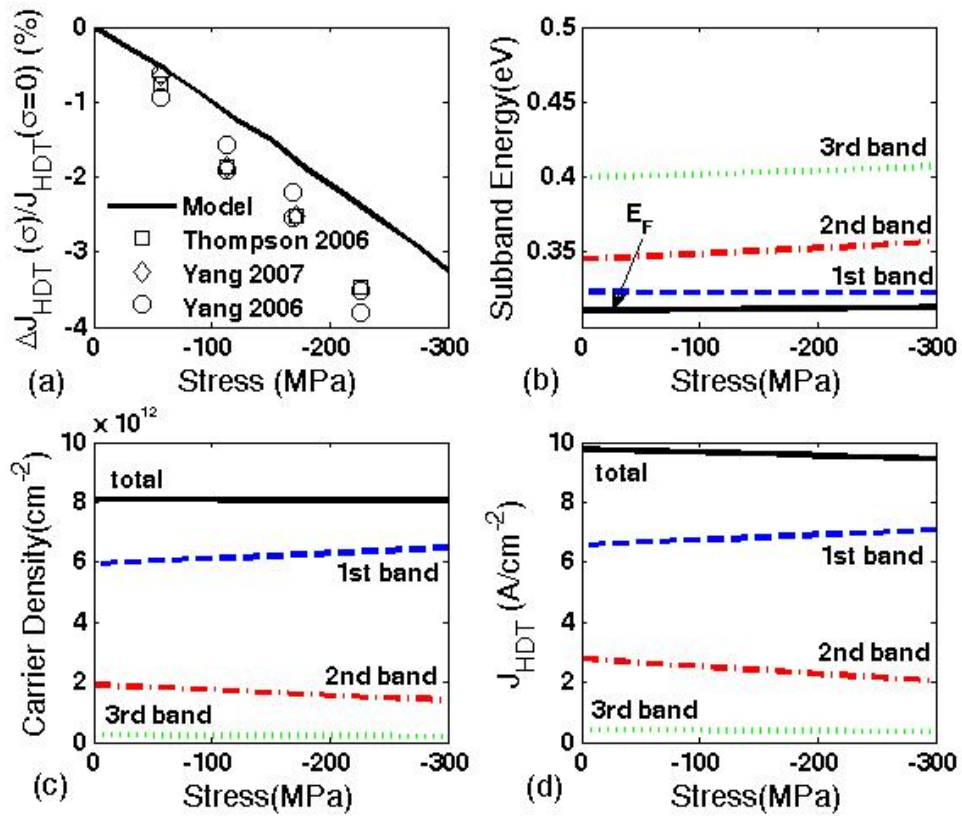


Fig. 4.9. (a) $\Delta J_{HDT}/J_{HDT}$ versus Stress. The squares, diamonds, and circles are data published by former works. The solid lines are the simulation result by our model. (b) Hole subband energy versus stress. (c) Carriers density versus stress. (d) Hole direct tunneling current density versus stress.

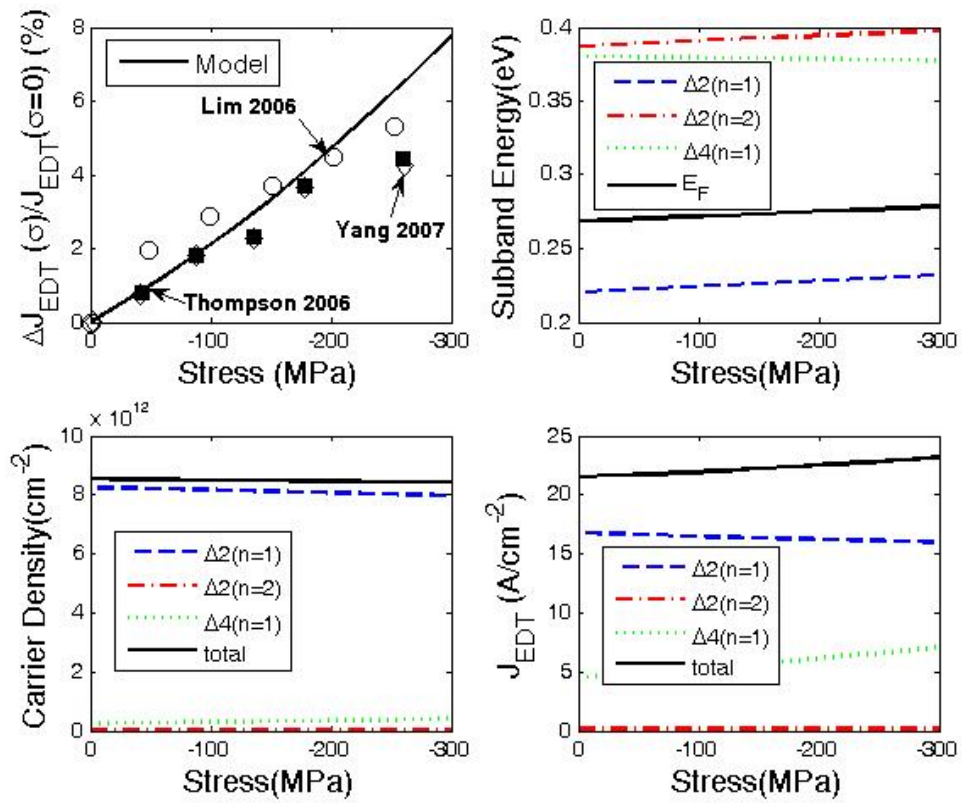


Fig. 4.10. (a) $\Delta J_{EDT}/J_{EDT}$ versus Stress. The squares, diamonds, and circles are data published by former works. The solid lines are the simulation result by our model. (b) Electron subband energy versus stress. (c) Carriers density versus stress. (d) Electron direct tunneling current density versus stress.

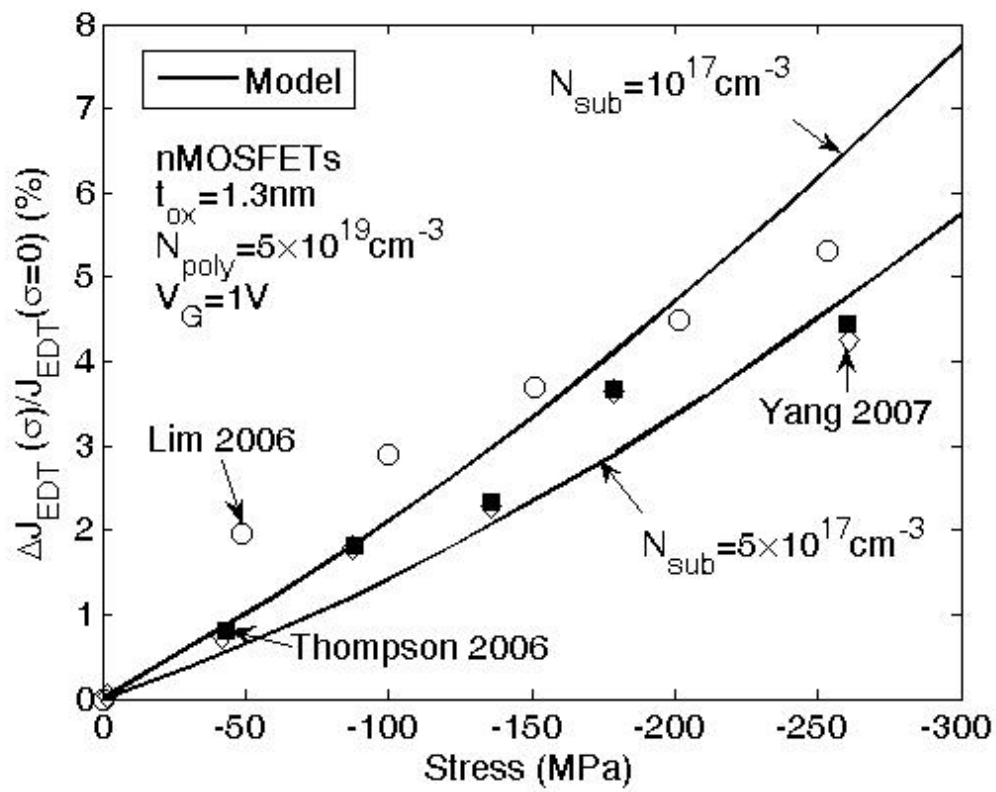


Fig. 4.11. Compare the influences of electron direct tunneling current between the two different doping concentrations of substrate.

Vita

姓 名：林以唐 Yi-Tang, Lin

性 別：男

出生日期：中華民國 七十三年 三月 九日

出 生 地：台北市

住 址：台北縣永和市得和路 361 號 4 樓

學 歷： 國立交通大學 電子工程學系

(西元 2002 年 9 月~2006 年 6 月)

國立交通大學 電子所固態組 碩士班

(西元 2002 年 9 月~2008 年 8 月)

經 歷：大學部半導體元件物理助教

論文題目：奈米級金氧半場效電晶體應變矽物理之研究
Strained Silicon Physics in Nanoscale MOSFETs